STUDY OF SUPERCONDUCTING NANOSTRUCTURE TOWARDS ITS APPLICATION AS SINGLE PHOTON DETECTOR

Thesis submitted in partial fulfillment of the requirements for the degree of

DOCTOR OF PHILOSOPHY
IN
DEPARTMENT OF APPLIED PHYSICS

by

MANJU SINGH
2K11/PHDAP/10

Under the supervision of

Dr. RISHU CHAUJAR
Assistant Professor
Department of Applied Physics
Delhi Technological University
Delhi 110042

Dr. R. K. RAKSHIT
Scientist
Time and Frequency and Electrical and Electronics Metrology Division
CSIR-National Physical Laboratory
Delhi 110012

DELHI TECHNOLOGICAL UNIVERSITY,
SHAHBAD DAULATPUR,
MAIN BAWANA ROAD
DELHI-110042

AUGUST 2018

CERTIFICATE

This is to certify that the PhD thesis entitled **"STUDY OF SUPERCONDUCTING NANOSTRUCTURE TOWARDS ITS APPLICATION AS SINGLE PHOTON DETECTOR"** submitted to Delhi Technological University India, for the award of degree of Doctor of Philosophy is based on the original research work carried out by me under the supervision of Dr. Rishu Chaujar, Department of Applied Physics, Delhi Technological University India and Dr. Rajib K. Rakshit, Time & Frequency and Electrical & Electronics Metrology division, CSIR-National Physical Laboratory India. It is further certified that the work embodied in this thesis have not submitted in part or full to any other University or institution for the award of any degree or diploma.

Manju Singh
(Enrolment No.: 2K11/PhDAP/10)

This is certified that the above statement made by the candidate is correct to the best of our knowledge.

Dr. Rishu Chaujar
(Supervisor)
Assistant Professor
Department of Applied Physics
Delhi Technological University
Delhi

Dr. Rajib K. Rakshit
(Co-Supervisor)
Scientist
Time & frequency and Electrical
& Electronics Metrology Division
CSIR-NPL, New Delhi

Prof. Suresh C. Sharma
Head of Department
Department of Applied Physics
Delhi Technological University
Delhi, India

DECLARATION

This is to certify that thesis entitled **"STUDY OF SUPERCONDUCTING NANOSTRUCTURE TOWARDS ITS APPLICATION AS SINGLE PHOTON DETECTOR"** being submitted for the award of degree of Doctor of Philosophy to Delhi Technological University India, embodies the original research work carried out by me under the supervision of Dr. Rishu Chaujar, Department of Applied Physics, Delhi Technological University and Dr. Rajib K. Rakshit, Time & Frequency and Electrical & Electronics Metrology division, CSIR-National Physical Laboratory India. The results obtained in this thesis have not been submitted in part or full to any other University or institution for the award of any degree or diploma.

Manju Singh
Research scholar
Enrolment No.: 2K11/PhDAP/10

Date: …….
Place: Delhi

ACKNOWLEDGEMENTS

I would like to thank everyone who inspired and supported me to carry out this work and contributed to take this work at a point where this could be realized in a thesis form.

My sincere thank to my supervisor, Dr. Rishu Chaujar for offering me the opportunity to perform the research under her guidance and assistance. I would like to thank her for managing her time to review this report.

I am also thankful to the chairman and members of Departmental Review Committee, DTU for their constructive criticism and excellent advice which have been beneficial for my thesis in some form or the other.

I would like to thank Dr. S. C. Sharma, Head, Department of Applied Physics for his timely help and support. My sincere thanks are due to Dr. Rinku Sharma, PhD coordinator, DTU, for her support and guidance.

I would like to express my sincere appreciation to my co-supervisor Dr. Rajib K Rakshit for guiding me and supporting me in carrying forward the work.

I would like to show my gratitude to Dr. V. N. Ojha, Head of the Department, Time & Frequency and Electrical & Electronics Metrology Division, CSIR-NPL for permitting me to attend meetings/ discussion in DTU as and when required and also for his support in carrying out this activity.

I am grateful to Dr. D. K. Aswal, Director, CSIR-NPL for his immense support.

I would like to acknowledge CSIR-NPL and DTU where I got infrastructure and opportunity to carry out this research and enhance my knowledge.

I would like to thank CSIR for funding network project, Advanced Quantum Research and Innovation in Ultra Small Systems (AQuaRIUS), to our group Quantum Phenomena and Applications (QPA).

My sincere thanks to Dr. Ranjana Mehrotra, my then HOD, QPA Division for her support in providing financial support through AQuaRIUS project and her guidance.

I would like to acknowledge the contribution of Dr. Sudhir C. Husale in nanofabrication using FIB, Dr. Anurag Gupta in magnetic measurement, Dr. Vidyanand Singh in scanning electron microscopy imaging.

I would like to thank Dr. Mandar Deshmukh, TIFR, Mumbai and his team for their time and help in nanostructure fabrication. It was the effort of his team in his guidance which helped me in optimization of reciepe using EBL and RIE respectively.

My sincere thanks to Indian nanoelectronics users program (INUP) and the team of IITB associated with this program for their help towards optimization of nanostructure fabrication and contact pads using EBL and photolithography respectively.

I would like to thank Dr. Alexander Korneev, Moscow Institute of Physics and Technology (MIPT), Russia for his time to time support and guidance in the fabrication and measurement related work.

Dr. A. H. Majedi, University of Waterloo deserves a special mention for his inputs in designing of low temperature measurement setup.

I also take this opportunity to acknowledge Cryo Industries of America Inc. for discussion in designing and manufacturing the low temperature measurement setup.

I am also thankful to the staff of liquid nitrogen and helium plants for providing cryogenics indispensable for my research work. I convey my special thanks to workshop staff at CSIR-NPL for their time to time technical support in my research work.

Manju Singh
(Enrolment No.: 2K11/PhDAP/10)

ABSTRACT

This study is about fabrication and characterization of nanostructures towards its application as single photon detector. Since this type of nanostructure can detect infrared radiation up to 2000nm, special care needs to be taken for selection of its dimensions as well as substrate and superconducting material for the growth of thin film.

Quantum optical technologies have many applications in the area of quantum teleportation, quantum computation (QC), quantum key distribution (QKD). These applications rely significantly on the performance of a single photon detector. Photo multiplier tube (PMT) is one of the initially invented photon detectors. Si based avalanche photodiode (APD) has better performance metrices in comparison to PMT. However, both these technologies have limitation at telecom wavelengths. Although InGaAs based photodetector shows better detection efficiency at infrared, it has its own shortcomings due to high dark count rate, relatively large time jitter, low count rate and after-pulsing effect. Superconducting nanowire based detectors have shown a lot of potential in recent years as single photon detector at the wavelength of interest for its application in the area of quantum optical technologies due to its better performance metrices.

The thesis starts with the study of superconducting properties of materials in case of two dimensional structures as well as one dimensional structure. The superconducting nanowire single photon detector (SNSPD) device fabrication incorporates five main steps, i.e.

(1) Device operation principle and modeling.

(2) Customized low temperature experimental setup for transport property measurement as well as optical characterization of the sample.

(3) Thin film fabrication and optimization using suitable superconducting material and its transport property measurement.

(4) Nanostructure fabrication and optimization of its process parameters and its transport property.

(5) Optical characterization of the nanowires in meander shape using readout electronics in microwave frequency range.

This thesis mainly focuses on first, second, third and fourth points as given above. Discussion on the device operation, modeling involves fundamental physics which help understanding the behavior of the device. The modeling of the device along with other components of the readout electronics has helped simulating the output response of the optical setup which can be verified experimentally in future. The overall fabrication steps of nanowires in meander shape have also been discussed along with design of contact pads in coplanar waveguide shape. The optical mask design for its use in fabrication of contact pads to save machine time of EBL is also discussed.

It is obvious that detection and measurement of low level light signal is very difficult. When it comes to detecting single photon and that too in the infrared range, the difficulty level enhances due to lower photon energy. Detecting such weak signal with high detection efficiency requires low operating temperature in the range of mK to few Kelvin depending on the material used for the fabrication of detector. It is found that the detection efficiency of SNSPDs increases and the dark count diminishes significantly with decrease in operating temperature.

An experimental setup down to 1.8K is designed using liquid helium flow cryostat along with probes for electrical as well as optical characterizations. Economical consumption of liquid helium, sound temperature stability, and efficient optical coupling, easy and user friendly samples changing option without breaking the vacuum, or warming up the cryostat were some of the important requirements taken into considerations while designing the cryostat. Sample holder with necessary arrangements for precise alignment of laser light with the active area of device to enhance optical coupling efficiency is designed for the optical probe. The INVAR alloy is used for sample holder to ensure that the alignment is not disturbed at low temperature. Single mode fibres due to its high transmission rate, minimum attenuation and least distortion have been used to shine light on the samples. Sample holder with 20-pin LCC socket and matching chip carrier provides convenient and fast sample mounting in electrical insert. Mu-metal is employed to cover the sample

space in both the inserts to attenuate any electromagnetic interference. Further, temperature stability with the passage of time is also monitored. It is found that variation in temperature is less than 10mK at lowest operating temperature. Apart from the above, another important advantage of the system is its very low liquid helium loss rate (~100ml/hr) with all inserts which allows uninterrupted measurements for several days without refilling of liquid helium.

Further, the thesis includes fabrication of thin films, patterning of nanowire structure and transport studies both on thin films and nanostructures. The niobium nitride (NbN) films were deposited using reactive magnetron sputtering. Argon to nitrogen ratio played a crucial role in the synthesis of high quality superconducting NbN. Critical temperatures (Tc) of about 15.5K have been measured for films with a thickness of about 10nm. Zero-Field-Cooled (ZFC) magnetization measurements were carried out to optimize the superconducting properties in ultra thin NbN films. The transport behavior down to 2K was studied using conventional resistance vs. temperature and current-voltage characteristics.

Fabrication of NbN superconducting nanowires based on focused ion beam milling (FIB) and electron beam lithography (EBL) is presented. The detailed study of fabrication of nanowires with optimized process parameters using EBL is presented.

Effect of gallium contamination on superconducting properties is discussed. Superconducting transition temperature as well as the transition width of nanowires do not show any significant impact of processing steps of standard EBL route, there is a significant degradation of superconducting properties for nanowires prepared using FIB. Gallium ion implantation across the superconducting channel may be considered as the root cause for this. The effect of gallium implantation may be the reason of technological limitations in designing fascinating single photon detector architectures, nevertheless provides some interesting manifestation of intrinsic low dimensional superconducting properties.

LIST OF PUBLICATIONS

Publications Relevant to this thesis

1 Manju Singh, Rishu Chaujar, S. Husale, S. Grover, Amit P. Shah, Mandar M. Deshmukh, Anurag Gupta, V. N. Singh, V. N. Ojha, D. K. Aswal, and R. K. Rakshit, "Influence of Fabrication Processes on Transport Properties of Superconducting Niobium Nitride Nanowires," Current Science **114,** 1443 (2018).

2 M. Singh, R. Chaujar, and R. K. Rakshit, "Cryogenic measurement setup for characterization of superconducting nano structures for single photon detection applications." (Accepted for publication in Current Science).

Other publications

1. Dinesh K. Misra, Rajib K. Rakshit, **Manju Singh**, P.K. Shukla, K.M. Chaturvedi, B. Sivaiah, B. Gahtori, Ajay Dhar, S.W. Sohn, W.T. Kim, D.H. Kim, *Materials and Design* **58,** 551 (2014). *High yield strength bulk Ti based bimodal ultrafine eutectic composites with enhanced plasticity.*

2. Anurag G. Reddy, Neha Aggarwal, Shibin Krishna T. C., **Manju Singh**, Rajib Rakshit, and Govind Gupta, *Appl. Phys. Lett*. **106**, 233501 (2015). *Correlation of current–voltage–temperature analysis with deep level defects in epitaxial GaN films*

3. Pooja Singh, P. K. Rout, **Manju Singh**, R. K. Rakshit, and Anjana Dogra, *J. Appl. Phys*. **118**, 114103 (2015). *Thickness dependent charge transport in ferroelectric $BaTiO_3$ heterojunctions*

4. G Venkat Swamy, P. K. Rout, **Manju Singh**, and R. K. Rakshit, *J. Phys D: Appl Phys.* **48**, 47502 (2015). *Resistance minimum and electrical conduction mechanism in polycrystalline CoFeB thin films*

5. Pooja Singh, Prasanna Rout, Sudhir Husale, Anurag Gupta, **M Singh**, R Rakshit, and Anjana Dogra. *J. Magn. Magn. Mat.* **419**, 566 (2016) *Non-linear polaronic conduction in magnetite nanowires*

6. G. Venkat Swamy, Dinesh Kumar, R. K. Rakshit, G. A. Basheed, K. K. Maurya, **Manju Singh**, and Anurag Gupta, *AIP Conf. Proc*. **1731**, 110048 (2016).*Structural and electrical transport studies on CrN(001) thin films*

7. Monu Mishra, Abhiram Gundimed, Shibin Krishna, Neha Aggarwal, Bhasker Gahtori, Nita Dilawar, Ved Varun Aggarwal, **Manju Singh**, Rajib Rakshit, and Govind Gupta, *Phys. Chem. Chem. Phys.* **19**, 8787 (2017) *Wet chemical etching induced stress relaxed nanostructures on polar & non-polar epitaxial GaN films*

8. Shibin Krishna, Anurag G.Reddy, Neha Aggarwal, Mandeep Kaur, Sudhir Husale, Dinesh Singh, **Manju Singh**, Rajib Rakshit, K. K.Maurya, and Govind Gupta, *Sol. Energy Mater Sol. Cells*. **170**, 160 (2017) *Enhanced current transport in GaN/AlN based single and double barrier heterostructures*

9. Pooja Singh, P. K. Rout, **Manju Singh**, R. K. Rakshit, and Anjana Dogra, *Thin solid films* **643**, 60 (2017) *Ferroelectric memory resistive behavior in BaTiO3/Nb doped SrTiO3 heterojunctions*

CONTENTS

LIST OF TABLES

LIST OF FIGURES

CHAPTER 1

INTRODUCTION

1.1 Introduction

The research that is being put forward, in recent times, to explore newer single photon detection systems has triggered huge interest in the areas of photonics, quantum optics and nanostructured optics. Photon counting technology has already revolutionized the areas of electronics, biotechnology, medical physics, space and military applications, meteorology and metrology. In addition, technological advancements require standardization of quantum optical systems, such as, photon sources, modulators and detectors.

In this chapter, all types of single photon detectors are briefly reviewed. It explains the performance of detectors based on values of the parameters required for its evaluation. Various photon detection technologies are described along with their limitations and reason for the final selection of SNSPD as topic of the thesis. The evolution of SNSPD since beginning and the progress in fabrication technology for its improvement with time is explained. At last, its various applications are described. The chapter concludes with a statement of the motivation for undertaking the present work and an outline of the remaining chapters of this thesis.

1.2 Single Photon Detectors (SPD)

Single-photon detector is one of the essential components for quantum optical information processing technology. More specifically, modern optical applications like photon correlation spectroscopy and quantum cryptography require fast single photon detectors with ultimate quantum efficiency and spectral resolution in the optical and infrared spectral range [1].

1.3 Performance matrices of single photon detector

Performance of SPD can be accessed on the basis of figure of merit as explained in the following sections.

1.3.1 Detection efficiency

Detection efficiency is the ratio of the number of detected photons to the total number of photons incident on a device. The system detection efficiency (η_{SDE}) of any detector is the product of three parameters namely coupling efficiency ($\eta_{coupling}$), absorption efficiency ($\eta_{absorption}$) and intrinsic detection efficiency ($\eta_{intrinsic}$).

$$\eta_{SDE} = \eta_{coupling} \times \eta_{absorption} \times \eta_{intrinsic.} \quad (1.1)$$

$$\eta_{DDE} = \eta_{absorption} \times \eta_{intrinsic.} \quad (1.2)$$

The coupling efficiency ($\eta_{coupling}$) is the ratio of the number of photons incident on the device to the total photons emitted by a source. All the photons emitted from the source do not necessarily reach the device due to loss, absorption, scattering etc. in the environment. The photons that fall on the device out of total emitted photons do not get absorbed by the detector and few of them get reflected / transmitted / scattered by the device. The ratio of photons that get absorbed by the device to the total photons incident on the device is called absorption efficiency ($\eta_{absorption}$). Absorption efficiency ($\eta_{absorption}$) is dependent on structural design of the detector and can be enhanced by incorporating anti reflection coating, optical cavity, waveguide structure and antenna etc [2]. Intrinsic detection efficiency is the property of the material. All the photons do not get registered by the device even after falling and getting absorbed by it. The ratio of registered photons by the device out of total absorbed photons is called its intrinsic detection efficiency ($\eta_{intrinsic}$).

1.3.1.1 Geometry

The geometry of the superconducting structures is characterized by ξ_{GL}, $d << w << \Lambda$ ($= 2\lambda^2/d$) and their length $L >> w$, where ξ_{GL} is the superconducting Ginzburg–Landau (GL) coherence length, Λ the Pearl length or effective magnetic penetration depth in films with $d << \lambda_L$ and λ_L the London penetration depth. Typically, in NbN based photon detectors w is of the order of 100 nm or more and $d \approx 4$ - 6nm, while the zero-temperature coherence length $\xi_{GL}(0) \approx 4$ nm. The low-temperature London penetration depth $\lambda_L \approx 350$nm so that the Pearl length $\Lambda \approx 40\mu m >> w$. Further, it was observed that the coupling efficiency is proportional to the value of both the coupling factor (K_P) and the fill factor of the device. The K_P of incident light is proportional to the active area of detector. Experimentally, it was found that the diameter of hotspot generated on a 3.5nm

thick film by a photon of 1550nm is about 40nm which then expands with passage of time. The detailed studies on evolution of hotspot area and its repercussion on quantum efficiency were studied by Korennev et al. [3] and Verevkin et al [4]. Shown in Fig.1.1 are some important results of their studies.

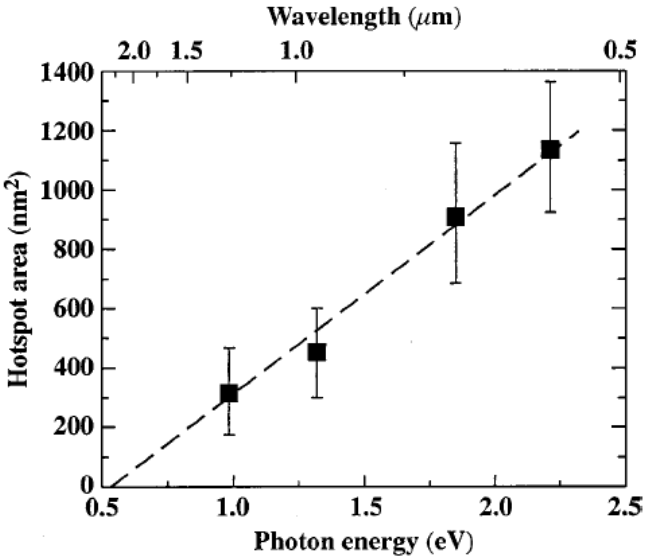

Fig.1.1 (a): Hotspot area for meander structure in an area of 10μm x 10μm with nanowires of 10nm thickness, 200nm width and 400nm pitch as a function of photon energy with top axis showing corresponding photon wavelength [4].

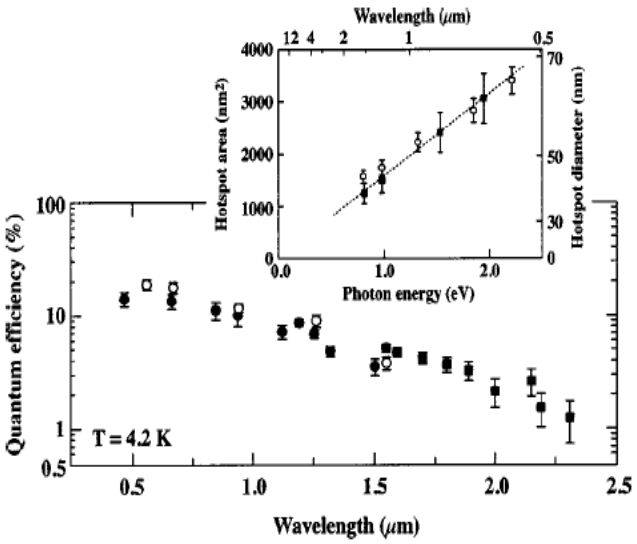

Fig.1.1 (b): Wavelength dependence of quantum efficiency for 3.5-nm-thick NbN SSPDs (2 numbers), with laser diodes (circles) and a blackbody radiation (squares) as photon sources. The hotspot area and diameter dependence on the incident photon energy (wavelength) can be seen in inset. The open and closed symbols correspond to the two devices [3].

1.3.1.2 Bias current

The device is usually biased with biasing current (I_B) ranging from 0.85Ic to 0.95Ic for better performance where Ic is the critical current at particular operating temperature. It was found that within this range detection efficiency increases with increasing bias current. The dependence of performance matrices of SNSPD on I_B were studied earlier [3, 4] and are summarized in Fig.1.2.

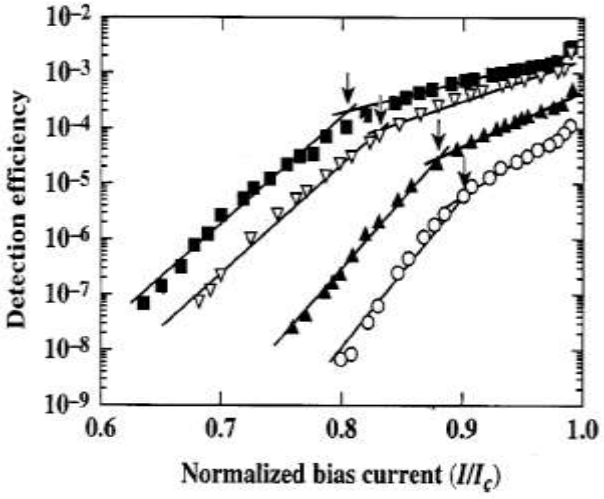

Fig.1.2 (a): Detection efficiency as a function of normalized bias current of the detector at 560 (closed squares), 670 (open triangles), 940 (closed triangles), and 1260nm (open circles) at 4.2K [4].

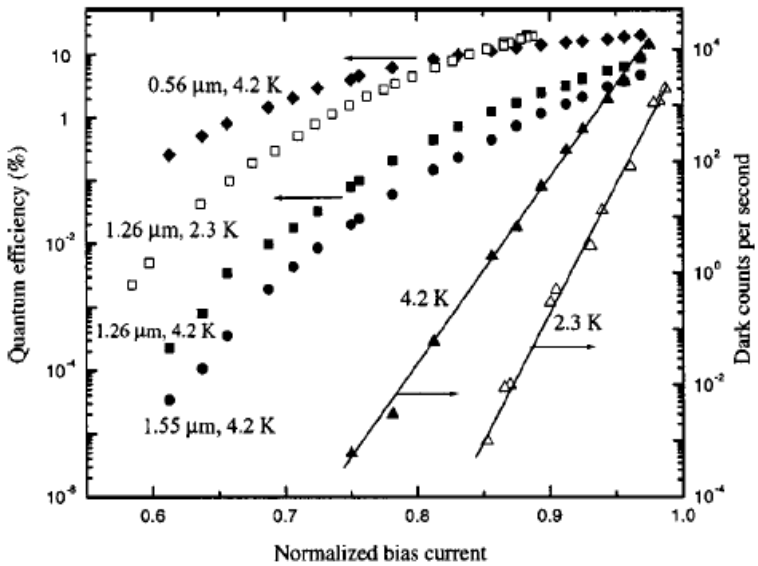

Fig.1.2 (b): QE and dark counts as a function of normalized current bias performed on 10x10 mm^2 area, 3.5nm thick NbN detector for several radiation wavelengths at 4.2K (closed symbols) and 2.3K (open symbols) [3].

The increase in QE with bias current is exponential initially but as the bias current reaches towards the critical current, the QE lowers significantly in a 3.5nm thick sample in comparison to 10nm thick sample (Fig.1.2 (a)). Further, Fig.1.2 (b) shows quantum efficiency (QE) and dark count rate (DCR) with respect to normalized bias current. Both QE and DCR increase with bias current whereas the QE increases and DCR decreases as the operating temperature go down. It can also be seen that the QE decreases with increasing wavelength.

1.3.1.3 Operating temperature

Size of a hotspot while decreases, its relaxation time increases with decreasing operating temperature. The reduction in hotspot area with decreasing temperature saturates below ≈ 0.5Tc. Since the diffusion of quasi-particles does not change much below 0.5Tc, the operating temperature range is kept below this value. The largest improvement in quantum efficiency (QE) was noticed at lower (2K) operating temperature which reaches a plateau below 2K. The dependence of QE on operating temperature that influences the critical current density was studied in details by Il'in et al. [5]. Some of their important results are shown in Fig.1.3.

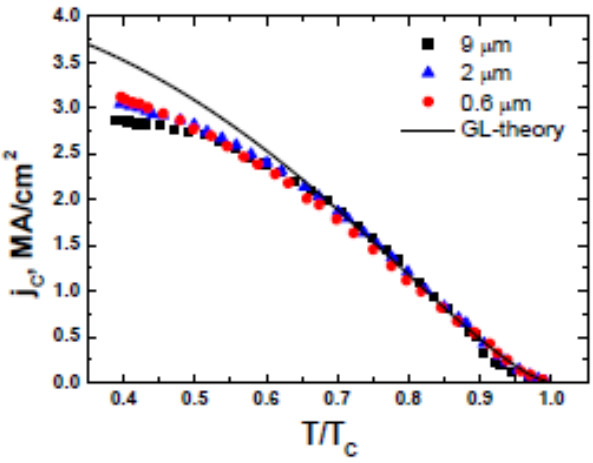

Fig.1.3 (a): Temperature dependencies of the critical current density in NbN bridges on Si [5].

1.3.1.4 Photon energy

The size of hotspot scales up with photon energy. It is shown that the QE increases with photon energy and saturates beyond particular photon energy as the hotspot area covers the entire width of the nanowires at this wavelength [6].

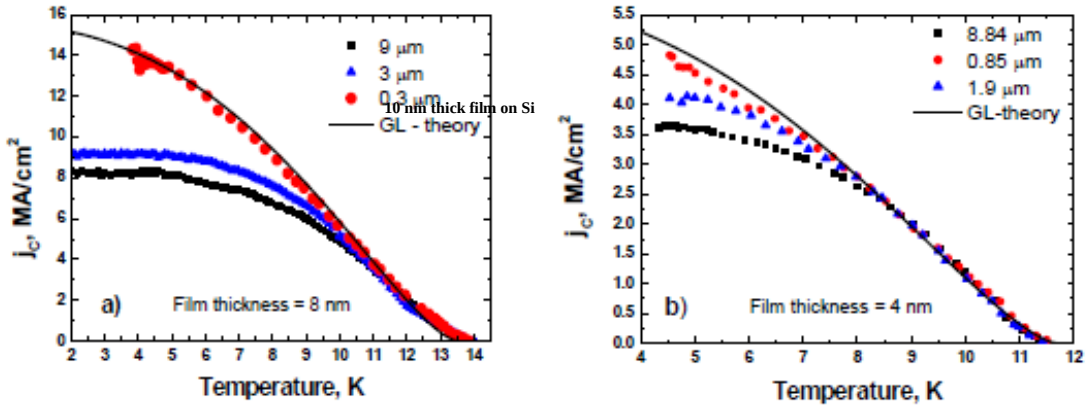

Fig.1.3 (b&c): Temperature dependencies of the critical current density in NbN bridges on sapphire [5].

1.3.2 Spectral sensitivity

SNSPD devices have wide spectral sensitivity which depends on energy band gap of the superconducting material. According to the hotspot model (described in chapter 2), the minimum energy, i.e. maximum wavelength required for appearance of the resistive nucleus depends on the equilibrium concentration of Cooper pairs around photon absorption site. Resistive nucleus formation is also dependent on the cross section of the nanowire. However, the appearance of resistive nucleus beyond the cut off wavelength due to hotspot mechanism indicates that there is some other mechanism responsible for appearance of resistance. When the photon energy is not sufficient to take the absorption site to normal state, fluctuation assisted photon detection takes place [7]. In this case the fraction of the line around the photon absorption site remains superconducting however, normal fluctuation may still occur. The NbN devices become effectively non sensitive above 2.5μm wavelength [4].

1.3.3 Dark count rate

Low dark count rate has always been a challenge for the use of any single photon detector in advanced applications. Sometimes the device mimics the detection of photon even in its absence due to stray light and electrical noise. The source for generation of dark counts can either be internal or external. Internal dark counts can be thermally generated (thermal excitation of magnetic vortices) or due to fluctuation in the density of the superconducting condensate or due to phase slips [8] in case of

SNSPD. Thermally generated dark counts can be reduced by lowering the temperature. Externally generated dark counts are due to presence of stray light or noise in electrical setup. The operating parameters of detector for better performance can be optimized on the basis of understanding of the underlying processes taking place in the detector.

1.3.4 Timing resolution

The inherent fluctuation in a time gap (τ) between arrival of the photon at detector and its detection is known as time jitter and corresponds to the time resolution of the response time. The variation of time due to formation of resistive area in the device can be attributed to intrinsic jitter. Jitter due to laser source and electronics used in the measurement setup comes under extrinsic jitter category. Thus [9],

$$\Delta\tau sys^2 = \Delta\tau laser^2 + \Delta\tau electronics^2 + \Delta\tau SNSPD^2. \quad (1.3)$$

The jitter due to laser source can be minimized by using the laser source with less pulse width. The noise in the leading edge of the voltage pulse can be reduced by using appropriate filter before the amplifier. Chromatic dispersion inside optical fibre also plays an important role in the case of long distance transmission.

The jitter associated with SNSPD is mainly dependent on the value of bias current and constriction in the device. It can be reduced by increasing the bias current below critical current and also by reducing the constrictions in the device. Fig.1.4 while shows the time correlated single photon counting (TCSPC) setup, Fig.1.5 describes differential cryogenic HEMT readout circuit for time jitter measurement.

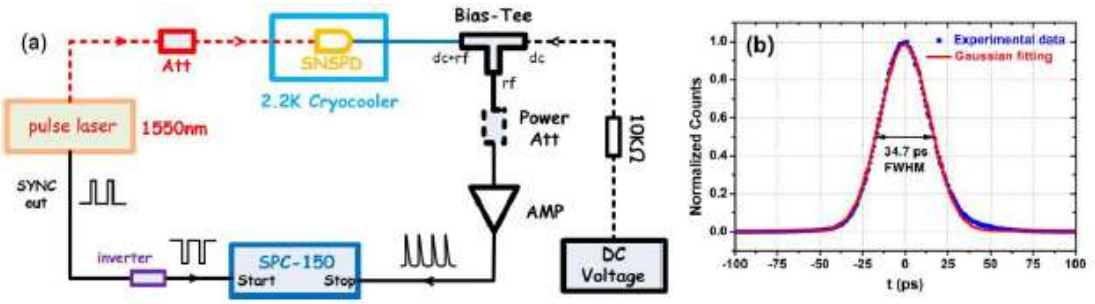

Fig.1.4 (a): TCSPC setup for jitter measurement of the SNSPD. (b) Experimental data for system jitter j_{system} = 34.7ps, and the corresponding Gaussian fitting curve [9].

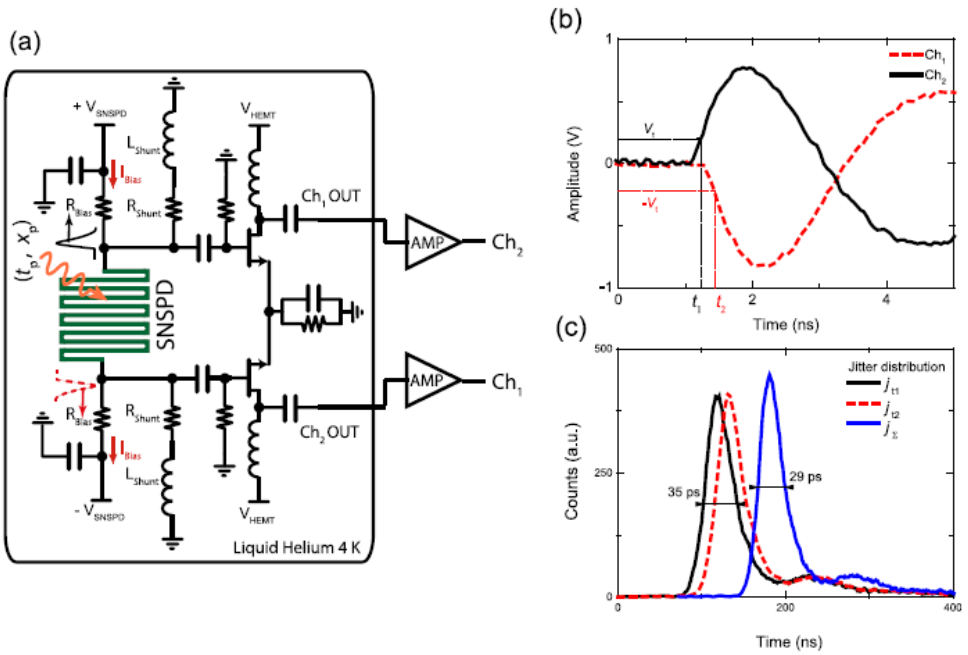

Fig.1.5 (a): Schematic of differential cryogenic HEMT (cut off all frequencies lower than 200 MHz) readout circuit with NbN SNSPD. (b) j_{t1} is jitter from Ch1, j_{t2} is time jitter from Ch2 and j is (t1+t2)/2 which is the time delay (t_p) of electronic circuit. (c) $\Delta j/2$ is $(j_{t2}-j_{t1})/2$ which is time jitter due to geometry of the SNSPD [10].

1.3.5 Dead time

The time that detector takes before going back to superconducting state from normal state after detection of photon and to become ready for detecting another photon is called dead time [1, 11]. The time taken by the device to go from superconducting state to normal state is called rise time and to come back from normal state to superconducting state is called fall time. Rise time is proportional to the kinetic inductance and inversely proportional to normal state resistance of the device [12]. Since the normal state resistance of the device is of the order of few kΩ, the rise time of the device is generally few hundreds of ps. whereas fall time is about few tens of nanosecond as in superconducting state the resistance of the device becomes zero and fall time solely depends on kinetic inductance [13] and on the load resistance (~50Ω). To minimize the dead time, it is important to keep the length of nanowire less and cross section area more so as the kinetic inductance of the nanostructure is reduced. Since many other factors are also dependent on the geometry of the nanostructure, it is desirable to design it accordingly.

1.3.6 Energy and photon number resolution capability

The area of hotspot increases with the energy of photons incident on the device. The photon count rate is linearly dependent on the photon flux incident on the device for very weak photon fluxes and it follows the trend within the single photon absorption regime. Since maintaining the intensity at a fixed level is difficult, the measured photon count rate can be normalized with respect to the curves obtained at known intensity and known wavelength. SNSPD lacks PNR capability and behaves like binary detector which can only confirm the presence or absence of photon. However, PNR capability can be incorporated by replacing single SNSPD by broadly illuminated array of detectors [14].

1.4 Established and emerging single photon detector technology

Single photon detector refers to a device that is capable of producing a measurable signal pulse after the absorption of a single photon of light. There are numerous established and emerging single photon detection technologies. The major thrust in this field is to improve the performance of the device. Photomultiplier tubes (PMTs) and single photon avalanche diodes (SPADs) are semiconductor based technologies. Whereas superconducting transition edge sensors (TESs), superconducting tunnel junctions (STJs) and superconducting nanowire single photon detectors (SNSPDs) are superconductor based technologies for single photon detection. The brief introduction with pros and cons of these technologies are described below:

1.4.1 Semiconductor based single photon detectors

1.4.1.1 Photomultiplier tubes (PMTs)

Fig.1.6 shows the picture of first photo-multiplier tube. Photomultiplier tubes are the first of this kind. Over the time this technology has grown to the extent of detecting single photons of wavelengths shorter than about 1μm. At longer wavelengths, however, due to the lower energy of the incident photons, initiation of the cascade process becomes difficult thus limits the performance of such devices.

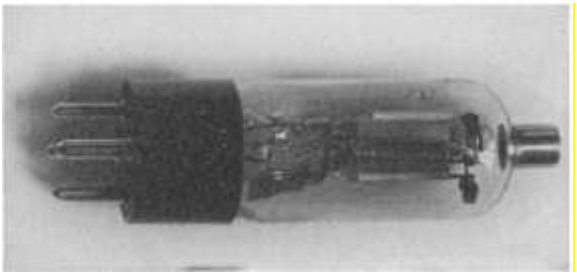

Fig.1.6: First photomultiplier tube [15].

1.4.1.2 Single photon avalanche diodes (SPADs)

Another technology for detection of single photons in the visible and near infrared wavelengths called avalanche photodiode (APD) is based on the principal of the avalanche breakdown process in silicon diodes [16]. In this case, the absorption of a single photon by a p-n junction biased close to its breakdown voltage can excite a single electron that accelerates and excites other electrons. This leads to a cascade breakdown and a measurable current through the junction. However, the operation of APDs is restricted only to the gated regime due to relatively high noise levels and after-pulsing as shown in Fig.1.7. Continuous improvements in the diode characteristics and the operating electronics, however, have seen new regimes and newer possibilities for future applications.

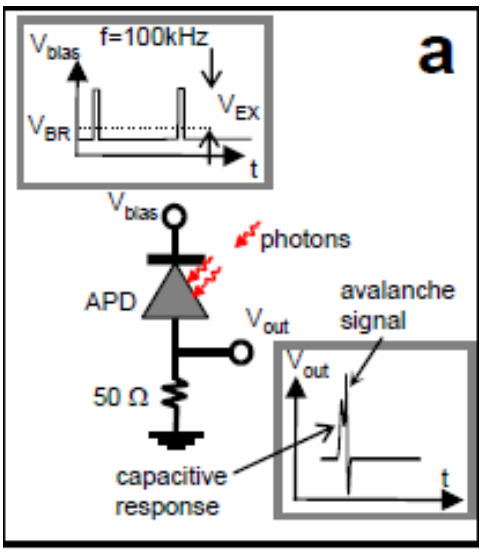

Fig.1.7: Voltage biased (Vbias: short voltage pulses, f: repetition frequency, level: (V_{BR}+V_{EX}) above the avalanche breakdown voltage V_{BR}) detector in gated Geiger mode with synchronized Photon pulses. Photon-induced output signal superposed upon the capacitive response of the APD to the applied bias detects only strong avalanches [17].

1.4.2 Superconductor based single photon detectors

A number of technologies based on superconductors have been developed for detecting single photon in optical as well as infrared regime. Major drawback of such devices is the requirements for a very low temperature down to few Kelvin. Nevertheless their superior performance compared to PMTs and APDs makes them attractive for specific applications.

1.4.2.1 Superconducting tunnel junctions (STJs)

In a typical superconducting tunnel junction (STJ), the absorption of a photon changes the current in a voltage biased junction by changing the concentration of quasiparticles in the absorbing film. The total current is proportional to the number and energy of the absorbed photons. STJs are used for X-ray detection but they can also be used in visible and infrared wavelength range. However, their operating temperature is in the range of mK. Also the performance of such detectors is limited by the slow count rate of (~10KHz) and large time jitter (≈1microsecond) [18] .

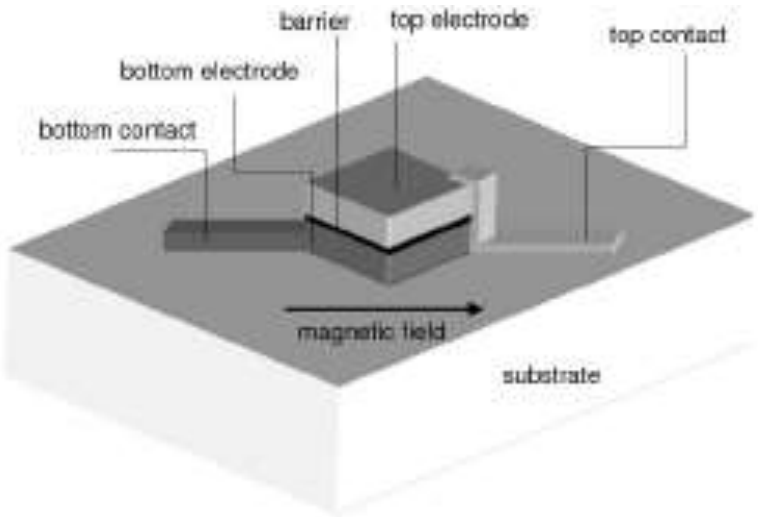

Fig.1.8: Schematic representation of a superconducting tunnel junction [18].

1.4.2.2 Superconducting transition edge sensors (TESs)

A transition edge sensor (TES), composed of a thin superconducting film, operates near its transition temperature. Fig.1.9 explains the working principle of the TES. The device is biased in such a way that it holds within the middle of the superconducting-normal metal phase transition [19, 21]. Therefore, even a negligible change in temperature can

causes a large change in resistance. An absorption of photon leads to a slight change in device temperature causing momentary and significant change of sensor resistance. The resultant change in the current flowing through the device can then be sensed. Although transition edge sensors (TES) offer very high detection efficiency (up to 95 %) [20] and zero dark counts, the main disadvantage of TES is its extremely low operating temperature in the range of 100 mK [21] and slow rise and fall times (100 ns and 15 µs respectively), limiting the maximum count rate to about 20KHz

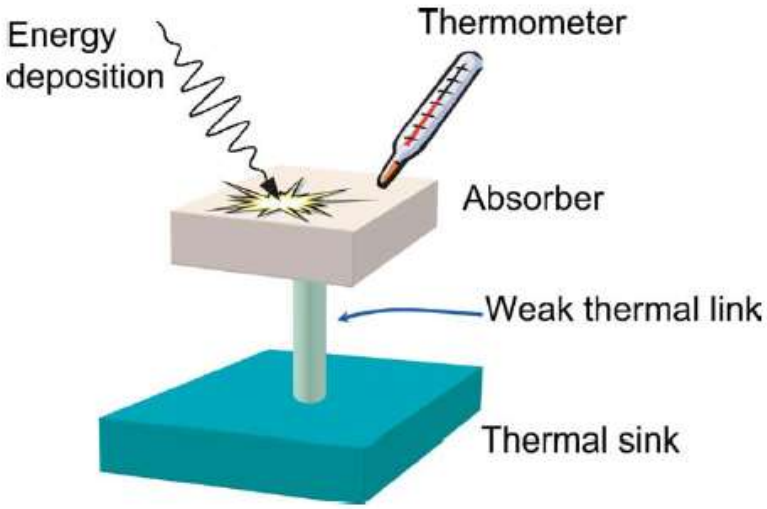

Fig.1.9: Tungsten electrons in Tungsten transition-edge sensors act as both the absorber and thermometer and voltage bias keeps them on the edge of the superconducting-to-normal transition. Precise thermometry is the outcome of steep dependence of resistance on temperature [19].

1.4.2.3 Superconducting nanowire single photon detectors (SNSPD)

A third type of detector known as superconducting nanowire single-photon detector (SNSPDs) has been developed recently. The SNSPD operates using the resistive region that appears in the superconducting wire (~100 nm wide and few nm thick) following absorption of a photon. This absorption creates a hot spot (a localized region with increased resistivity) that suppresses the superconductivity locally and a transient voltage pulse proportional to the number of absorbed photons is produced. The hotspot grows and eventually dissipates as it expands along the line. The voltage across the device falls back to zero and the device is ready for a new detection event.

Table.1.1: Comparison of performance metrices and related single photon detection technology

Detector	Operating temp	Spectral Range	SDE @1550nm	Dark Count	Time jitter	Count rate	Figure of merit
PMT	200K	1.7µm	2%	200kHz	300ps	10MHz	3.33×10^{2}
SPAD	200K	1.7µm	10%	91Hz	370ps	10kHz	2.97×10^{6}
TES	0.1K	4µm	95%	1Hz	100ns	100kHz	$9.6x10^{6}$
SNSPD	3K	5µm	0.7%	10Hz	60ps	100MHz	1.16×10^{7}
SNSPD	3K	5µm	67% 80%	10Hz 100Hz	105ps	10GHz	$6.38x10^{8}$

The device is capable of detecting single photon from visible to near infrared wavelength range. The device upto 97% detection efficiency has been reported by a group in NIST, USA and have reported 97% detection efficiency on W_xSi_{1-x} based SNSPD [22]. Table.1.1 incorporates the typical values of performance metrices and related available single photon detector for comparison [11].

1.4.2.3.1 Selection of substrate

The performance of SNSPD also relies on substrate material. Substrates with low energy gap provide large optical spectral range from ultraviolet to mid infrared. MgO, Sapphire, Si etc. are commonly used as substrate [23-26]. The hardness and mechanical strength of substrate material are also desirable. Better lattice match between superconducting materials and substrate promotes epitaxial growth resulting in superior superconducting properties in NbN and NbTiN in particular. Superconducting properties of amorphous materials such as W_xSi_{1-x} although does not depend much on lattice match with substrates, however substrates with low refractive index are preferred to enhance reflection of light from superconductor-substrate interface which in turn increases the absorption efficiency. Further, material which is electrically insulated, nevertheless good conductor of thermal load is preferred as substrate as it promotes heat dissipation [26].

1.4.2.3.2 Selection of superconducting material

Band gap of superconducting material is the deciding factor for spectral range sensitivity. Band gap energy is required to be less than the energy of photon to initiate the cascade process of pair breaking. The choice of superconducting material also depends on the available operating conditions and also the performance metrices for its compatibility as single photon detector in any specific applications. NbN was the first choice and mostly explored material for its performances. Many modifications in its fabrication and operating conditions were tried to improve its performance [2-4, 6-7, 13-15, 25]. Many other materials were also tried in the direction to improve the performance of the device. NbTiN shows less response time due to its low resistivity and hence low inductance value [24]. W_xSi_{1-x} has low energy band gap and hence better sensitivity at higher wavelength. But these materials have low Tc and hence require advanced cooling technique down to mK [26].

1.4.2.3.3 Selection of dimension

The dimensions of superconducting nanostructures play an important role in single photon detection. When the thickness of the film is of the order of coherence lengths, the Tc reduces due to proximity effect and number of density states decreases with increasing disorder [28]. The absorption efficiency ($\eta_{absorption}$) of the meander depends on its width, thickness and filling factor and on the polarization of the incident light [27]. The detection efficiency ($\eta_{DDE} = \eta_{intrinsic} \times \eta_{absorption}$) increases as the absorption efficiency of meander increases. The absorption by meander decreases with film thickness towards infrared. Another important aspect as reported the dark count grows and start dominating when bias current > 0.97Ic. On the other hand decreasing the bias current to circumvent the issue with higher dark count leads to decrease in short wavelength plateau which vanishes at $I_B < 0.7Ic$. Further, reported data shows that detection efficiency remains constant with increase in thickness up to certain limit beyond which it starts to decrease linearly. The trend is different at near infrared range. Detection efficiency decreases linearly as the thickness of superconducting layer increases. This indicates that there are two different mechanisms for detection of photons. One is called hotspot detection mechanism and another one is fluctuation assisted detection. In hotspot model the growth of the hotspot depends on the applied

bias current ($\delta n_S/n_S=1-I_B/ Ic_D$), and thermal coupling between substrate and superconductor. Change in Cooper pair concentration (δn_S) required for appearance of resistive nucleus is dependent on the minimum energy of photon absorbed (E_{ph}) where E_{ph} follows as:

$$\mathbf{E_{ph} = [\sqrt{\pi}/\delta][N_o \Delta^2 wd (D\tau_{th})^{1/2} (1-I_B/Ic_D).} \quad \mathbf{(1.4)}$$

Here δ is efficiency of quasiparticle multiplication process, N_o is electron density of states and τ_{th} is time constant of quasiparticle thermalization. In the eqn. (1.4) minimum required energy is dependent on nanowire width (W), thickness (d), diffusion coefficient (D) and change in Cooper pair concentration (I_B / Ic_D)) [28]. The existence of the η_D beyond cut off wavelength shows the detection of photons by some other phenomena also. When the energy of the absorbed photon is less than the energy gap of the material, it reduces the barrier height for vortex motion. The barrier height is proportional to the thickness and width of the film and bias current.

1.5 Evolution of device and state of the art

Ever since the discovery of the first SNSPD, researchers around the world have been working on to improve the performance metrics of the devices for practical uses.

Gol'tsman, et al. [29] reported on devices in the form of straight bridge of 0.2μm wide NbN stripe and later on 0.2μm wide meander type line covering the 4μm x 4μm area to enhance the detection efficiency. The detector's active area was increased by the factor of 80, while the quantum efficiency increased only 20 times which is about 5% of the intrinsic efficiency. It has been concluded that the observed decrease in the meander device performance could be due to the lack of uniformity of the device width over the very long length of the meander stripe. In order to improve the performance metrics, large area meander SNSPDs have been developed to improve the coupling efficiency and hence the practical detection efficiency [4, 30]. A method had been developed for fabrication of very large 20μm x 20μm meander area from ultrathin epitaxial NbN films. They were successful in synthesizing a highly uniform nanowire with a low probability of constrictions over large area and lower kinetic inductance [31].

To further improve the performance in terms of detection efficiency of the device an optical cavity and anti-reflection coating to a nanowire photodetector has been added to boost the absorption efficiency [2]. Rosfjord et al. have demonstrated detection efficiencies of 57% at 1550nm and 67% at 1064nm.

Tanner et al. explored new materials and substrates for improved fabrication versatility, higher detection efficiency, and lower dark counts [24]. They reported the performance of packaged NbTiN SNSPDs fabricated on oxidized silicon substrates in the wavelength range from 830 to 1700nm. Constructive interference from the SiO_2/Si interface to achieve enhanced front-side fibre-coupled detection efficiency of 23.2 % at 1310nm, at 1 kHz dark count rate, with 60 ps full width half maximum timing jitter has been reported.

One more step has been taken to enhance absorption efficiency by illuminating the optical coupled SNSPDs from the rear side through the substrate and with small-gradient index lenses to reduce the beam waist at a distance from the exit end [25, 32]. For efficient coupling, the devices were installed in compact fibre-coupled packages and the substrate thickness was reduced from 400 to 45 μm using mechanical polishing method. Optical coupling efficiency of ~98% was achieved in a 15 μm × 15 μm device. NIST, USA however integrated SNSPDs with an optical cavity design for front-side illumination [33]. Using a confocal optical scanning technique, significant enhancement of optical absorptance of 73% in comparison with 20% in a typical bare nanowire device at 1550nm and 3K has been reported.

Monolithic integration with GaAs/AlAs microcavities, leads to enhanced quantum efficiency. SSPDs fabricated and measured on GaAs/AlAs Bragg mirrors, show a clear cavity enhancement with increased quantum efficiency [34]. Integration of optical nano-antennae with an SNSPD was performed to enhance the efficiency and speed of photodetection at the quantum level [35].

Passive quantum photonic integrated circuits were also demonstrated to improve device performance. Superconducting nanowires on GaAs ridge waveguide is reported to provide high efficiency (~20%) at telecom wavelengths, high timing

accuracy (~60 ps), and response time in the ns range and are fully compatible with the integration of single-photon sources, passive networks, and modulators [36, 37].

Hu et al. have proposed a photonic structure that can increase the nanowire optical absorptance without increasing the active length of the detector, thus achieving good efficiency without compromising the speed of the detector. The concept of nano-antennae integration and the mechanism of absorption enhancement have been studied in detail. This antenna-assisted coupling enables a SNSPD (9μm x 9μm active area) with 47% device efficiency at telecom wavelengths while maintaining a reset time of only 5ns [35].

Although SNSPD has been successfully demonstrated for telecom wavelengths its extension to mid-infrared wavelength was restricted due to its low sensitivity above 2μm. A new concept has been adopted recently [25] by rearranging the wires used in meandered SSPDs to a parallel configuration. This configuration decreases the detector inductance and increases the signal amplitude, while keeping the good sensitivity and maintaining the same dark count rate. The new device exhibits 10 times better quantum efficiency at 3.5μm than the standard SNSPD [38].

A photon number resolving (PNR) detector with high count rate and precise time resolution is useful in many applications, such as high sensitivity optical communication, laser radar, and fluorescence measurement techniques. PNR detectors based on parallel superconducting nanowires and capable of counting up to four photons at telecommunication wavelengths, with an ultralow dark count rate and high counting frequency has been demonstrated [38]. Results on a two elements SNSPD shows sub 50ps relative timing jitter, and four times the maximum counting rate of a single SNSPD with the same active area [39]. A photon-number-resolving detector based on a four-element superconducting nanowire single photon detector is demonstrated to have sub 30ps resolution [40].

Apart from fabrication and patterning of the device, it was found that selection of material is also an important factor for improving the device performance.

SNSPDs based on NbN although played a crucial role in high-fidelity quantum optics measurements due to their sensitivity over a broad range of wavelengths, low dark

count rate, and high timing resolution. However, the low quantum efficiency has been the limiting factor in many correlation-type measurements.

Device based on an amorphous W_xSi_{1-x} thin film seems to have great potential to overcome such limitations due to its smaller superconducting gap and low electron density. Moreover, excellent structural homogeneity and the absence of grain boundaries could be advantageous and may lead to higher internal quantum efficiency in amorphous films of W_xSi_{1-x} [26].

Dorenbos et al. demonstrated performance of detectors based on NbTiN thin films on a silicon substrate. NbTiN ultra-thin films have several favorable features for use in SNSPDs like better lattice matching with MgO substrates, lower resistivity than NbN thin films and most importantly less kinetic inductance, 25% lower than that of NbN-SNSPD. The low dark count rate by a factor of 10 compared to identical NbN detectors reduces a noise equivalent power to 10^{-19} W $Hz^{-1/2}$ at 4.2K. Lower dark count rate in NbTiN detectors is believed to be due to better homogeneity of the superconducting parameters compared to NbN [41]. Moreover, the superconducting properties of NbTiN thin films can be tuned by changing the composition of the NbTi target which would allow further optimization of the superconducting properties to improve device performance [24].

Fabrication of ultrathin nanowires of superconducting YBCO with Focused Ion Beam (FIB) milling technique is reported with the purpose of developing high-T_c superconducting photon detectors [42]. However, sensitivity down to single-photon detection at visible or infrared is a big question as the high-T_c superconducting materials have a large superconducting gap energy compared to NbN.

An important issue in this direction is to obtain large area coverage while retaining a high quantum efficiency and maximum count rate. SNSPDs have been realized using an innovative parallel wire configuration. This configuration is advantageous as it provides a large detection area, fast response, and large signal amplitudes [40, 43, 44]. Fig.1.10 below shows the evolution of the SNSPD device since beginning to improve its performance.

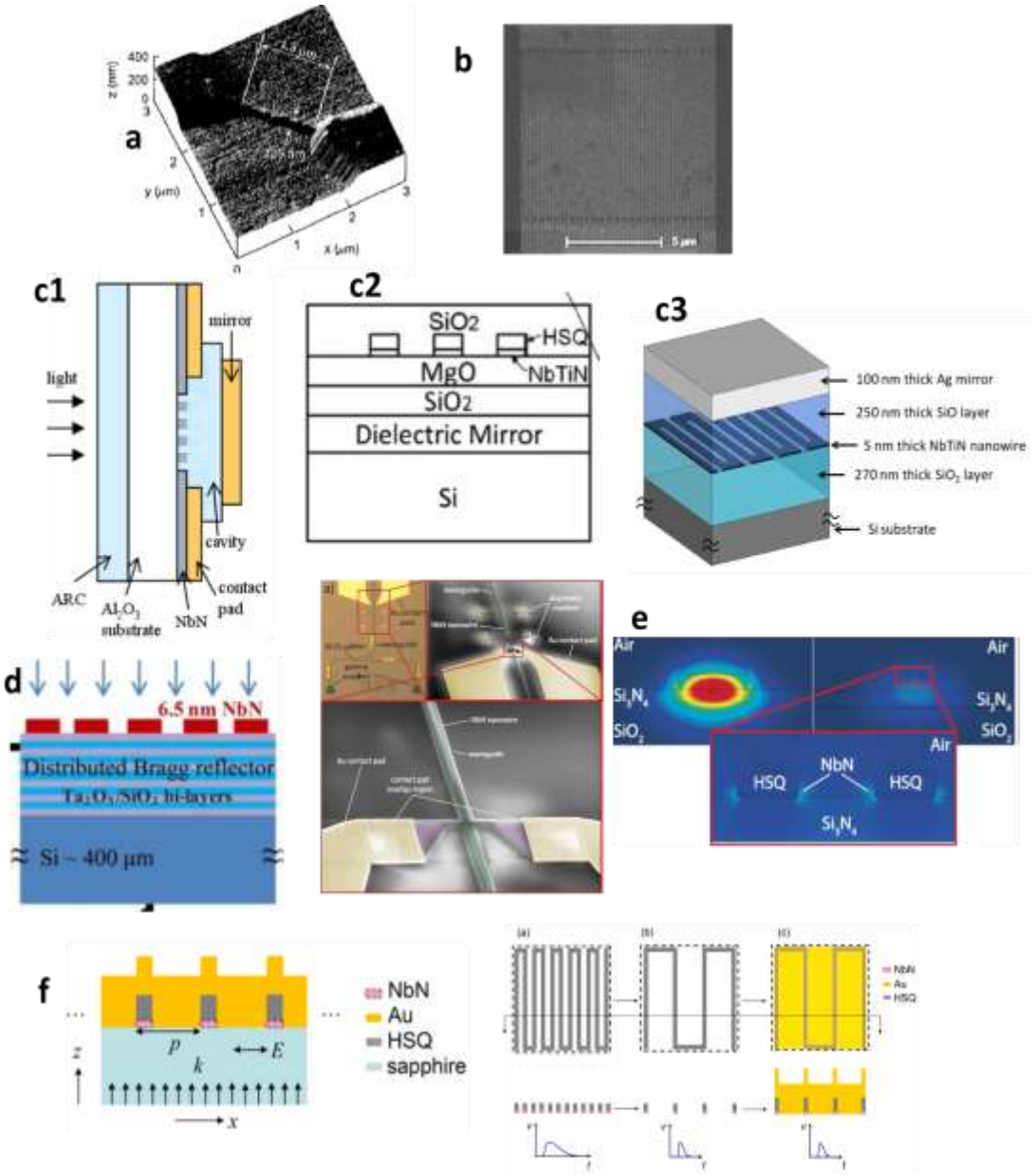

Fig.1.10: Evolution of device (a) AFM image of a 1.3µm x 0.23µm simple-bridge device (Single nanowire) [29]. (b) Meander structure to enhance coupling efficiency [1] (c1) Single photon detector integrated with an optical cavity and anti-reflection coating (ARC) to reduce transmission and reflection of photons [2]. (c2) Optical cavity SNSPD layer structure (thicknesses: SiO_2: 45nm, HSQ: 30nm, NbTiN: 4.5nm, MgO: 20nm, and SiO_2: 246nm from top to bottom) [33]. (c3) Schematic configuration of NbTiN SSPD on thermally oxidized Si substrate [41]. (d) SNSPD on Distributed Bragg Reflector/ Si substrate [45] (e) Waveguide structure of a nanophotonic circuit with integrated SNSPD device. Inset: SEM micrograph of the detector area with metal alignment mark and zoom into the waveguide region with NbN nanowire on top [36]. (f) optical antenna to enhance absorption efficiency, fabricate the HSQ structure and put gold on top to collect the incident photons [35].

1.6 Applications of single photon detectors

Photon counting devices have applications in various fields which utilizes particularly photon detection/ photon counting characteristic of the device. Since SNSPD has shown better performance in comparison to other available SPD technologies, the demand for its utilization in various fields like quantum key distribution (QKD), optical quantum computing (OQC), photon source characterization and light detection and ranging (LIDAR) applications is continuously increasing. Few application areas of SNSPD have been described below.

1.6.1 Quantum key distribution (QKD)

The quantum key distribution is a part of quantum cryptography in which the sender and the receiver of data acquire some secret key which is very difficult for intruders to know. The 1550nm wavelength is used for loss free transmission in long distance communication. Low DCR and low time jitter are the features which enhances the transmission rate of bits in teleportation. QKD over 200km distance has been achieved at 10GHz clock rate using SNSPD [46]. The application of SNSPD based QKD setup can be seen in Fig.1.11 (a, b). Fig.1.11 (a) shows the setup (source) for generating the signal and idler photons. Fig.1.11 (b) shows the receiver unit of the QKD where the signal and input photons are passed through polarization controller then fibre coupler followed by SNSPD1 and SNSPD2. The idler photon is received by another MZI after travelling 102 km of distance followed by SNSPD3 and SNSPD4.

Details of few QKD demonstrations along with the transfer distance attenuation, operating temperature and bit transfer rate are enlisted in the table.1.2 as given below.

Table.1.2: Summary of notable QKD demonstrations, outlining the maximum achievable distance and the level of security:

Quantum channel			Detector		Security		
	Distance (km)	**Attenuation (dB)**	**Type**	**Temperature (K)**	**Protocol**	**Attacks**	**r_{sec} (bps)**
Wang 2012	260	52.9	SNSPD	1.7	DPS	Individual	1.85
Stucki 2009	250	42.9	SNSPD	2.5	COW	Collective	15
Takesue 2007	200	42.1	SNSPD	3.0	DPS	Individual	12.1
Liu 2010	200	--	SNSPD	2.4	BB84	Collective	15
Rosenberg 2009	135	27.8	SNSPD	3.0	BB84	Collective	0.2
Shimizu 2014	90	30	SNSPD	2.5	DPS	Individual	1100

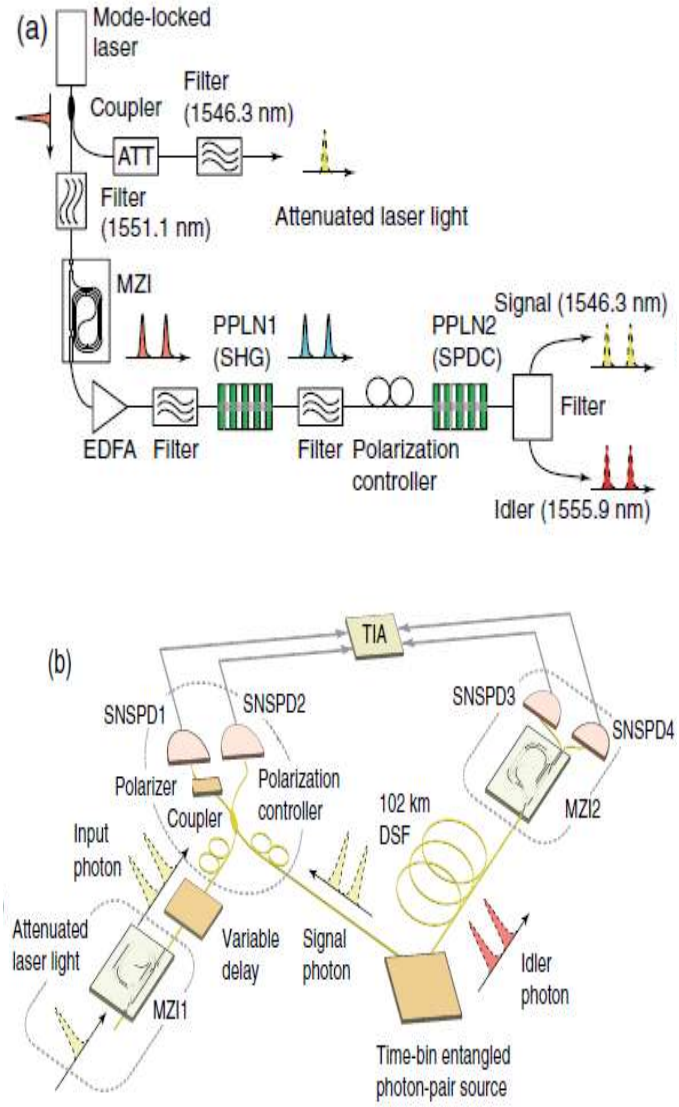

Fig.1.11: (a) Setup for generating time-bin entangled photon pairs. (b) Quantum teleportation setup [47]. (Yellow lines: optical fibers; Gray line: electrical lines, ATT: attenuator; EDFA: erbium-doped fiber amplifier; PPLN: periodically poled lithium niobate waveguide; SHG: second-harmonic generation; SPDC: spontaneous parametric down conversion; MZI: unbalanced Mach–Zehnder interferometer; DSF: dispersion-shifted fiber; TIA: time interval analyzer).

1.6.2 Light detection and ranging (LIDAR)

SNSPDs may also be ideal candidates for use in LIDAR (light detection and ranging) with visible/near infrared light for precise location and to generate large amounts of data about the physical layout of landscape features. Fig.1.12 explains photon-

counting depth imaging system. Few photons get reflected by a reference reflector and others come back after getting reflected from target. The time gap get registered between these two bunches of photons after detection by SNSPD and thus determines the distance of the target from detector.

1.6.3 Photon number resolving detector (PNRD)

A photon number resolving detector is capable of detecting number of photons striking detector at a particular time. TES and STJ have intrinsic energy resolving capability and can be considered as PNR detector. However SNSPD acts as binary detector and can only detect the presence or absence of photons. These detectors can be made PNR by adding this features using time multiplexing or spatial multiplexing [49].

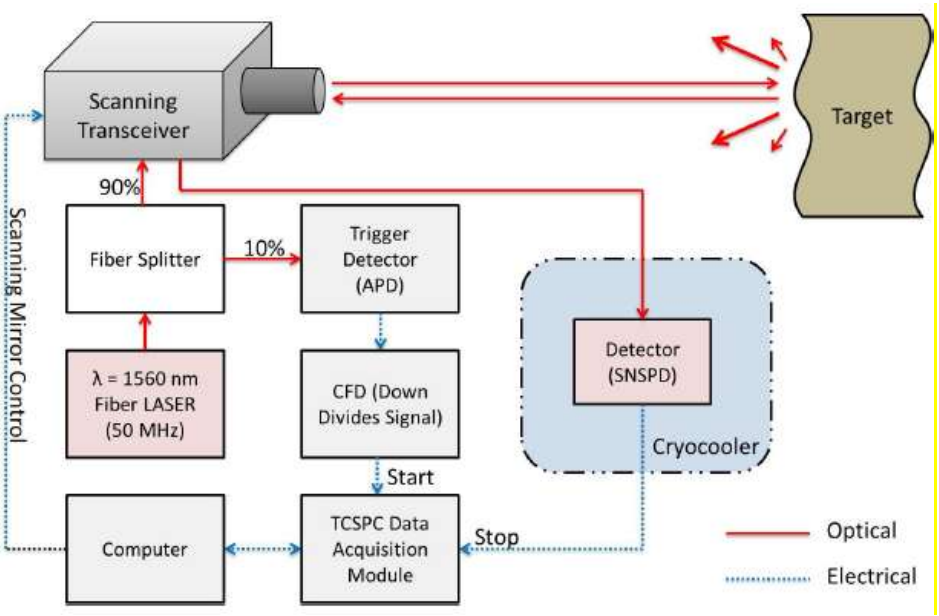

Fig.1.12: Superconducting nanowire single-photon detector (SNSPD) based photon-counting depth imaging system illuminated by a sub-picosecond 1560nm wavelength source [48].

As for an example, the electrical equivalent circuit of 24 pixel PNRD is shown in Fig.1.13.A (a) and the SEM image of the same can be seen in Fig.1.13.A (b). The histogram of the output signals obtained at different input light power can be seen in Fig.1.13.B (a) which is depicted using colour map. Fig.1.13.B (b) and 1.13.B (c) show two of these histograms at two different input power levels. The probability of

absorption of two or more photons in a single nanowire section increases with the more number of input photons falling on the device. This is the reason for the device showing saturation after crossing the some number of photons detection which is less than the total number of input photons falling on the device [50].

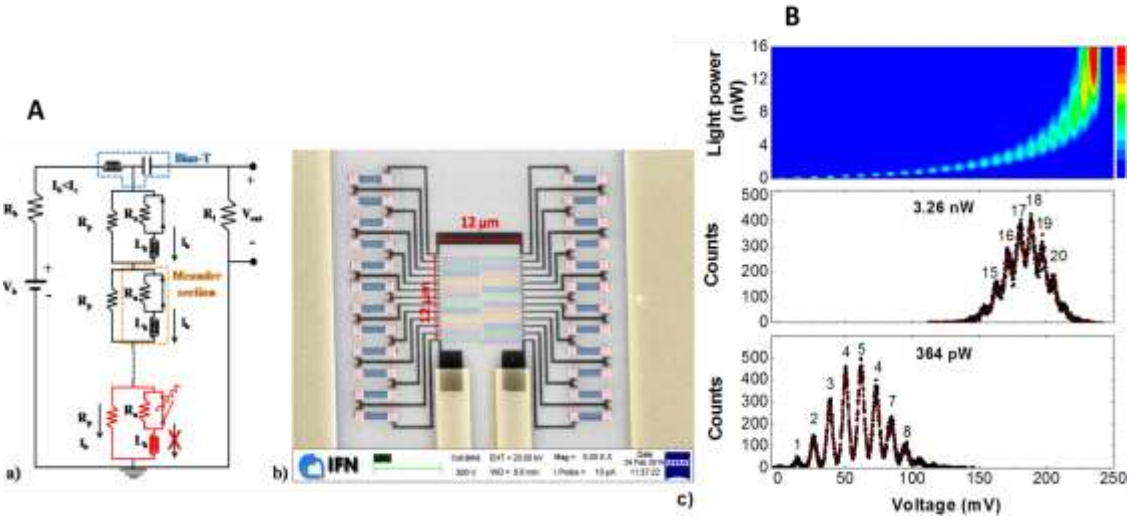

Fig.1.13: A (a) Series photon number resolving detector represented by Electrical equivalent circuit. Superconducting nanowire sectionh, in orange box shows superconducting state and in red box shows normal state after photon absorption, is connected with parallel resistance Rp fabricated on chip. b) Scanning electron microscopy image of a 24-pixel-PNRD fabricated on Silicon oxide on Si and Au–Pd parallel resistors (blue in the image). The nanowire width is 100nm with a filling factor of 40%. Fig.1.13.B (a) Histograms of the output signals from device at bias current I_B = 19.0 µA with different light powers in the range 0-15nW. Twenty-five distinct output levels with respect to the detections of 0-24 photons are visible. (b) and (c) histograms at fixed light powers of 3.26nW and 64pW respectively.

1.7 Outline of the thesis

The above discussion has broadly outlined the scope of the present thesis. The motivation behind the present study is twofold;

- Designing and optimization of process parameters from the perspective of single photon detection for both visible and infrared regime.
- Designing and optimization of process parameters from the perspective of establishment of quantum metrology standard in India.

The layout of the thesis is as follows:

The work is divided in five parts namely (i) basic understanding about the device, its working principle, application, properties and comparison with already existing technologies; (ii) study of readout circuit; (iii) facility creation for low temperature measurements; (iv) optimization of process parameters for thin film fabrication and characterization; (v) optimization of process parameters for nanowire fabrication in the form of meander structure using EBL and FIB and its characterization and finally (vi) conclusion/ future aspects.

Chapter 1 is the discussion about single photon detectors and its various important performance matrices e.g. detection efficiency, dark count rate, response time, time jitter, spectral sensitivity etc. There are continuous research efforts worldwide in this field to improve the device performance. The performance of SNSPD is compared with other already existing single photon detectors. The chapter discusses in detail about the evolution of SNSPDs from straightforward single nanowire to state-of-the-art configurations and many technological challenges associated with device fabrications. Few applications of SNSPDs are discussed in detail afterwards.

Chapter 2 explains about the operation of SNSPD devices. The various components to be used in readout circuit at room temperature as well as cryogenic temperature are discussed. The electrical model of the device is simulated using microwave simulation software. The transient response and S-parameters are studied using different circuits.

Chapter 3 explains in details about the low temperature measurements system. The designing of the cryostat took into consideration many factors namely, the minimum operating temperature, temperature stability, special arrangement for measurement at microwave frequency, light shining and alignment of fibre with micron size devices, arrangement for DC measurements, shielding of the device from any outside electromagnetic noise etc. Overall setup for electrical as well optical are discussed.

Chapter 4 describes synthesis of high quality ultrathin superconducting NbN films using DC magnetron sputtering. It explains the effect of pressure, temperature and sputter parameters on thin film fabrication and its optimization. Thin film

characterization at low temperature is carried out. Results of low temperature transport measurements are discussed.

Chapter 5 discusses designing and fabrication of superconducting meander line nanoarrays using the two standard techniques – electron beam lithography (EBL) and focused ion beam (FIB) milling. Electrical characterizations such as measurements of superconducting transition temperature, transition width, critical current density etc. of superconducting nanostructures are carried out and discussed.

Chapter 6 presents a brief summary of important results and scope for improvements. It also discusses some issues which are potentially interesting for further studies.

1.8 References

[1] C. M. Natarajan, M. G. Tanner and R. H. Hadfield, "Superconducting nanowire single-photon detectors: physics and applications", Supercond. Sci. Technol. **25**, 063001 (2012).

[2] K. M. Rosfjord, J. K. W. Yang, E. A. Dauler, A. J. Kerman, V. Anant, B. M. Voronov, G. N. Gol'tsman, and K. K. Berggren, "Nanowire Single-photon detector with an integrated optical cavity and anti-reflection coating", Optics Express **14**, 527-534 (2006).

[3] A. Korneev, P. Kouminov, V. Matvienko, G. Chulkova, K. Smirnov, B. Voronov, G. N. Gol'tsman, M. Currie, W. Lo, K. Wils, J. Zhang, W. S ysz, A. Pearlman, A.Verevkin, Roman Sobolewski, "Sensitivity and gigahertz counting performance of superconducting single-photon detectors", Appl. Phys. Lett. **84,** 5338 (2004).

[4] A. Verevkin, J. Zhang and R. Sobolewski, "Detection efficiency of large-active-area NbN single-photon superconducting detectors in the ultraviolet to near-infrared range", Appl. Phys. Lett. **80**, 25 (2002).

[5] K. Il'in, M. Siegel, A. Engel, H. Bartolf, A. Schilling, A. Semenov, H.-W. Huebers, "Current-Induced Critical State in NbN Thin-Film Structures", J Low Temp Phys **151**, 585 (2008).

[6] M Hofherr, D Rall, K S Ilin, A Semenov, N Gippius and H-W Hübers and M Siegel, "Superconducting nanowire single-photon detectors: Quantum Efficiency vs. thickness of NbN films", Journal of Physics Conf. Series (SuST) **234**, 012017 (2010) .

[7] A. Engel, A. Semenov, H-W. H¨ubers, K. Il'in, and M. Siegel, "Fluctuation effects in superconducting nanostrips", phys. stat. sol. (c) **2**, 5 (2005).

[8] J. Kitaygorsky, J. Zhang, A. Verevkin, A. Sergeev, A. Korneev, V. Matvienko, P. Kouminov, K. Smirnov, B. Voronov, G. Gol'tsman, and R. Sobolewski, "Origin of Dark Counts in Nanostructured NbN Single-Photon Detectors", IEEE Trans. Appl. Supercond. **15**, 545 (2005).

[9] L. You, X. Yang, Y. He, W. Zhang, D. Liu, W. Zhang, L.Zhang, L.Zhang, X. Liu, S.Chen, Z. Wang, X. Xie, "Jitter analysis of a superconducting nanowire single photon detector", AIP Advances **3**, 072135 (2013).

[10] N. Calandri, Q.Y. Zhao, D. Zhu, A. Dane, and K.K.Berggren, "Superconducting nanowire detector jitter limited by detector geometry", Appl. Phys. Lett. **109**, 152601 (2016).

[11] R. H. Hadfield, "single-photon detectors for optical quantum information applications", Nature Photonics **3**, 696 (2009).

[12] J. K. W. Yang, E. Dauler, A. Ferri, A. Pearlman, A. Verevkin, G. Gol'tsman, B. Voronov, R. Sobolewski, W. E. Keicher, K. K. Berggren, "Fabrication Development for Nanowire GHz-Counting-Rate Single-Photon Detectors", IEEE Trans. Appl. Supercond. **15**, 626 (2005).

[13] A. J. Kerman, E. A. Dauler, W. E. Keicher, J. K. W. Yang, K. K. Berggren, G. N. Gol'tsman, and B. M. Voronov, "Kinetic-inductance-limited reset time of superconducting nanowire photon counters", Appl. Phys. Lett. **88**, 1111161 (2006).

[14] F. Marsili, F. Najafi, C. Herder, and K. K. Berggren, "Electrothermal simulation of superconducting nanowire avalanche photodetectors", Appl. Phys. Lett. **98**, 093507 (2011).

[15] H. E. Iams and B. Salzberg, "The secondary emission phototube", Proc. IRE **23**, 55 (1935).

[16] D. Achilles, C. Silberhorn, C. Sliwa, K. Banaszek, and I. A. Walmsley, "Fiber-assisted detection with photon number resolution", Optics Letters **28**, 2387 (2003).

[17] B. E. Kardyna, Z. L. Yuan and A. J. Shields, "An avalanche-photodiode-based photon-number-resolving detector", Nature Photonics **2**, 425 (2008).

[18] D.D.E. Martin and P. Verhoeve, "Superconducting tunnel junctions", Advanced Studies and Technology Preparation Division, ESA-ESTEC, The Netherlands.

[19] D. Rosenberg, A. E. Lita, A. J. Miller and S W Nam, "Noise-free high-efficiency photon-number-resolving detectors", Phys. Rev. A **71**, 061803 (2005).

[20] S. W. Nam, B. Cabrera, P. Colling, R. M. Clarke, E. Figueroa-Feliciano, A. J. Miller, R. W. Romani, "A new biasing technique for transition edge sensors with electrothermal feedback", IEEE Trans. Appl. Supercond. **9**, 4209 (1999).

[21] D. Rosenberg, A. E. Lita, A. J. Miller, S. Nam, and R. E. Schwall, "Performance of Photon-Number Resolving Transition-Edge Sensors With Integrated 1550 nm Resonant Cavities", IEEE Trans. Appl. Supercond. **15**, 575 (2005).

[22] F. Marsili, V. B. Verma, J. A. Stern, S. Harrington, A. E. Lita, T. Gerrits, I. Vayshenker, B. Baek, M. D. Shaw, R. P. Mirin and S. W. Nam, "Detecting single infrared photons with 93% system efficiency", Nature Photonics 7, 210 (2013).

[23] J Wu, L X You, L Zhang, W J Zhang, H Li, X Y Liu, H Zhou, Z Wang, X M Xie, Y X Xu, W Fang and L M Tong, "NbN superconducting nanowire single-photon detector fabricated on MgF2 substrate", Supercond. Sci. Technol. **29**, 065011 (2016).

[24] M. G. Tanner et al., "Enhanced telecom wavelength single-photon detection with NbTiN superconducting nanowires on oxidized silicon", Appl. Phys. Lett. **96**, 221109 (2010).

[25] S. Miki, T. Yamashita, M. Fujiwara, M. Sasaki, and Z. Wang, "Multichannel SNSPD system with high detection efficiency at telecommunication wavelength", Opt. Lett. **35**, 2133 (2010).

[26] V. B. Verma, B. Korzh, F. Bussières, R. D. Horansky, A. E. Lita, F. Marsili, M. D. Shaw, H. Zbinden, R. P. Mirin, and S. W. Nam, "High-efficiency WSi superconducting nanowire single-photon detectors operating at 2.5 K", Appl. Phys. Lett. **105**, 122601 (2014).

[27] V. Anant, A. J. Kerman,2 E. A. Dauler, J.K.W.Yang, K. M. Rosfjord, and K. K. Berggren, "Optical properties of superconducting nanowire single-photon detectors", Optics Express **16**, 14 (2008).

[28] Influence of Material and Geometry on the Performance of Superconducting Nanowire Single-Photon Detectors by Henrich, Dagmar, (2013).

[29] G. Gol'tsman, O. Okunev, G. Chulkova, A. Lipatov, A. Dzardanov, K. Smirnov, A. Semenov, B. Voronov, C. Williams, and R. Sobolewski, "Fabrication and Properties of an Ultrafast NbN Hot-Electron Single-Photon Detector", IEEE Trans. Appl. Supercond. **11**, 574 (2001).

[30] G. Bachar, I. Baskin, O. Shtempluck, and E. Buks, "Superconducting nanowire single photon detectors on-fiber", Appl. Phys. Lett. **101**, 262601 (2012).

[31] S. Miki S, M. Fujiwara, M. Sasaki, B. Baek, A. J. Miller, R. H. Hadfield, S. W. Nam, and Z. Wang, "Large sensitive-area NbN nanowire superconducting single-photon detectors fabricated on single-crystal MgO substrates", Appl. Phys. Lett. **92**, 061116 (2008).

[32] S. Miki, M. Takeda, M. Fujiwara, M. Sasaki, and Z. Wang, "Compactly packaged superconducting nanowire single-photon detector with an optical cavity for multichannel system", Opt. Express **17**, 23557 (2009).

[33] B. Baek, J. A. Stern, and S. W. Nam, "Superconducting nanowire single-photon detector in an optical cavity for front-side illumination", Appl. Phys. Lett. **95**, 191110 (2009).

[34] A. Gaggero A et al., "Nanowire superconducting single-photon detectors on GaAs for integrated quantum photonic applications", Appl. Phys. Lett. **97**, 151108 (2010).

[35] X. Hu, E. A. Dauler, R. J. Molnar, and K. K. Berggren, "Superconducting nanowire single-photon detectors integrated with optical nano-antennae", Opt. Express **19**, 17 (2011).

[36] O. Kahl, S. Ferrari, V. Kovalyuk, G. N. Goltsman, A. Korneev, and W. H. P. Pernice, "Waveguide integrated superconducting single-photon detectors with high internal quantum efficiency at telecom wavelengths", Sci. Reports 5, 10941 (2015).

[37] J. P. Sprengers, A. Gaggero, D. Sahin, S. Jahanmirinejad, G. Frucci, "Waveguide superconducting single-photon detectors for integrated quantum photonic circuits", Appl. Phys. Lett. **99**, 181110 (2011).

[38] A. Divochiy, F. Marsili, D. Bitauld, A. Gaggero, R. Leoni, F. Mattioli, A. Korneev, V. Seleznev, N. Kaurova, O. Minaeva, G. Gol'tsman, K. G. Lagoudakis, M. Benkhaoul, F. Levy and A. Fiore, "Superconducting nanowire photonnumber-resolving detector at telecommunication wavelengths", Nature Photon. **2**, 302 (2008).

[39] E. A. Dauler, B. S. Robinson, A. J. Kerman, J. K. W. Yang, E. K. M. Rosfjord, V. Anant V, B. Voronov, G. Gol'tsman, and K. K. Berggren, "Multi-Element Superconducting Nanowire Single-Photon Detector", IEEE Trans. Appl. Supercond. **17**, 279 (2007).

[40] E. A. Dauler, A. J. Kerman, B. S. Robinson, J. K. W. Yang, B. Voronov, G. Gol'tsman, S. A. Hamilton, and K. K. Berggren, "Photon-number-resolution with sub-30-ps timing using multi-element superconducting nanowire single photon detectors", J. Mod. Opt. **56**, 364 (2009).

[41] S.Miki, T.Yamashita, H.Terai, and Z.Wang, "High performance fiber-coupled NbTiN superconducting nanowire single photon detectors with Gifford-McMahon cryocooler", Opt. Express **21**, 10208 (2013).

[42] N. Curtz, E. Koller, H. Zbinden, M. Decroux, L. Antognazza, O. Fischer, and N. Gisin, "Patterning of ultrathin YBCO nanowires using a new focused-ion-beam process", Supercond. Sci. Technol. **23**, 045015 (2010).

[43] M. Ejrnaes, A. Casaburi, O, Quaranta, S. Marchetti, A. Gaggero A, F. Mattioli, R. Leoni, S. Pagano, and R. Cristiano, "Characterization of superconducting pulse discriminators based on parallel NbN nanostriplines", Supercond. Sci. Technol. **22**, 055006 (2009).

[44] M. Ejrnaes, A. Casaburi, R. Cristiano, O. Quaranta, S. Marchetti, N. Martucciello, S. Pagano, A. Gaggero, F. Mattioli, R. Leoni, P. Cavalier, and J. C. Villégier, "Timing jitter of cascade switch superconducting nanowire single photon detectors", Appl.Phys. Lett. **95**, 132503 (2009).

[45] W. J. Zhang, H. Li, L. X. You, Y. H. He, L. Zhang, X.Y. Liu, X. Y. Yang, J. J. Wu, Q. Guo, S. J. Chen, Z. Wang, and X. M. Xie, "Superconducting nanowire single-photon detectors at a wavelength of 940 nm", AIP Advances 5, 067129 (2015).

[46] H. Takesue, S. W. Nam, Q. Zhang, R. H. Hadfield, T. Honjo, K. Tamaki & Y. Yamamoto, "Quantum key distribution over a 40-dB channel loss using superconducting single-photon detectors", Nature Photonics **1**, 343 (2007).

[47] H. Takesue, S. D. Dyer, M. J. Stevens, V. Verma, R. P. Mirin and S. W. Nam, "Quantum teleportation over 100 km of fiber using highly efficient superconducting nanowire single-photon detectors", Optica **2**, 10 (2015).

[48] A. McCarthy, N. J. Krichel, N. R. Gemmell, X. Ren, M. G. Tanner, S. N. Dorenbos, V. Zwiller, R. H. Hadfield and G. S. Buller, "Kilometer-range, high resolution depth imaging via 1560 nm wavelength single-photon detection", Optics Express **21**, 7 (2013).

[49] A. E. Lita, D. Rosenberg, S. Nam, A. J. Miller, D. Balzar, L. M. Kaatz, and R. E. Schwall, "Tuning of tungsten thin film superconducting transition temperature for fabrication of photon number resolving detectors", IEEE Trans. Appl. Supercond. **15**, 2 (2005).

[50] F. Mattioli, Z. Zhou, A. Gaggero, R. Gaudio, R. Leoni, A. Fiore, "Photon-counting and analog operation of a 24-pixel photon number resolving detector based on superconducting nanowires", Optics Express **24**, 8 (2016).

CHAPTER 2

DEVICE OPERATION AND MODELING

2.1 Introduction

The chapter explains about the operation of SNSPD devices. The electrical model of the device was simulated using microwave simulation software and using S-parameters of the amplifier. The transient response and S-parameters were studied using different circuits and the difference in response was analyzed. The effect on output was simulated with change in the values of frequency, load resistance and biasing resistance.

2.2 Principle of operation

The superconducting nanowire single photon detector utilizes superconducting property of the material. One can describe a superconducting wire by means of a complex order parameter $\psi(x) = |\psi(x)| \exp^{i\phi(x)}$, where Φ is the phase of the quantum mechanical wave function and $|\psi|^2 = n_s$ is the density of the superconducting charge carriers. The Bardeen-Cooper-Schrieffer (BCS) theory explains the microscopic phenomenon behind the photo-response of the SNSPD [1]. In the ground state, two electrons join together to form Cooper pair. The length over which electrons form the Cooper pair is called coherence length,

$$\xi = (2 \hbar v_f)/ (\pi \Delta), \quad (2.1)$$

where $\hbar$ is the Planck constant, v_f is the Fermi velocity, and Δ is the superconducting energy gap. The superconducting energy gap for conventional superconductors at zero temperature can be expressed in terms of its transition temperature (Tc) as

$$\Delta(0) = 1.6 k_B Tc. \quad (2.2)$$

When a photon with energy greater than band gap energy is absorbed, it creates quasiparticles by breaking Cooper pair. These excited quasiparticles interact with other electrons and phonons and recombine to form a Cooper pair. The phonon thus generated promotes further pair breaking. The processes, generation of quasiparticles and recombination to Copper pairs continue until the phonons reach to substrate and get absorbed as shown in Fig.2.1 [2].

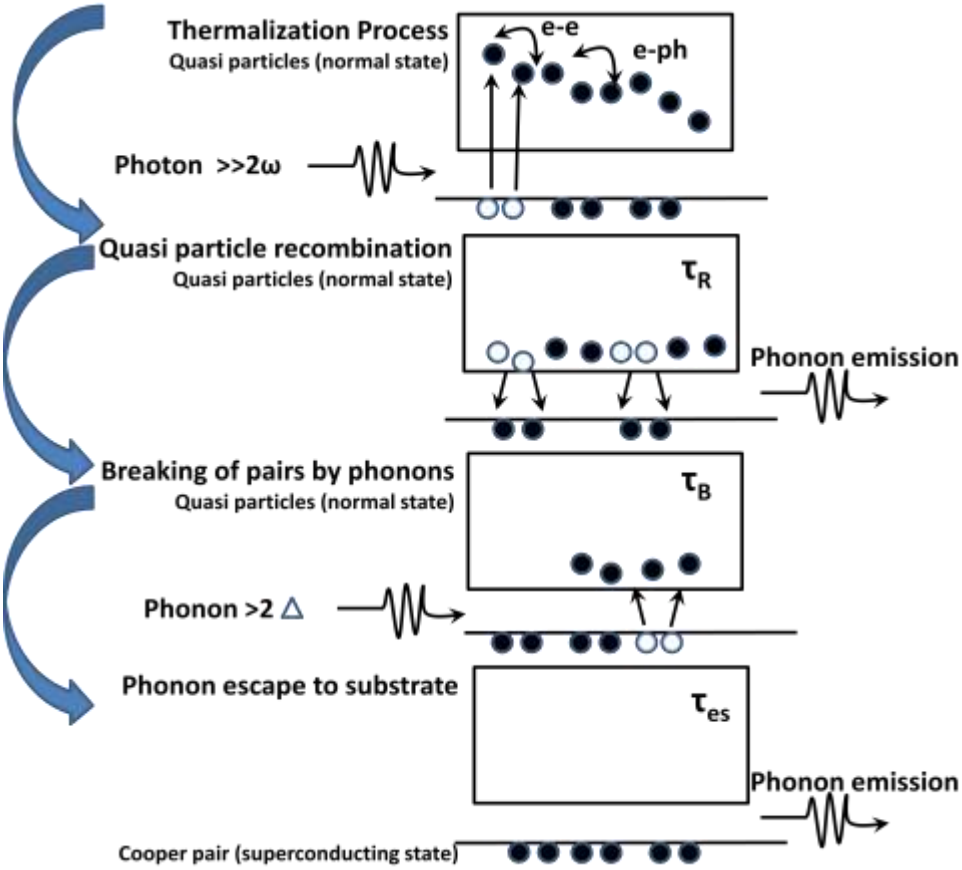

Fig.2.1: Photo-response processes on absorption of a single photon (a) thermalization process (b) quasiparticle recombination results in phonon emission. (c) breaking of pairs by phonons. (d) final escape of phonon to substrate. (Box represents the energy level above the energy gap and line represents the ground state) [2].

2.3 Detection mechanism - The hotspot model

A photon absorbed by the superconducting film generates many quasiparticles as explained before which create a region of suppressed / destroyed superconductivity called hotspot. When the rate of quasiparticles multiplication is more than the rate of

their out diffusion their temperature rises and goes beyond their critical temperature [3]. The volume of hotspot expands due to diffusion of quasiparticles. The quasiparticle concentration along with the stripe width varies with time and with distance from the spot of photon absorption. The thermalization length L_{th} is the length of hotspot span from the point of photon absorption and it is equal to the square root of multiplication of the diffusivity (D) and thermalization time (τ) of quasiparticles. Since the thickness of the film $d<<L_{th}$, the hotspot spans in whole thickness area uniformly [4, 5]. The volume of hotspot has been reported to be proportional to the energy of the absorbed photon [6]. As shown in Fig.2.2, schematically, the hotspot forces the biasing current to flow sideways. The local current density around the hotspot when exceeds the critical value giving rise to the formation of resistive barrier along the width of the nanowire. The resistive region expands along the axis of the nanowire until the current flow is completely blocked and the bias current starts flowing through the external circuit until the hotspot cools down and nanowire goes back to the superconducting state.

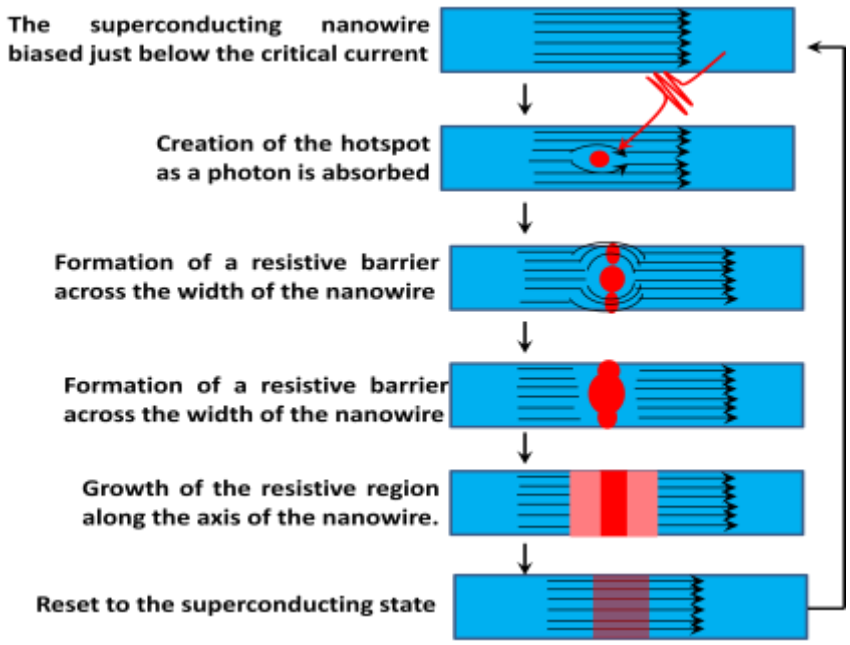

Fig.2.2: Hotspot model showing the loop of transition from superconducting state to normal state and back to superconducting state after absorption of a single photon by current biased (I_B) nanowire.

2.3.1 Limitation of hotspot model

The hotspot model does not explain the nature of increasing tendency of quantum efficiency with decreasing temperature and at the same time, nor does it explain the origin and increase in dark count rate with increasing bias current. The hotspot model describes the step like behavior of device detection efficiency (η_{DDE}) with increasing I_B/Ic value, however experimental results differ from that and shows exponential increase in η_{DDE} with increasing I_B/Ic till it reaches a threshold value. Beyond the threshold η_{DDE} becomes constant. Similarly, hotspot model does not explain the wavelength dependence of η_{DDE}. Unlike the step like behavior as explained by hotspot model η_{DDE} remains constant until it reaches a threshold wavelength value, beyond the threshold η_{DDE} decreases exponentially with increasing wavelength.

Further, hotspot model limits the detection of photon above cut off wavelength. All these contradictions and limits of the hotspot model can be explained in terms of thermal unbinding of the vortex and anti-vortex pair.

2.4 Fluctuation in 2D superconductors: vortex and antivortex pairs

Superconducting nanowires used in SNSPD can be treated as two dimensional. The resistance does not necessarily reach zero below the Tc in 2D superconducting materials due to thermal fluctuation caused by the existence of vortex and antivortex pairs (VAPs). According to the framework of the Berezinskii-Kosterlitz-Thouless (BKT) model, there is a temperature T_{BKT} (< Tc) below which the resistance of the 2D superconductor becomes zero due to formation of vortex antovortex pair [7]. The binding energy of VAPs weakens in the presence of transport current and finally the thermal fluctuation break the VAP. The binding energy is strongly reduced if the separation between the vortex and anti vortex (r) is more than $2\lambda^2/ d$ and becomes proportional to $(1/r^2)$. In 2D superconductors however, the binding energy becomes proportional to the log of separation (r) as the width is less than $w<<2\lambda^2/ d$ [8].

2.5 Kinetic inductance in superconducting nanowires

Kinetic inductance is intrinsically associated with superconducting nanowires. It plays an important role in electro-thermal response and timing jitter of SNSPDs. The value of the kinetic inductance also determines the rise and fall times of the photo-induced signal in the SNSPDs and hence the count rate [9, 10]. The SNSPD device can be represented with kinetic inductance in series with parallel combination of resistance (R_{HS}) and a switch as shown in Fig.2.3.

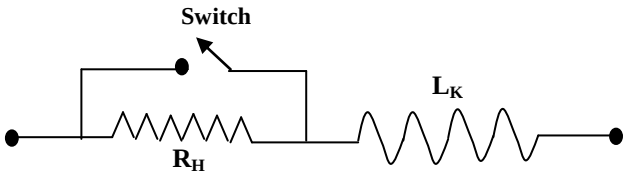

Fig.2.3: Phenomenological model of SNSPD.

The switch remains closed as long as there is no photon absorption. Once a photon is absorbed and forms hotspot the switch becomes open. Once the switch is open, the current flows through the load impedance Z_O (~50Ω). This gives rise to voltage transient with rise time τ_{rise}, where

$$\tau_{rise} = L_K / (R_{HS}+Z_O). \quad (2.3)$$

The moment current flows through the load impedance; SNSPD cools down and regains superconductivity. The fall time (τ_{fall}) of the voltage pulse follows

$$\tau_{fall} = L_K/Z_O. \quad (2.4)$$

2.6 Count rate and reset

The count rate of a SNSPD is dependent on its reset time [11] and the value of the kinetic inductance limits the reset time. For instance, the kinetic inductance of a meander structure in a (10µm x 10µm) area with 100nm width and 50% fill factor is about 500nH and the fall time (τ_{fall}) is about 10ns. The maximum count rate is estimated to be 0.1 GHz. The count rate can be increased by decreasing the reset time

which is possible by decreasing the value of L_K [12-15] and increasing the value of Z_O. The kinetic inductance (L_K) of the nanowire can be reduced either by reducing its length or by choosing superconducting material with lower intrinsic inductivity [6]. However, lowering the length will also reduce the effective area of the device. The other way to reduce reset time is by putting a series resistance between device and the contact pads. The drawback in reduction of reset time in this way is that the device gets latched in finite voltage mode and requires to be heated above the superconducting transition temperature to resume the counting event [16].

2.7 Simulation of readout circuit

The electrical model of the device can be simulated using any microwave simulation software. High frequency electromagnetic simulation software (SONNET) is used to solve the S-parameters of gold (Au) pads as well as NbN superconducting material (Fig.2.4). The S11 (reflection) and S21 (transmission) parameters for NbN nanowires (100nm width and 10nm thin) on Si/SiO_2(300nm) substrate in the shape of meander structure in an area of 10µm x 10µm as a function of frequency is plotted in Fig.2.5. It can be seen that S11 is in the range of (0.9 to 0.8) and phase difference increases with frequency whereas S21 is in the range of 0.1 to 0.04 while shown the increasing trend as the frequency increases. These values can be used in ADS software while modeling the electrical circuit to study the output w.r.t. time and frequency.

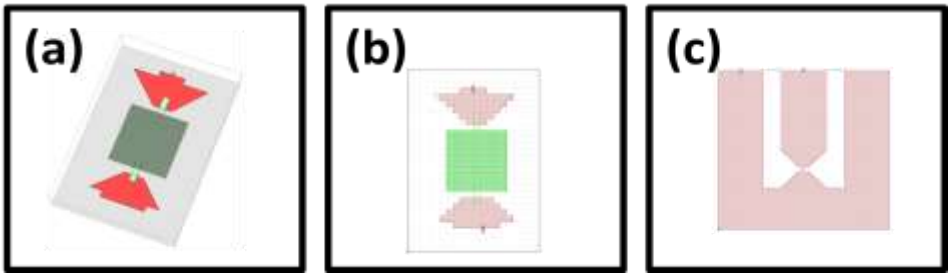

Fig.2.4: NbN meander structure along with Au contact pads using SONNET software (a) Zoomed 3D view (b) Zoomed 2D view (c) Full 2D view.

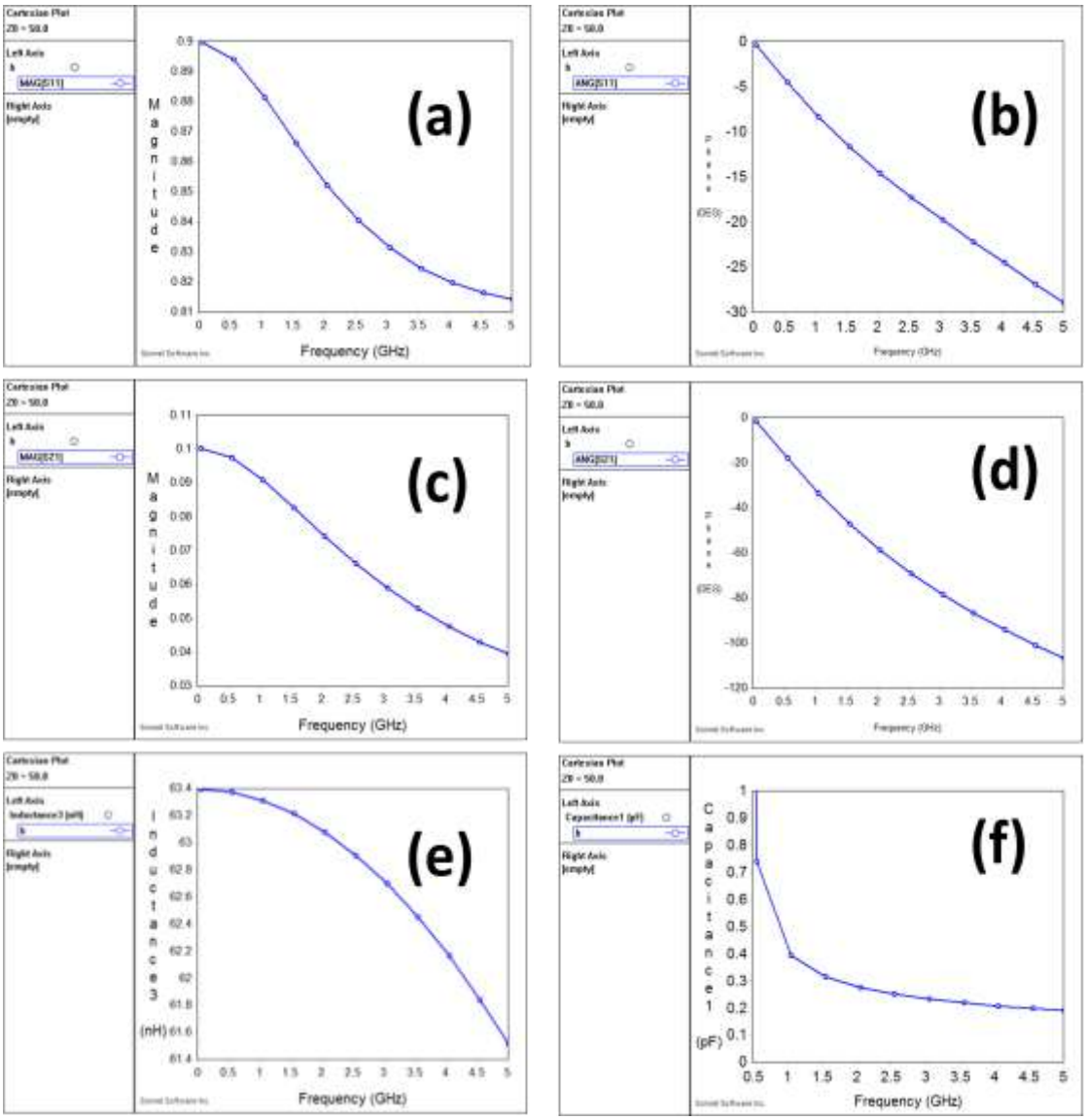

Fig.2.5: Graph for NbN meander structure using SONNET software (a) S11(magnitude) vs frequency (b) S11(phase) vs frequency (c) S21(magnitude) vs frequency (d) S21(phase) vs frequency (e) inductance vs frequency (f) capacitance vs frequency.

S-parameters for gold pads (magnitude and angle) and its equivalent capacitance are shown in Fig.2.6. Since the gold pads are designed in coplanar waveguide shape with all the dimensions taken for impedance matching, the S21 is quite high in comparison to S11.

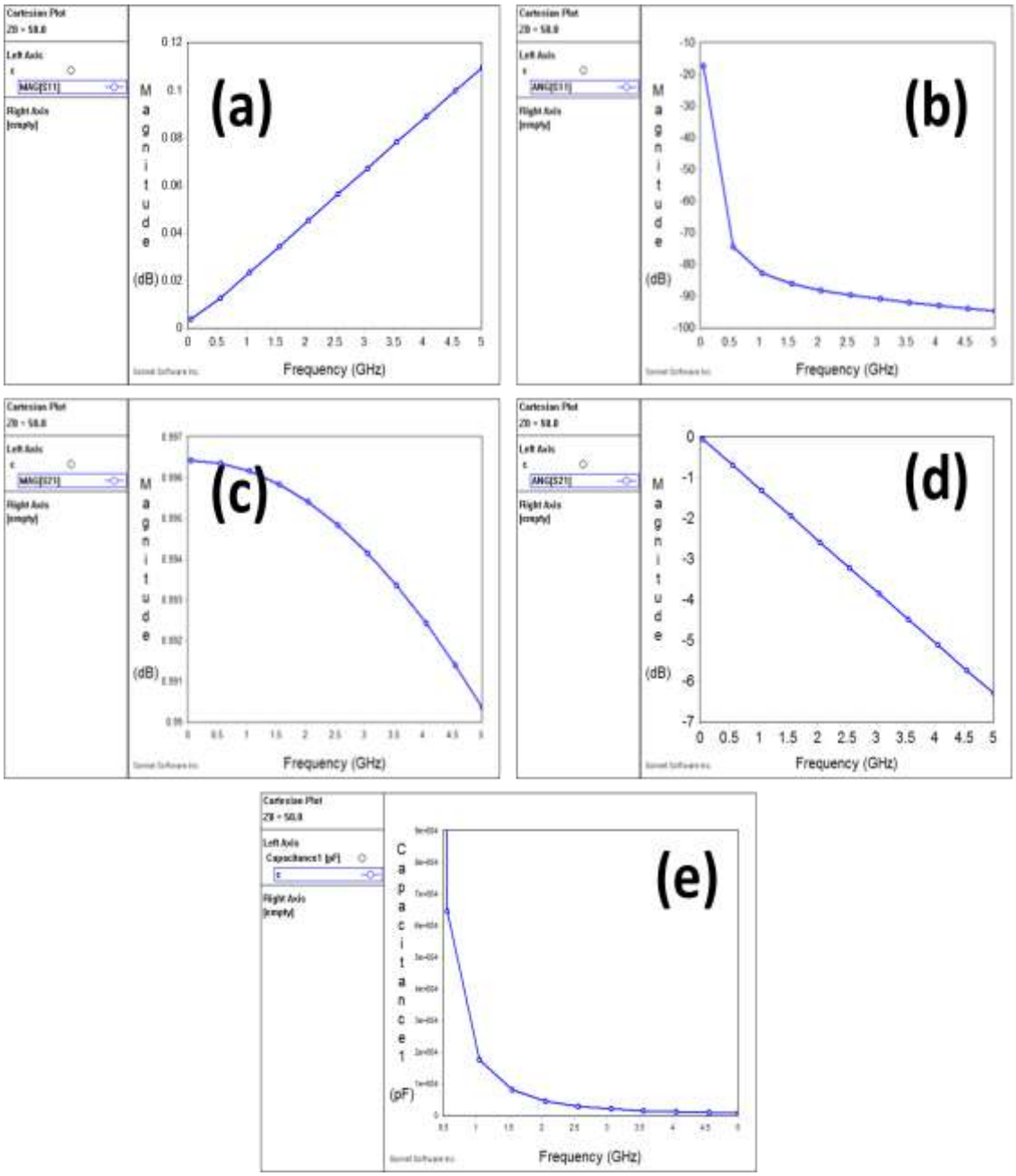

Fig.2.6: Graph for Au contact pads using SONNET software (a) S11(magnitude) vs frequency (b) S11(phase) vs frequency (c) S21(magnitude) vs frequency (d) S21(phase) vs frequency (e) capacitance vs frequency for contact pads.

2.7.1 DC coupled electrical readout

Case study – I

The detector is connected to a dc bias source and readout which consists of transmission line, band pass filter and amplifier with 50Ω input impedance as shown

in Fig.2.7. The values of equivalent capacitance and inductance generated by SONNET software for NbN meander and gold pad are used in Agilent Advanced Design System (ADS) ADS for modeling of SNSPD along with readout components. The transient response and S-parameters have been studied and analyzed using different circuits.

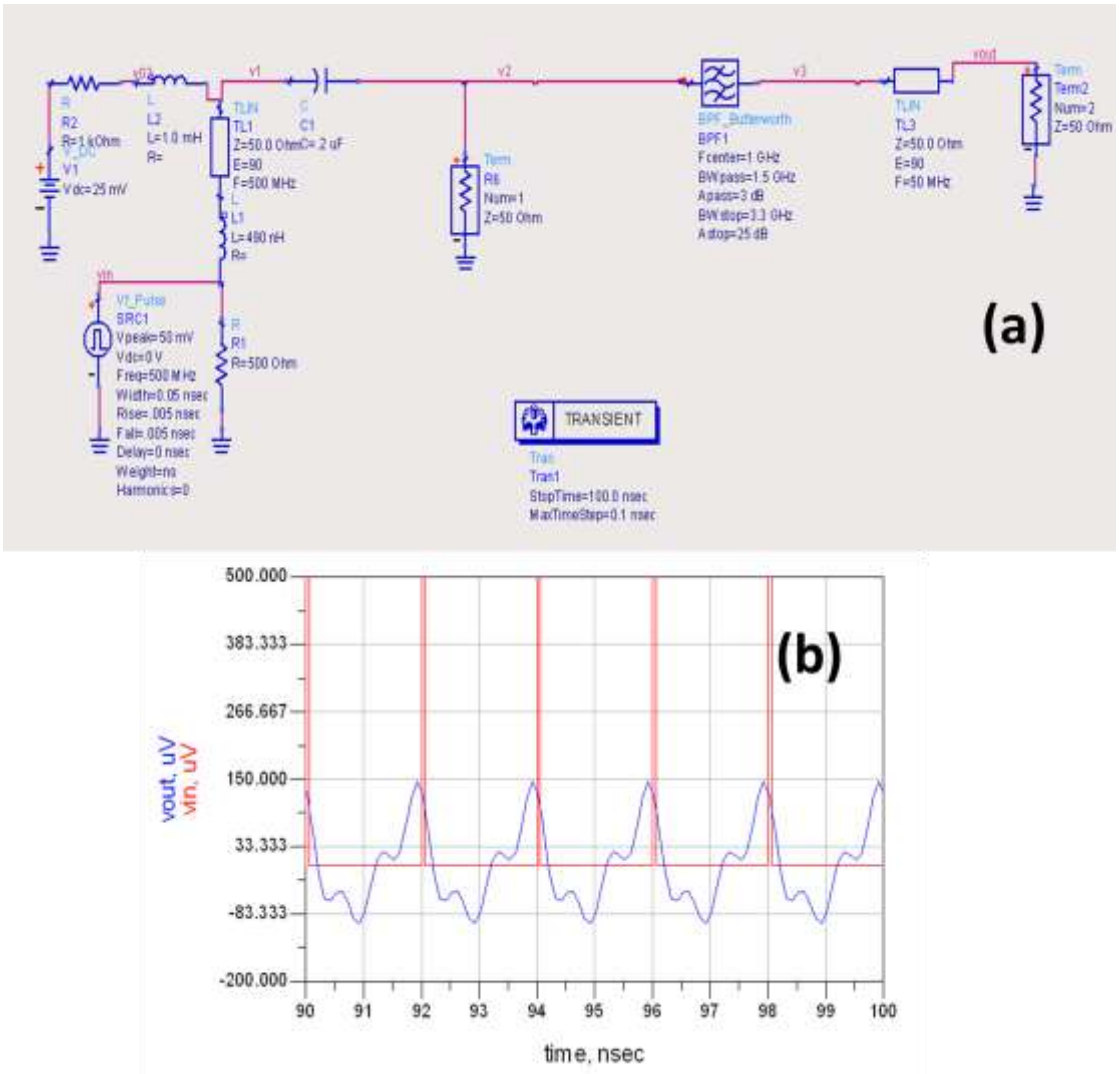

Fig.2.7: (a) Readout circuit (b) Input and output voltage vs frequency.

Case study - II

A normal coax Tee is replaced by using a bias Tee and the response is studied. Next the Band pass filter (BPF) is replaced by HEMT and the difference in response (Fig.2.8) is noticed at 50mV pulse generated across the SNSPD at 500MHz. The details of the Bias Tee and HEMT are as follows.

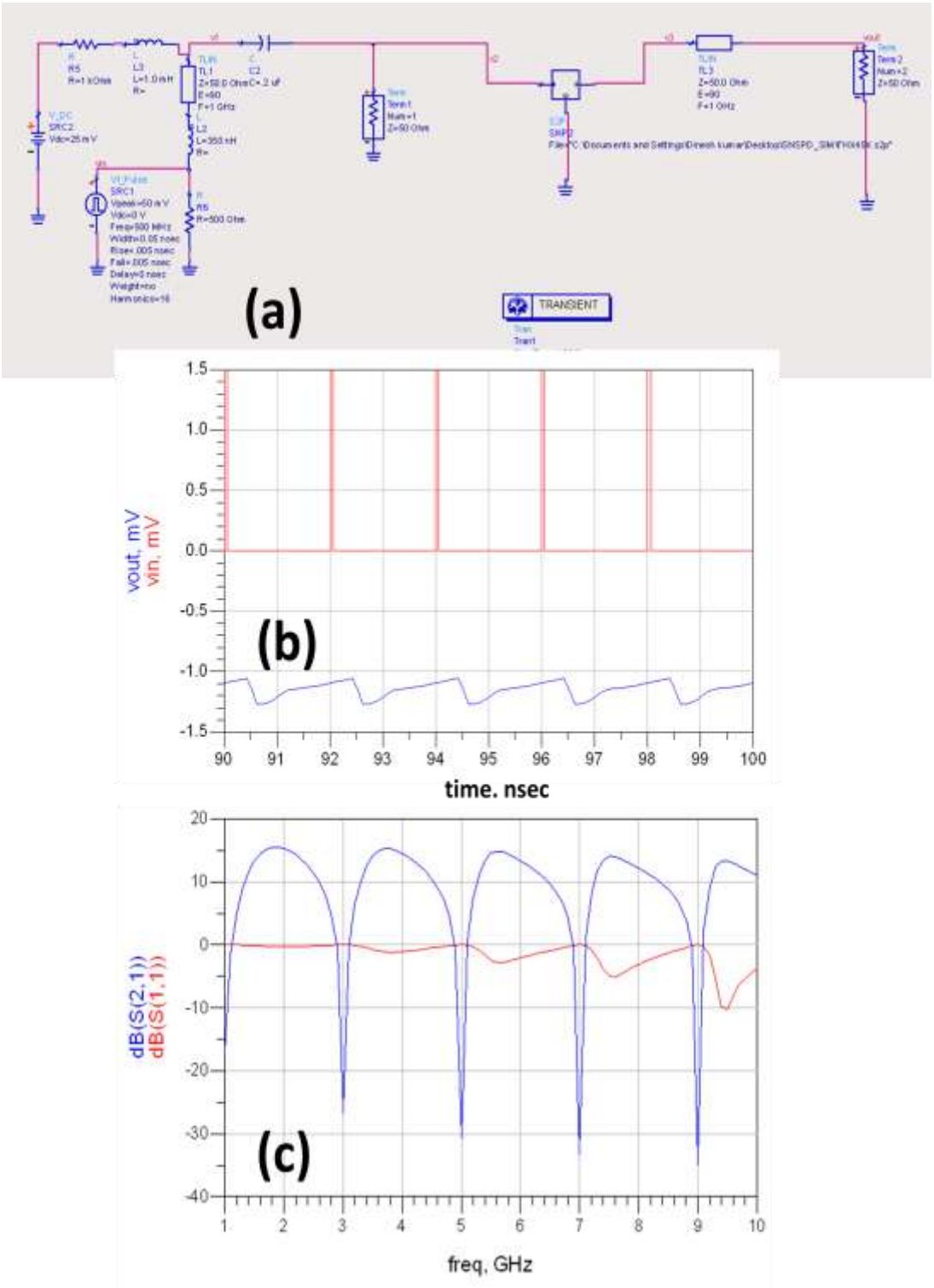

Fig.2.8: (a) Readout circuit (b) Input and output voltage vs frequency (c) S11 and S21 vs frequency.

Specifications of bias Tee:

Make - Mini circuit, Model - ZX85-12G-S+**.**

50Ω, wide band (0.2MHz - 12GHz), 0.6dB insertion loss, 30dBm RF power, 1.8Ω DC resistance from DC to RF&DC port and DC current up to 400mA and voltage standing wave ratio (VSWR) of 1.2.

Specifications of high electron mobility transistor (HEMT):

Make - Sumitomo Electric Device, Model - FHX45X

Ultra-low noise and high gain amplifiers in the 2 to 18GHz frequency range, low noise figure: 0.55dB at 12GHz, high associated gain: 12dB at 12GHz

Case study - III

The effect of cascading two amplifiers can be seen in the response of the simulated model of the circuit as shown in Fig.2.9. Apart from this the voltage from the DC voltage source passes through the low pass filter (LPF) to diminish electronic noise. One LPF is kept at room temperature while the other one is placed inside the cryostat. The same way, output of the SNSPD gets amplified from an amplifier kept at cryogenic temperature. The second amplifier is placed outside of the cryostat.

Case study - IV

Simulated inductance and capacitance of the Au coplanar waveguide along with that of meander structure are shown in Fig.2.10. The first negative peak is the response caused by the pulse generated across the SNSPD (formation of the resistive domain due to absorption of the photon). The amplitude of the output pulse depends on the bias current and positive pulses afterwards are due to charge storage in the capacitor of the low pass filter which slowly dies out. However, reflection in AC signal occurs due to partial mismatch of impedance in coaxial cable and input impedance (50Ω) of the amplifier

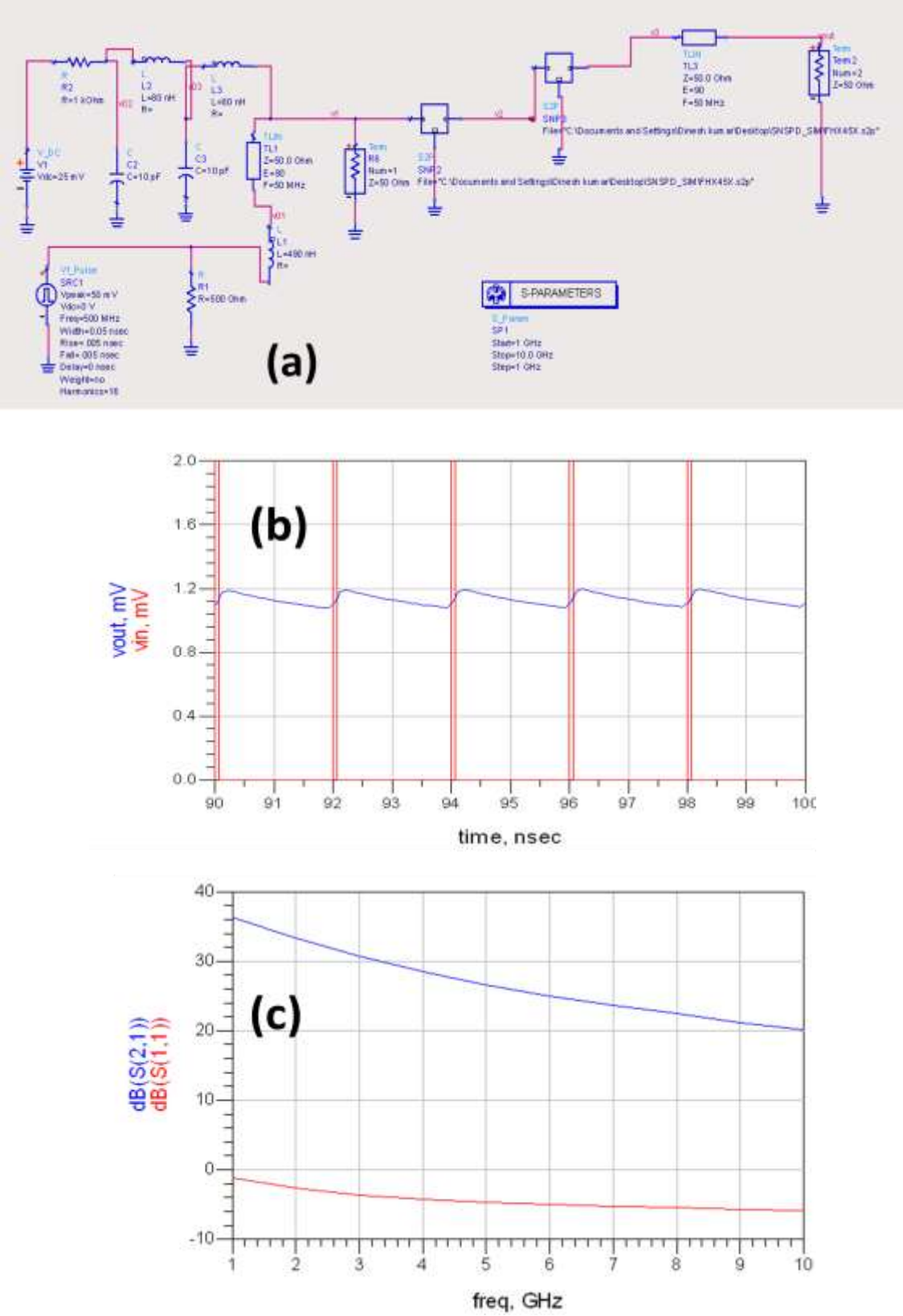

Fig.2.9: (a) Readout circuit (b) Input and output voltage vs frequency (c) S11 and S21 vs frequency.

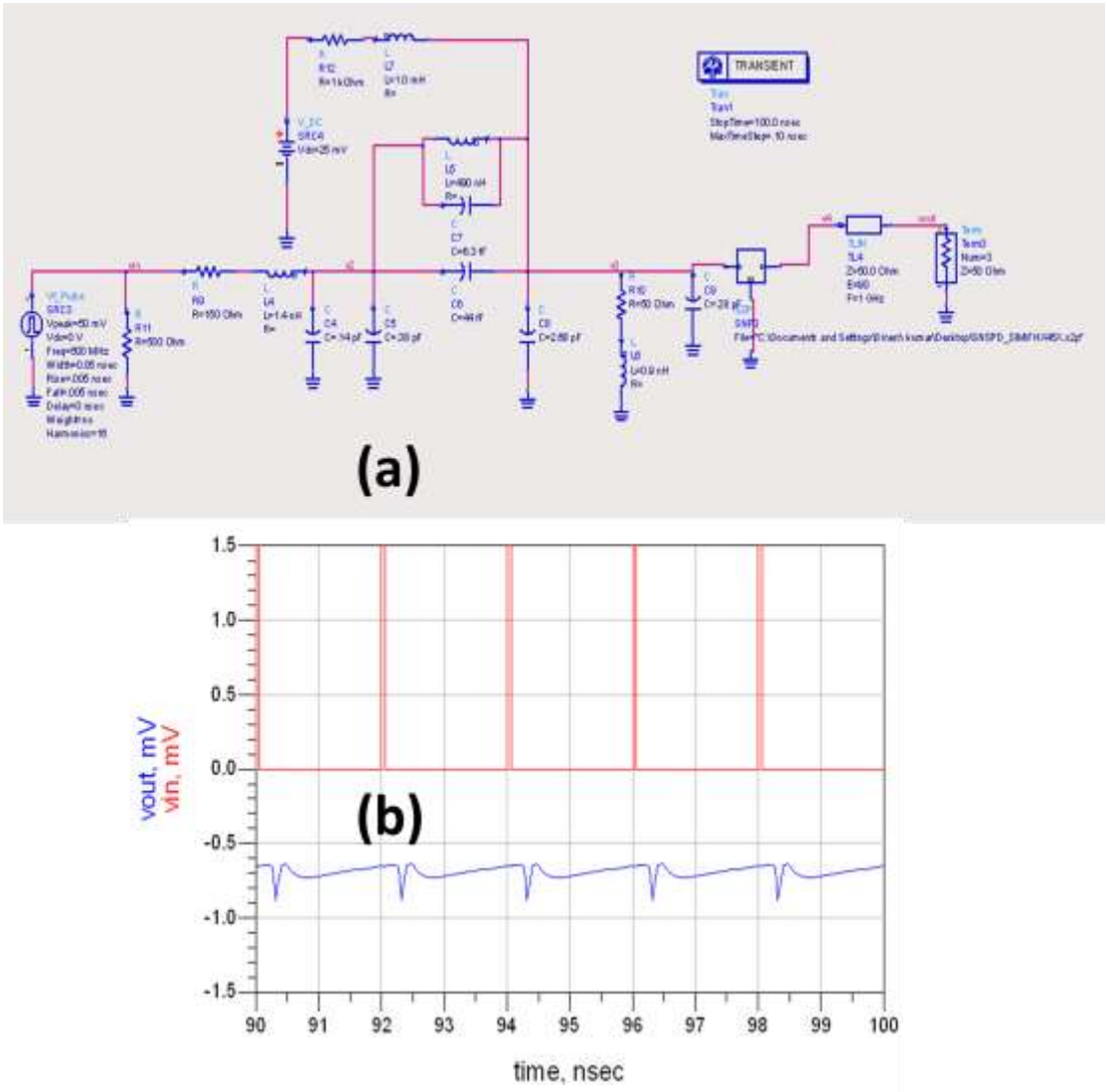

Fig.2.10: (a) Readout circuit (b) Input and output voltage vs frequency.

Case study – V

A -3dB attenuator is placed before the second amplifier to damp the reflection and prevent the formation of standing waves between two amplifiers (Fig.2.11). Second stage amplifier is AC coupled with pre amplifier to remove non-linear effects. The isolation provided by pre amplifier from the 50Ω impedance of the subsequent amplifier gives chance to independently adjusting the load seen by the SNSPD by changing R_L [17]. In order to mitigate the effect of slowly decaying oscillations and maintain high SNR and maximum bandwidth, L-R high pass filter is added at the input of the amplifier. This filter creates a path to the ground for DC and the

frequencies below its -3 dB cut off frequency. The chosen cut off frequency couple the oscillations to the ground and not to the input of the amplifier.

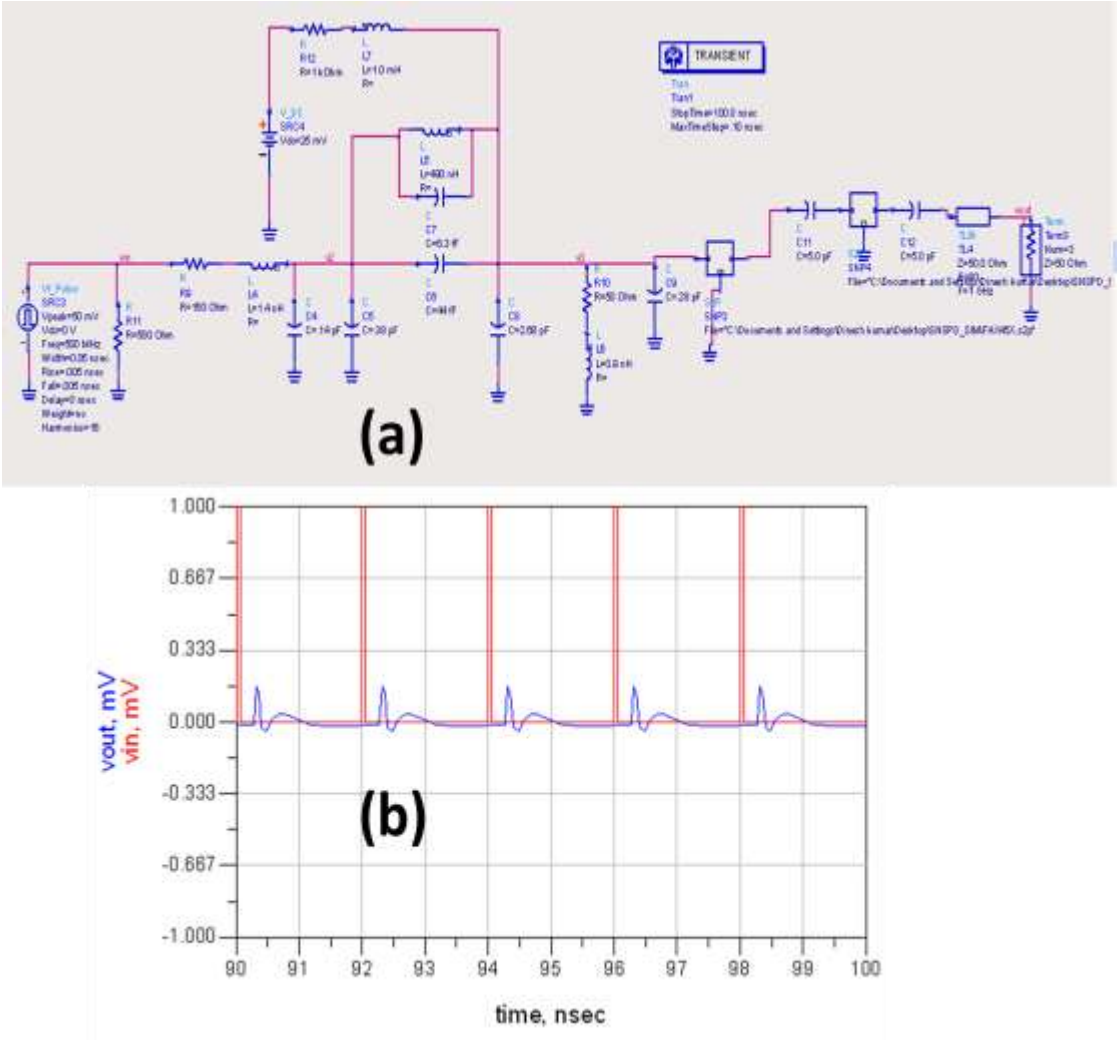

Fig.2.11: (a) Readout circuit (b) Input and output voltage vs frequency.

2.7.2 Dependence of output on frequency, load resistance, and biasing resistance

The output of SNSPD is damped oscillation and its electrical equivalent circuit can be represented by RLC model. Fig.2.12 shows that reset time can be decreased (τ_R) and pulse amplitude can be increased by increasing the R_L. The maximum limit of R_L is the value at which the device starts latching.

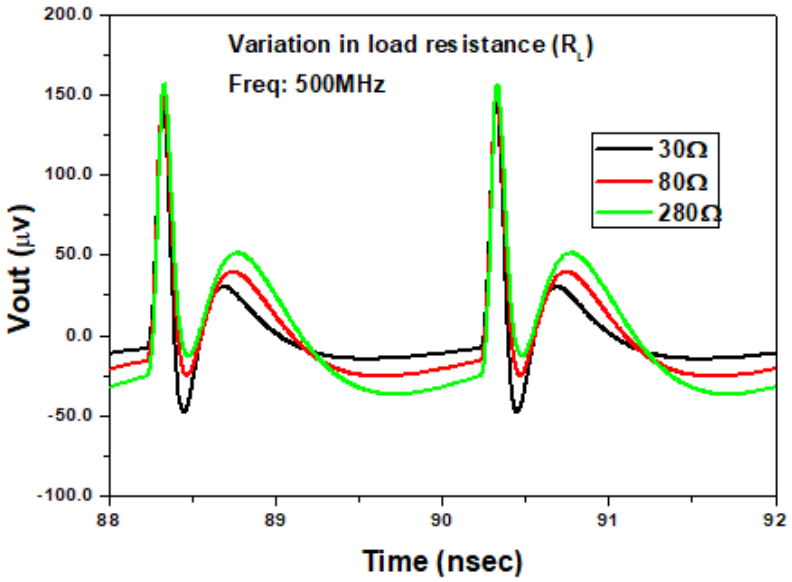

Fig.2.12: Output voltage of readout circuit at different load resistance.

The effect of biasing resistor (R_B) on output voltage is seen in the Fig.2.13. The output voltage remains unchanged. The increase in biasing resistance therefore decreases the bias current. The high value of R_B helps in making the bias network work as constant current source and the bias voltage is selected accordingly. In other way the decrease in R_B value increases the current and hence the R_B can be decreased up to a minimum value to keep the device in superconducting state. However once the photon is detected by SNSPD, R_B does not affect the output response from the readout.

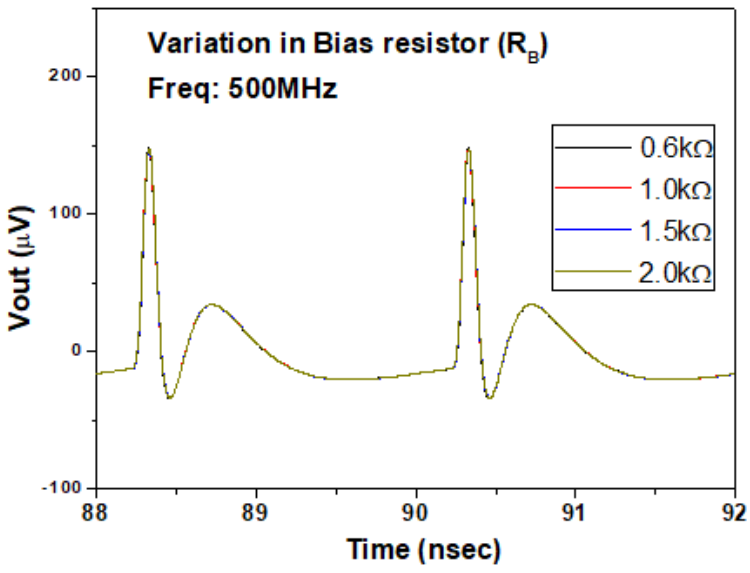

Fig.2.13: Output voltage of readout circuit at different Bias resistance.

Variation in output with change in frequency is shown in Fig.2.14. Since the application in the field of quantum communication requires fast data transfer at high bit rate, the circuit is tested for a range of frequencies from MHz to GHz range. The output is found to be absolutely fine and detectable in the whole frequency range.

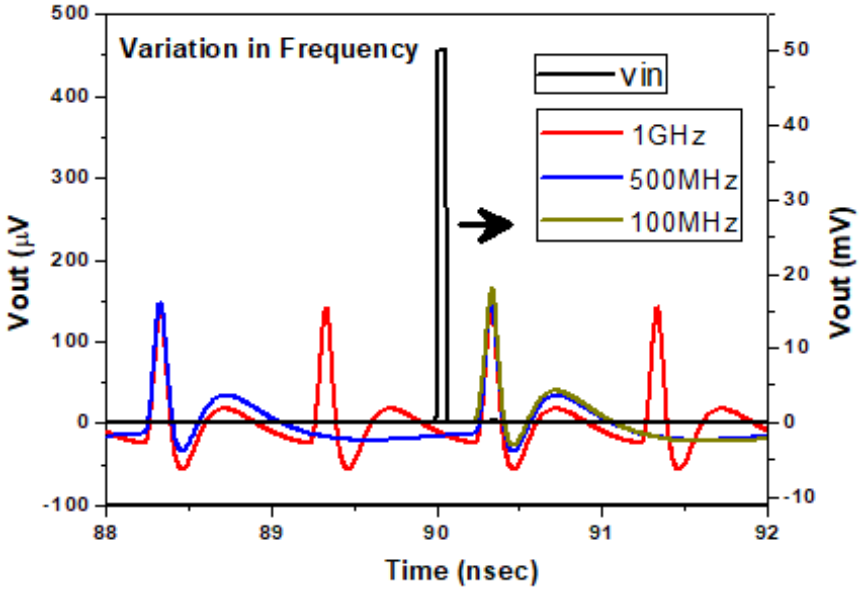

Fig.2.14: Output voltage of readout circuit at different frequencies.

2.8 Summary

This chapter gives a brief overview on principle of SNSPD operation. It discusses about hotspot model and its limitation. Fluctuation in 2D superconductors due to vortex and anti-vortex pair formation has been introduced. Apart from this sophisticated readout electronics required for monitoring signal corresponding to each and every photon has been discussed. Simulation of readout circuits which assist identifying electronic components has been carried out.

2.9 References

[1] J. Bardeen, L.N. Cooper, J.R. Schrieffer, "Theory of superconductivity", Phys.Rev. **108**, 1175 (1957).

[2] N. Bluzer, "Temporal relaxation of photoinduced nonequilibrium in niobium", Phys. Rev. B **46**, 1033 (1992).

[3] M. Bell, a. Sergeev, V. Mitin, J. Bird, a. Verevkin, and G. Gol'tsman, "One-dimensional resistive states in quasi-two-dimensional superconductors: Experiment and theory", Phys. Rev. B **76**, 094521 (2007).

[4] A. D. Semonov, G. Gol'tsman, A. Korneev, "Quantum detection by current carrying superconducting film", Physica C **351**, 349 (2000).

[5] A. M. Kadin, M. W. Johnson, "Nonequilibrium photon-induced hotspot: A new mechanism for photodetection in ultrathin metallic films", Appl. Phys. Lett. **69**, 3938 (1996).

[6] A. Korneev, P. Kouminov, V. Matvienko, G. Chulkova, K. Smirnov, B. Voronov, G.N. Gol'tsman, M. Currie, W. Lo, K. Wilsher, J. Zhang, W. Slysz, A. Pearlman, A. Verevkin, R. Sobolewski, "Sensitivity and gigahertz counting performance of NbN superconducting single-photon detectors", Applied Physics Letters **84**, 5338 (2004).

[7] J. E. Mooij, "Percolation, Localization, and Superconductivity", edited by A. M. Goldman and S. A. Wolf (Plenum, New York, 1984), p. 325.

[8] B. I. Halperin and D. R. Nelson, "Resistive transition in superconducting films", J. Low Temp. Phys. **36**, 599 (1979).

[9] J. Zhang, W. Słysz, A. Pearlman, A. Verevkin, Roman Sobolewski, O. Okunev, G. Chulkova, and G. N. Gol'tsman, "Time delay of resistive-state formation in superconducting stripes excited by single optical photons", Phys. Rev. B **67**, 132508 (2003).

[10] R. Sobolewski, J. Zhang, W. Slysz, A. Pearlman, A. Verevkin, A. Lipatov, O. Okunev, G. Chulkova, A. Korneev, K. Smirnov, P. Kouminov, B. Voronov, N. Kaurova, V. Drakinsky, G. Goltsman, "Ultrafast superconducting single-photon optical detectors", Proc. SPIE 5123, Advanced Optical Devices, Technologies, and Medical Applications, 585 (2003).

[11] M. Tarkhov, J. Claudon, J. Ph. Poizat, A. Korneev, A. Divochiy, O. Minaeva, V. Seleznev, N. Kaurova, B. Voronov, A. V. Semenov, and G. Gol'tsman, "Ultrafast reset time of superconducting single photon detectors",Appl. Phys. Lett, **92**, 241112 (2008).

[12] S. Miki, M. Takeda, M. Fujiwara, M. Sasaki, A. Otomo, and Z. Wang, "Superconducting NbTiN nanowire single photon detectors with low kinetic inductance", Appl. Phys. Express **2**, 075002 (2009).

[13] A. J. Annunziata, D. F. Santavicca, J. D. Chudow, L. Frunzio, M. J. Rooks, A. Frydman, and D. E. Prober, "Niobium superconducting nanowire single-photon detectors", IEEE Trans. on Appl. Supercond., **19**, 327 (2009).

[14] M. Ejrnaes, A. Casaburi, R. Cristiano, O. Quaranta, S. Marchetti, S. Pagano, "Maximum count rate of large area superconducting single photon detectors", J. Mod. Optics, **56**, 390(2009).

[15] Y. Korneeva, I. Florya, A. Semenov, A. Korneev, and G. Goltsman, "New generation of nanowire NbN superconducting single-photon detector for mid-infrared", IEEE Trans. Appl. Supercond. **21**, 323 (2011).

[16] A. J. Kerman, J. K. W. Yang, R. J. Molnar, E. A. Dauler, and K. K. Berggren, "Electrothermal feedback in superconducting nanowire single-photon detectors", Phys. Rev. B **79**, 100509(R) (2009).

[17] A. J. Kerman, D. Rosenberg, R. J. Molnar, and E. A. Dauler, "Readout of superconducting nanowire single-photon detectors at high count rates", J. Appl. Phys. **113**, 144511 (2013).

CHAPTER 3

FACILITY CREATION FOR LOW TEMPERATURE MEASUREMENTS

3.1 Introduction

Superconducting nanowire based detectors have shown lot of potential in recent years as single photon detector at the telecom wavelength for its application in the area of quantum optical technologies due to its better performance matrices [1-19]. It is found that the detection efficiency of SNSPDs increases and the dark count diminishes significantly with the decrease in operating temperature. Motivated by the earlier work of Orgiazzi et al. [20], on experimental setup down to 4.2K which was based on standard liquid helium transport dewar, we designed and built a liquid helium flow cryostat down to 1.8K along with probes for electrical as well as optical characterizations. Economical consumption of liquid helium, sound temperature stability, and efficient optical coupling, easy and user friendly samples changing option without breaking the vacuum, or warming up the cryostat were some of the important requirements taken into considerations while designing the cryostat.

3.2 Cryogenic equipment and measurement systems

3.2.1 Cryostat

High efficiency variable temperature liquid nitrogen shielded liquid helium cryostat with cryogen level monitor and level probes is custom designed for its use in characterization of superconducting nanowire single photon detector (SNSPD). Since the performance of SNSPD improves with lowering of operating temperature, the operating temperature range of the cryostat is kept 1.8K to 325K and it has sample in vapor (dynamic exchange gas) configuration. The interface flange of cryostat along with two sample probes have matching NW100 flange for top loading samples which can be quickly changed while operating.

The cryostat has four chambers namely vacuum chamber, liquid nitrogen reservoir, liquid helium reservoir and sample tube space. Sample vapor pumping port with NW25 interface flange, sample safety pressure relief and compound pressure gauge are included for regulating and monitoring the pressure in sample tube space (10PSI maximum operating pressure). 2 stage rotary vane vacuum pumping station, compound vacuum gauge, oil mist exhaust filter and pumping line assembly with isolation vacuum valve, stainless steel flexible bellow are used to pump the sample space.

Evacuation valve with safety pressure relief and provision for pressure gauge for vacuum chamber is installed and connected to turbo pump. The outer vessel called vacuum chamber provides thermal insulation from environment while evacuated. Liquid nitrogen reservoir assembled with nitrogen fill/vent ports cools radiation shields surrounding the sample space inside the tail of the cryostat to 77K to reduce the amount of heat reaching the 4K stage.

The liquid helium reservoir is assembled with helium fill and access port with wilson fitting, helium flow control valve and safety pressure relief valve. It also has the provision for helium recovery. Liquid helium flows from the reservoir through the adjustable flow valve located at the bottom of the sample tube. On applying heat, it vaporizes the liquid and raises the gas temperature. This gas then enters the sample space and cools the sample space to the desired temperature down to 1.8K upon pumping. De-icing heaters are installed on capillary/flow valve to prevent blocking of helium flow due to icing.

Dual channel liquid cryogen level monitor with top loading removable liquid helium, liquid nitrogen level probe and two sensor readouts enable in-situ monitoring of cryogen inside the reservoirs.

The 14.5” OD cryostat with 22.0” main dewar body length has ~10 liters capacity outer liquid nitrogen reservoir which provides full nitrogen shielding around liquid helium reservoir and sample tube**.** Liquid helium reservoir with ~10 liters capacity and ~ 100ml/hr helium loss rate with all inserts at 4.2K enables users to continue experiment without refilling the system for two to three days.

Sample tube with 3" outer dia. and 8" long tail section has one 50Ω cartridge heater. One calibrated (1.4K to 325K) cernox sensor installed at the heat exchanger are for precise controlling and monitoring of temperature at heat exchanger.

Hermetic electrical 10-pin vacuum feedthrough mounted on the top surface of the cryostat provides access to connect the heater and sensor of the heat exchanger to a temperature controller.

The temperature of the heat exchanger is controlled by the dual action of regulating the helium flow and the electrical power to the heater in contact with the heat exchanger. The temperature-controlled liquid/gas then flows up an annular channel surrounding the central sample tube, which contains low-pressure helium exchange gas to cool the sample. The coolant exits at the top of the cryostat and passes to a gas flow pump and controller combination. An extra temperature sensor is fitted at the sample position to monitor the temperature at the sample position. A complete picture of the cryostat is shown in Fig.3.1. Fig.3.2 shows the electrical connections for different sensors and heaters.

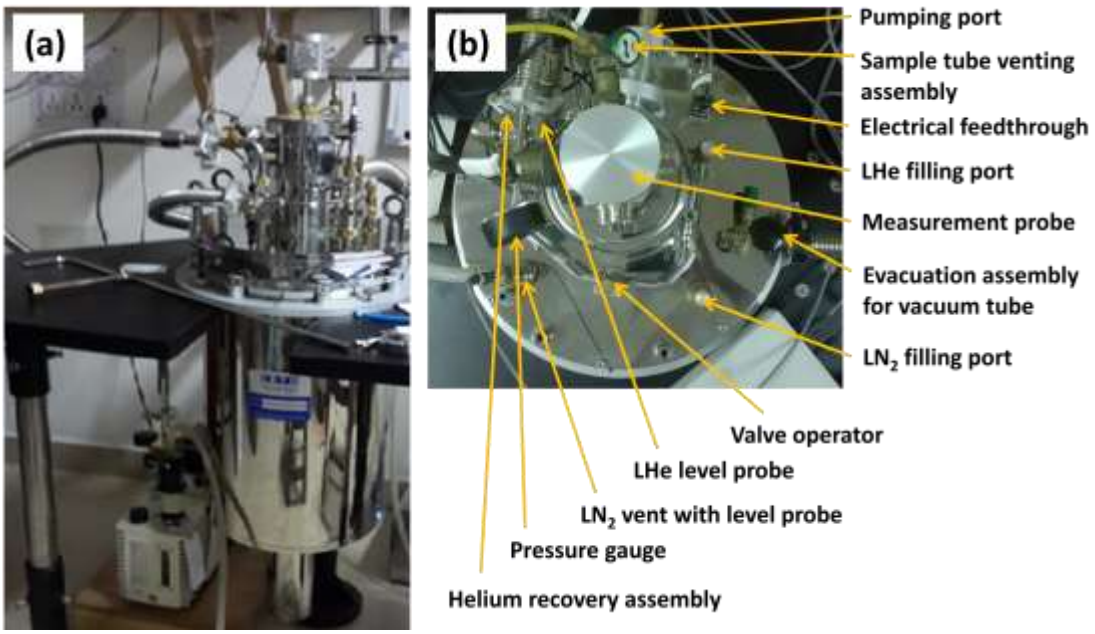

Fig.3.1: (a) Picture of complete cryostat system. (b) Top view of the system. Major parts of the system are marked with arrows.

3.2.2 Dipper probe

Two dipper probes, one for transport property measurement and another for optical property measurement are designed.

The electrical probe is designed to study transport properties such as critical temperature (Tc), critical current (Ic) for the optimization of properties in superconducting thin films and nanostructures.

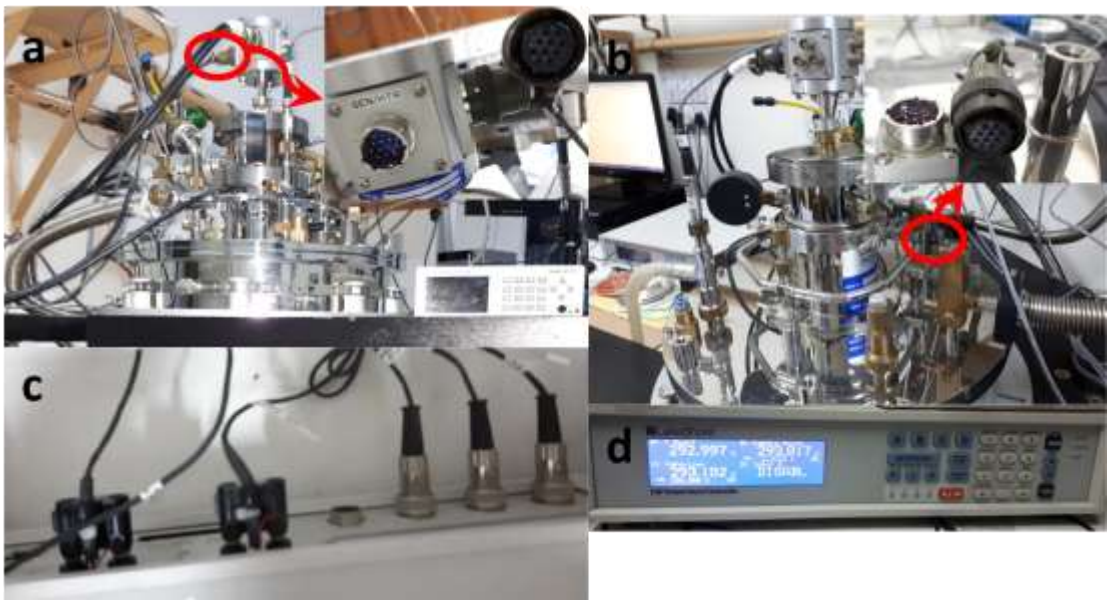

Fig.3.2: 10 pin feed through for connection with temperature sensor and heater from (a) sample space and T-mount in probe (inset zoomed view) as well as (b) vaporizer and its connection with temperature controller (inset zoomed view) (c) back view showing three sensor connection (sample space, T-mount, vaporizer) and two heater connection respectively from right (d) front view showing temperature at sample space, T-mount, vaporizer and fourth sensor is not connected.

3.2.2.1 Custom sample probe for low temperature electrical measurements

Top loading sample probe assembly with a sliding seal for sample positioning and height adjustment with NW100 interface flange is designed. 10-pin feedthrough is connected to DC Manganin leads which run down the probe and are properly twisted in pairs and filtered with RF chokes with high impedance to minimize noise propagating down to the device enclosure. These wires are connected with thermal sensors and heaters at the lower end. Manganin wires are used to minimize the heat transfer due to poor thermal conductivity. 26-pin electrical connector with mate for 10

twisted pairs of 36 gauge phosphor bronze are connected to LCC socket at sample zone. Fair electrical conductivity and low thermal conductivity of phosphor bronze allows electrical connections to devices at low temperatures without adding excessive heat. Further, non-magnetic phosphor bronze has a relatively low temperature dependence of its resistance from room temperature to helium temperatures. In addition, hermetically sealed 6 nos. BNC feedthroughs are connected with coaxial cables for AC transport measurement.

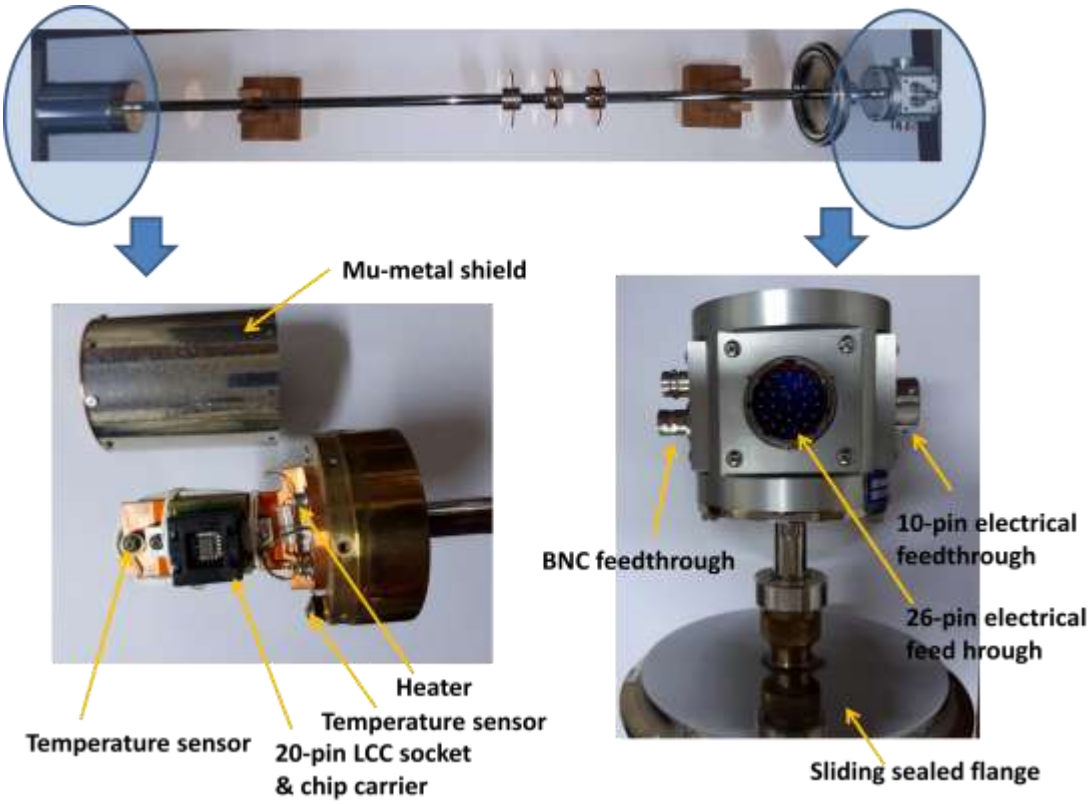

Fig.3.3: Top panel shows the variable temperature insert for electrical characterization. Lower left panel while describes the major components of the low temperature module right lower panel marks the different feedthroughs for electrical connections.

Mu-metal shield is attached to copper sample mount to cover entire sample assembly. Mu-metal is a nickel–iron soft magnetic alloy with very high permeability, which is used for shielding sensitive electronic equipments against static or low-frequency magnetic fields. Mu-metal's advantage over other high-permeability alloys is that it is more ductile and workable, allowing it to be easily formed into the thin sheets needed for magnetic shields. 50Ω heater and calibrated (1.4K-325K) sensor are installed on

sample mount. Custom T-style sample holder with 20-pin LCC socket and matching chip carrier is mounted on brass sample mount. The sample rod is made from stainless steel because of its high mechanical strength, and excellent thermal insulation. Variable temperature insert with all its parts and feedthroughs can be seen in Fig.3.3.

3.2.2.2 Custom sample probe for low temperature optical measurements

The variable temperature insert for single photon detection application along with its major components and feedthroughs can be seen in Fig.3.4.

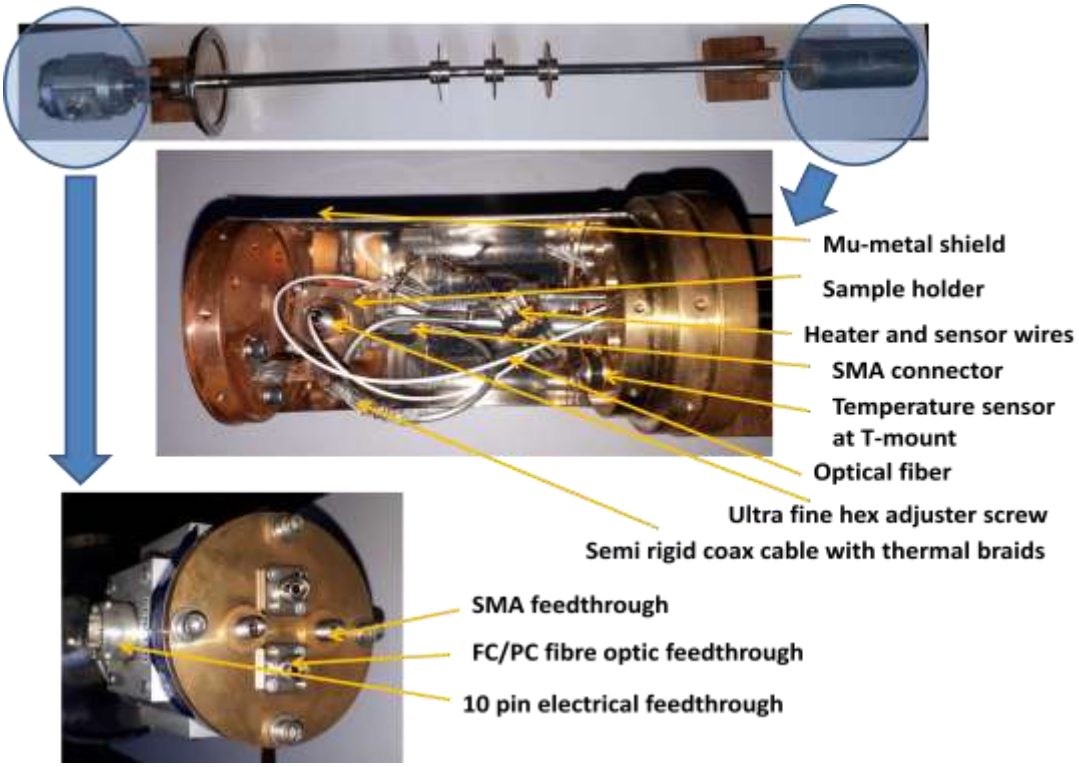

Fig.3.4: Variable temperature insert for single photon detection application shown in the top panel. The bottom panel shows the enlarged view of the top of the insert having feedthroughs for electrical as well as optical connections. The center panel describes in details the essential components of the optical insert.

It is a top loading sample probe assembly with sliding seal to adjust the height for sample processing. It has nickel plated copper tube with brass end cap and Mu-metal shield installed inside nickel plated copper tube to cover entire sample assembly at lower end of the probe. Probe dimensions are compatible with cryostat. One 50Ω heater is installed on sample mount. One out of two calibrated (1.4K-325K) sensors is installed on sample mount and another one on INVAR sample holder near sample space. There is

one 10-pin feedthrough with mate connected to sensor and heater using manganin wires and has same purpose as in the case of electrical probe. It has two hermetic SMA female to female coaxial connectors. One connector is connected with ultra miniature coaxial cable (0-20GHz) and another one with semi rigid coaxial cable rated for use 0-20GHz. These cables have male SMA connectors at both ends and the other end of these cables is terminated in sample area (inside Mu-metal shield).

The probe has the provision of shining light onto the sample area. Single mode fibre (SMF-28e or equivalent) at one end connected to hermetic FC/PC fibre optic feedthrough and the other end of fibre is fixed on sample holder for illumination of the sample.

The measurement setup has the provision of connecting two sample holders with separate set of FC/PC connector with single mode fibre to shine light on the sample and SMA connector with coaxial cables for RF output. The optical characterization of two devices can be performed using the setup and at the same time which is useful for HBT / Time correlated single photon counting (TCSPC) studies.

3.2.3 Sample holder

Custom sample holder consists of main body, cover and device mounting plate made of INVAR 36. The sample holder along with its components is shown in Fig.3.5.

Main body and device mounting plate are gold electroplated. Dimension of sample holder is 20mm x 20mm x 11mm. The cover plate is 3mm thick while the main body height is 8mm. SMF28e single mode optical fibre terminated by 5.5mm long x1.8mm diameter anti reflection coated ferrule and grin lens assembly is attached with the cover plate. The lenses include an 8° angled facet to minimize back reflection and compensate for the angular beam deviation from angled fibre ferrules. The ferrule is held in a modified ultra-fine hex adjuster screw with 100 threads per with 1.8mm diameter central hole for housing the optical fibre. The ferrule holding the optical fibre is placed inside the hole and permanently fixed with low temperature compatible STYCAST epoxy. Locking ring arrangement at top of screw allows adjusting and fixing the distance between optical fibre tip and sample surface.

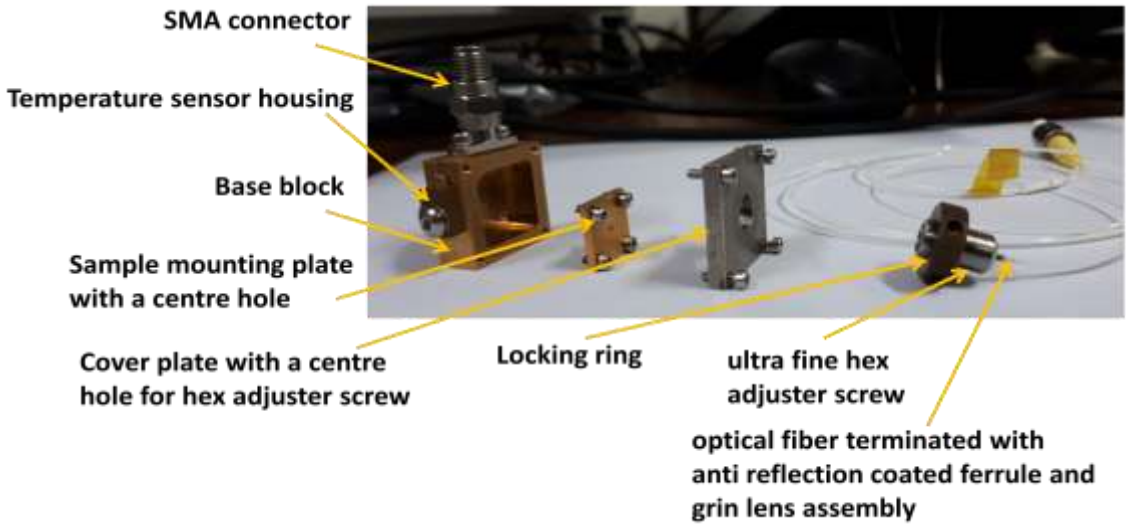

Fig.3.5: Picture of all essential components for customized sample holder placed in sequence for easy to understand the sample mounting steps.

An observation hole of 0.08mm diameter is bored at centre of the body and also at centre of device mounting INVAR 36 plate (12mm x 12mm x 1.5mm). The device mounting plate can be tightly fixed at the bottom of the main body with four non magnetic stainless steel screws. An SMA male connector is mounted at one side of the main body of sample holder. The centre pin of SMA connector is surrounded by insulating sleeve to isolate it from the main body of the sample holder. Calibrated cernox sensor mounted on the back of the sample mounting block monitors the sample temperature in a precise manner.

3.2.4 Arrangement for sample mounting to enhance optical coupling

The sensor wires installed to the sample holder are demountable and are terminated in mini-disconnects. Fig.3.6 shows the microscope and sample holder assembly. The short wave infrared camera with InGaAs sensor and having spectral band from 0.9µm to 1.7µm is connected with microscopic zoom lens compatible with C mount microscopic zoom lens (12:1 or higher) to achieve ~3-4 micron resolution. Illumination source for in situ monitoring of alignment with the help of fibre optic ring light/ fibre optic coaxial illuminators is integrated with the camera. The sample mounting arrangement is quite user friendly under a microscope.

This process involves (1) fixing the sample on sample mounting plate inside the main body with an idea that when the top lid is placed the tip of the fibre should nearly comes on the top of the active area (10µm x 10µm) of the sample; (2) loosely placing the top lid on to the holder; (3) placing the whole assembly under the microscope; (4) turning on the laser so that the fibre tip illuminates the sample. Once illuminated, through the backside hole of the holder one can see which part of the sample is coming under the fibre tip; (5) adjustment of the top lid to ensure that the active area is illuminated; (6) tightening the screws to firmly fix the top lead on to the main body.

Fig.3.6: (a) Microscope assembly (b) Sample holder assembly.

3.2.5 System operation

3.2.5.1 Evacuating the outer space and sample space of cryostat

The outer space of the cryostat is evacuated using turbo molecular pump to reach the base pressure of the order of E-6 mbar. It is found that the cryostat retains the vacuum for at least couple of weeks.

One roughing pump is permanently attached to the sample space of the cryostat. It allows venting the sample space as and when requires. The roughing pump line attached to the sample tube while maintains the vacuum level in the sample space also pumps out helium gas to reach the temperature of the sample space below 4.2K.

3.2.5.2 Flushing of liquid helium chamber to check flow conductance

It is important to check the flow conductance through the inside capillary in dry condition at room temperature prior to cooling down the cryostat. For that liquid helium chamber is filled with helium gas whereas the sample space is kept in vacuum.

The helium throttle valve while open partially by turning the flow valve operator counter-clockwise, the pressure gauge clearly indicates flow of gas into the sample tube. If the chamber is connected with the vacuum pump the pump exhaust or sound indicates that the capillary is not plugged or restricted.

3.2.5.3 Cooling down

The liquid nitrogen chamber requires thorough flushing with nitrogen gas before filling it with liquid nitrogen to minimize moisture content in the LN_2 reservoir. In a similar way, the helium reservoir is required to be flushed out several times with helium gas filled with high purity helium gas to avoid any condensation during cooling. The outer LN_2 reservoir is then filled with liquid nitrogen and the system is left overnight in such condition.. Maintaining a certain vacuum level in the sample tube during cooling is must to reduce potential water condensation. Ideally the sample tube should be continuously pumped out. Pre-cooling the system wil LN_2 substantially reduces the consumption of liquid helium. Prior to filling the liquid helium reservoir with liquid helium, it is important to maintain the liquid LN_2 in reservoir.

3.2.5.4 Pressure regulation

The helium reservoir safety relief pressure regulator maintains positive pressure. This helps in maintaining proper flow of liquid helium from the reservoir into the heat exchanger and sample tube. Moreover, the regulator prevents condensation and air from entering the reservoir while protecting against over pressure. All other helium ports require to be plugged immediately after the completion of the liquid helium transfer.

3.2.5.5 Helium recovery

Helium recovery line next to the cryostat is installed for recovery of expansive helium gas as shown in Fig.3.7. The outlet of the helium reservoir and the exhaust port (with oil mist filter) of the sample tube vacuum pump are connected to the helium recovery line to ensure that the evaporated helium is recovered.

Fig.3.7: Connection of bellow with (a) helium reservoir at one end and with (b) helium recovery line at another end.

3.2.5.6 Mounting the probe in cryostat

The mounting of sample on probe was performed in two situations one is initial mounting before cooling down of sample space and another one is when the sample space is sitting at low temperature. The main advantage of this cryostat is that no warming of sample space is required prior to sample change.

In the first case, at the time of mounting the sample probe continuous flow of helium gas in the sample space needs to be maintained. Sample space is purged afterwards with enough helium gas two to three times before the final evacuation. This prevents sample space from moisture absorption and reduces moisture content from the sample probe.

In the second case, while unmounting the sample probe from the cryostat enough flow of helium gas is required to be maintained. Sample place needs to be immediately closed with blank flange and evacuated. Prior to remounting of probe the sample space needs to be filled again with helium gas. Insertion of the probe in the cryostat is required to be done under the constant flow of helium gas in the sample space to avoid any condensation due to absorption of moisture.

3.2.5.7 Variable temperature operation

The evacuation of sample space is started with rotary pump. After half an hour waiting, the throttle valve that controls the flow of liquid helium to the sample space through capillary is opened by about one complete turn. The sample space begins to cool down at in about four to five hours of time the temperature of sample holder (T_{sample}), heat exchanger ($T_{vaporizer}$), and sample mount assembly (T_{mount}) reached ~1.8K. The throttle valve is then kept open by about half a turn to maintain the system at minimum temperature.

There are two ways to operate the system below 4.2K - (a) sample in vapour and (b) sample in liquid.

In 'sample in vapour mode', the flow control valve is opened partially while pumping the sample tube continuously. The flow requirement can be adjusted precisely in order to reach the lowest desired temperature. The temperature of the sample zone can be fixed at any value to approximately 20K by heat input to the heat exchanger alone. In 'sample in liquid' mode, initially heat exchanger power is set to zero and the flow control valve is opened largely by two-three complete turns till the sample tube is filled with liquid helium to a some extent. In the next step the flow valve is required to be closed complete and the sample tube to be attached to vacuum pump for evacuation. The system reaches to the lowest possible temperature and holds until the liquid helium inside the sample tube is all exhausted.

3.2.5.8 Sample contact and connections

The sample is wire bonded with the connections on the chip carrier. Sample for the low temperature transport measurements can be positioned on 20-pin chip carrier using silicone-free cryogenic Apiezon N grease. The chip carrier can be easily placed inside the chip carrier socket. The arrangement for mounting the chip carrier inside the socket is very much user friendly. The twenty contacts from the sample holder as shown in Fig.3.8 are connected with the 20-pin connector using separate manganin wires. Hermetically sealed 20-pin connector is the link between instruments sitting at room temperature and sample at low temperature inside the cryostat.

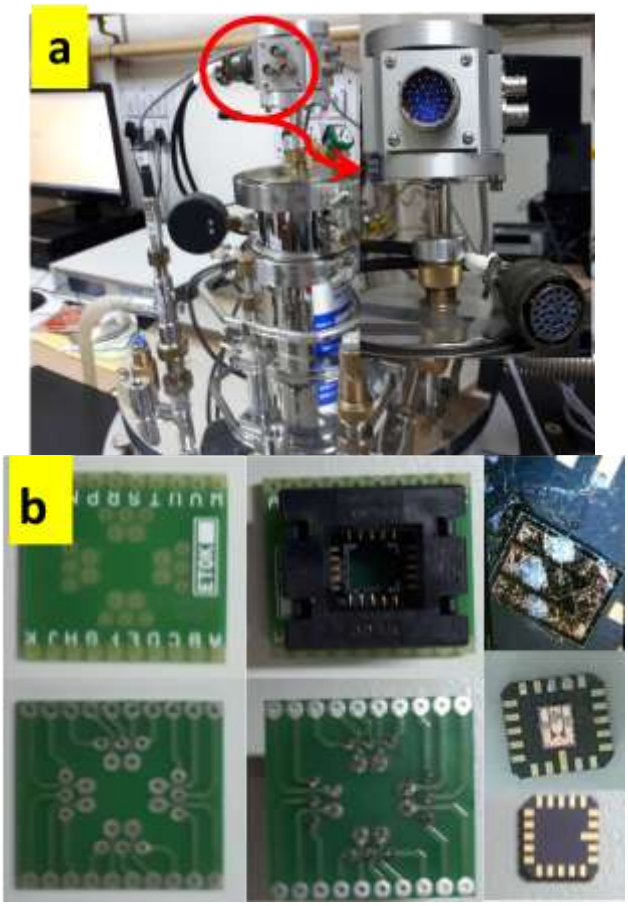

Fig.3.8: (a) 20 pin feed through and its connection with cable having 20 twisted manganin wires; six BNC connectors for connecting coaxial cable. Either of the connectors can be used for outside connection with instruments using cables for IV, RT measurements. Either two cables with 10 wires each or six coaxial cables for other side (inside cryostat) connection with the (b) PCB (front and back view vertically) on which sample holder (front and back view vertically) is mounted. Chip carrier with sample mounted on it (Zoomed picture of sample and its wire bonding with pins of chip carrier can be seen) can be put inside the sample holder.

3.2.6 System performance

3.2.6.1 Temperature stability

For monitoring and controlling the temperature of heat exchanger, and sample space heater and sensor are connected to the Lakeshore 336 auto tune temperature controller. 50Ω heater with 50W max heater power is used for the heaters installed on vaporizer and T-mount. Three out of four available sensor inputs are used to read the sensors installed on sample mount, T mount and vaporizer.

Fig.3.9 shows the temperature stability at sample mount for both the inserts. They were cooled down and after stabilization of temperature using the adjustable flow valve variation of temperature was monitored with time. The maximum temperature drift of ~4mK from average value has been observed for electrical insert, whereas optical insert shows maximum drift of ~7mK over a time span of about one and half hour. It is important to mention that during these measurements neither the sample mount heater nor the heater mounted at the heat exchanger was used to stabilize the probe temperature.

Fig.3.10 shows the temperature dependence of resistance change in superconducting NbN thin films carried out in four-point-probe measurement geometry. Measurements in both heating and cooling cycle were performed at a sweeping rate of 0.5K/min. The data clearly shows superconducting transition (Tc) at 14.6K with 0.5K transition width (ΔT). The measurement clearly shows there is negligible thermal hysteresis associated with heating and cooling cycles.

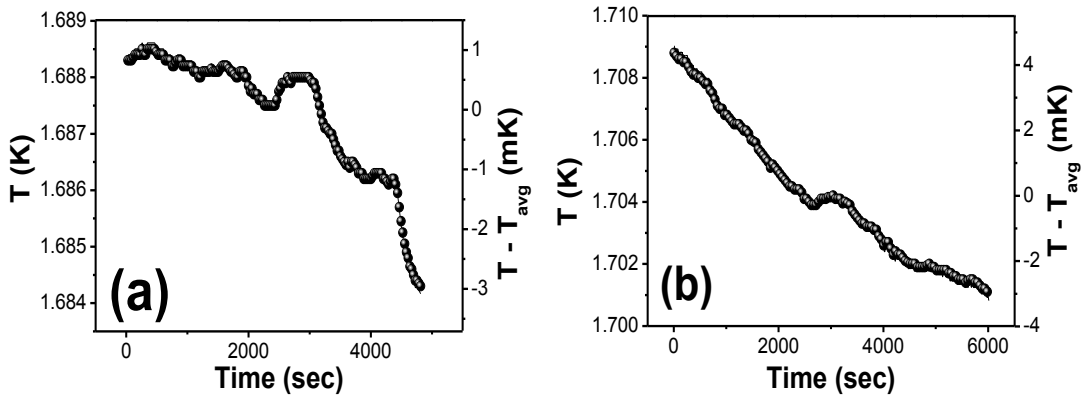

Fig.3.9: Observation of temperature stability. Plot (a) shows the experimental data of temperature drift for electrical insert. Similar measurements were carried out for optical insert and plotted in panel (b).

3.2.6.2 Current versus voltage (IV) measurements

The voltage across the device remains zero in its superconducting state and current flows without any dissipation. This can be maintained only if the operating temperature of the device is less than the critical temperature and also the current flowing through the device at this temperature

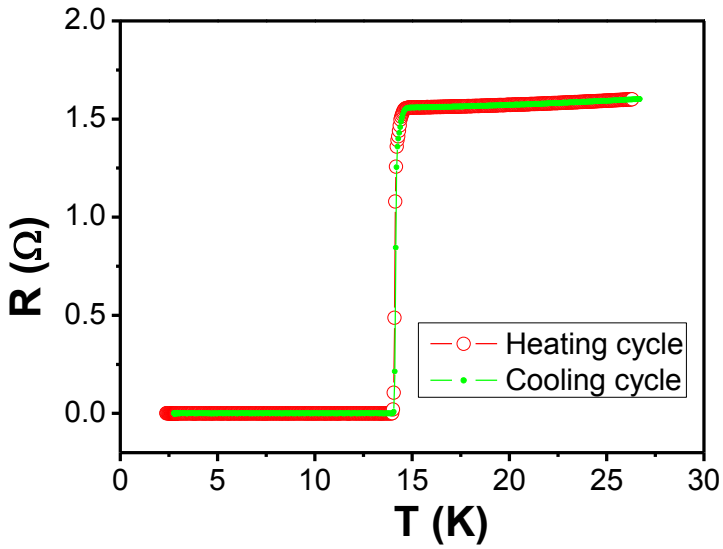

Fig.3.10: Resistance versus temperature plots of superconducting NbN films. Heating cycle was followed immediately after the completion of cooling cycle. As can be seen cooling and heating profiles are perfectly superimposed.

is less than the critical current (Ic). The IV measurements of a used device from MIPT Moscow have been performed to check the system performance and shown in Fig.3.11. A resistance (R_P) is connected in parallel of device which helps the device to come back to the superconducting state and therefore prevents from latching. The IV plot shows that the critical current (Ic) of the device is ±5μA.

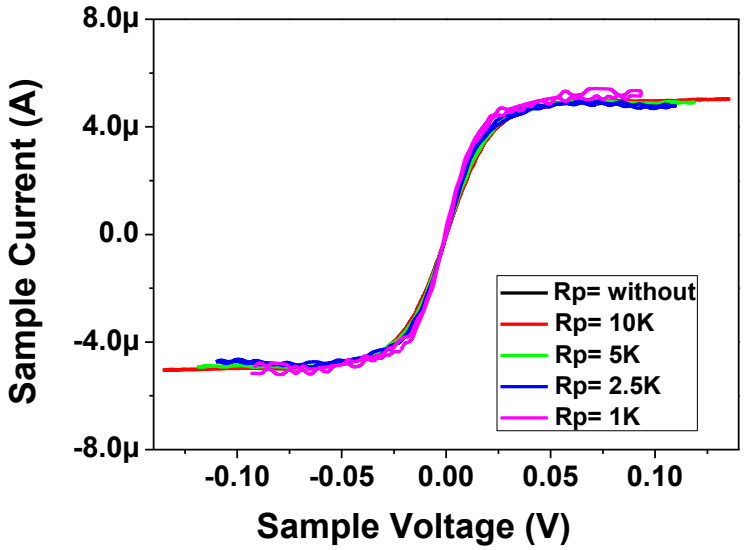

Fig.3.11: IV measurements on a SNSPD device.

3.3 Setup for optical measurement

3.3.1 Overall plan

The setup in the Fig.3.12 shows measurement protocols of single photon devices. The function generator triggers the pulsed laser diode and oscilloscope simultaneously. The output pulse from laser can then be attenuated to a desired level using a series of variable attenuators. Beam splitter after the polarizer guides a fraction of laser beam to the power meter while the remaining part goes to the device inside low temperature cryostat though single mode optical fibre. The device is current biased using a source meter nit (SM) in series with a ~100kΩ resistance just below the Ic. The voltage output from the device due to absorption of single photon is amplified and monitored either by high bandwidth (GHz) oscilloscope or by a photon counter. However, integration of overall setup requires though characterizations of individual components. A brief discussion towards that direction has been discussed in the following sections.

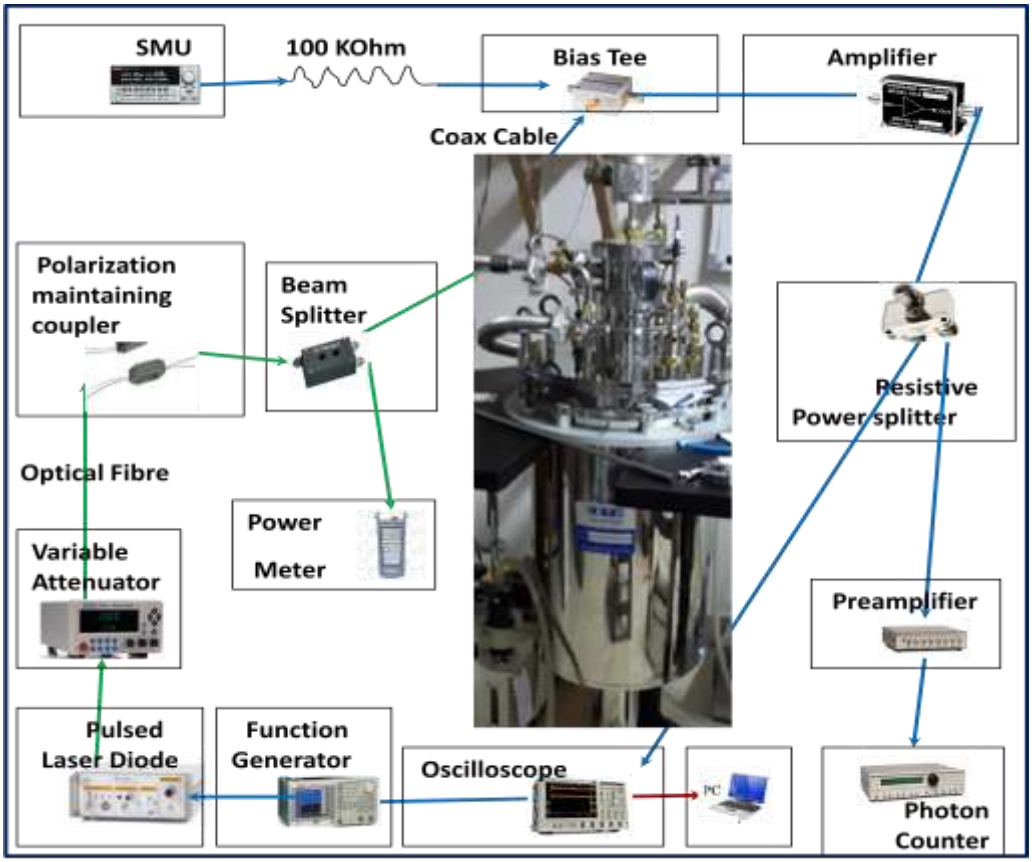

Fig.3.12: Setup for optical characterization of the device.

3.3.2 Characterization of laser source, photodetector and system automation

The continuous wave laser source (S1FC635) of 635nm is operated in the power range of maximum 2.5mW. The laser source is connected with the photodiode (DET025AFC) using single mode fibre (SM600) and its output is fed to the input of oscilloscope. The variation in the output voltage from photodiode with the variation in output power of laser source is in the form of DC voltage. The laser output is modulated using sine wave and is monitored in the oscilloscope. The output from photodiode is in the pulse form which can be used for counting the pulses by a photon counter. The modulation bandwidth of the signal is set up to 5kHz in the case of full depth of modulation (FDM) and 30kHz in case of small signal modulation (SSM). The output signal from photodiode is terminated in a 50Ω load and hence the output signal obtained is equal to the product of photo response current and load resistance. The output of photodetector from CW laser source is seen in the setup shown in Fig.3.13.

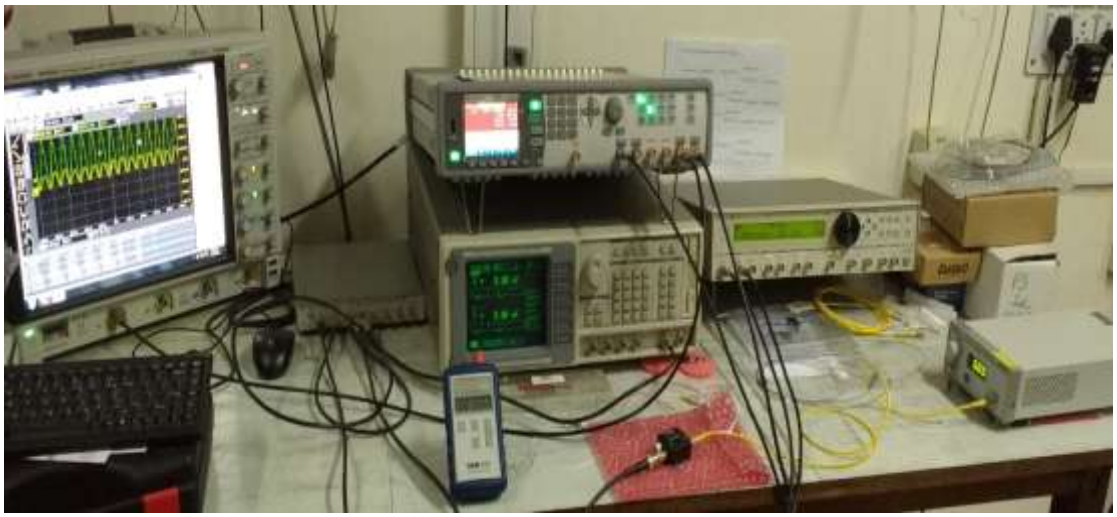

Fig.3.13: Real time measurement for laser characterization and modulation.

The program in LabVIEW platform is developed for optical characterization of the setup in automation mode. The output of the device at oscilloscope is monitored at the screen (Fig.3.14) and is saved for future reference. The number of pulses in a specified time can also be stored in the file with the help of photon counter.

Fig.3.15(a) is the number of counts of pulses versus frequency starting from 10kHz to 1MHz using IDQ801 in TCSPC setup. Fig.3.15(b) is the study of time jitter in the output of photodetector which happens to be 59ns. It can be seen that 50K pulse count occurred in 100ms at 100kHz and the response time was 99µs. In another case the time jitter was plotted at variable frequency and its variation was from 550ps to 725ps (Fig.3.15 (c)).

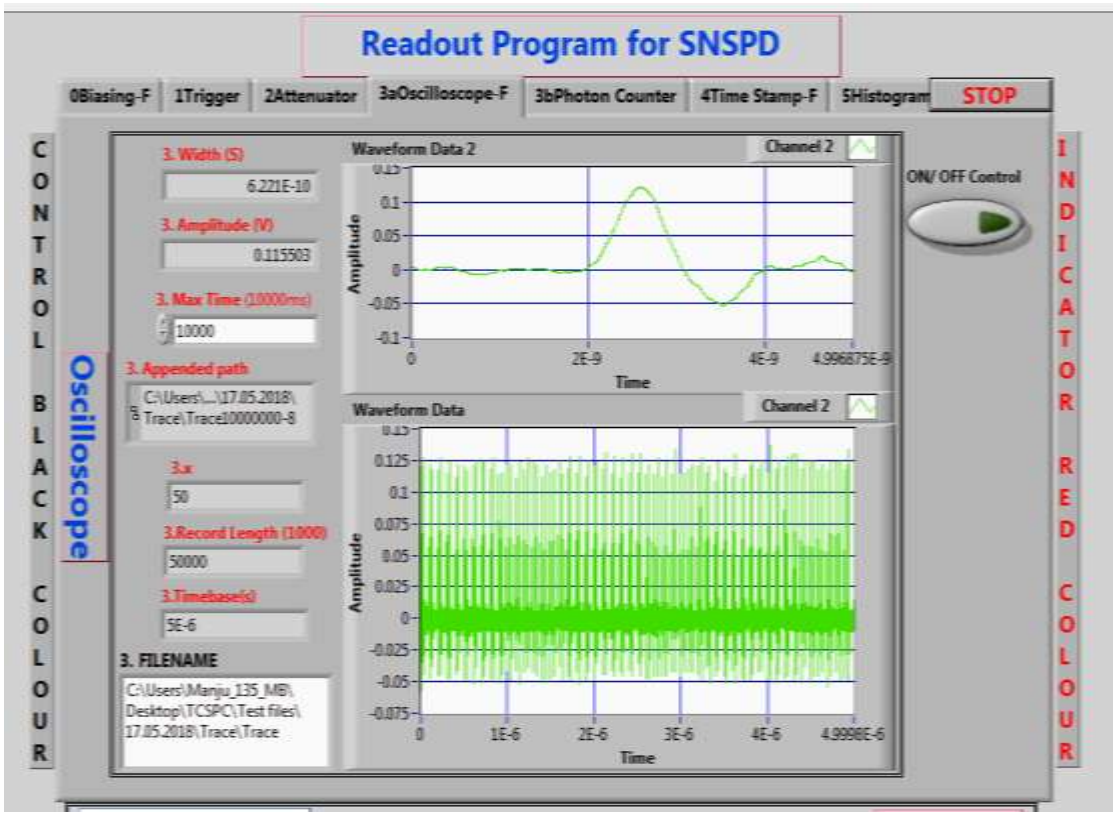

Fig.3.14: Front panel of the program for automation in optical characterization of the device.

Fig.3.16 (a) shows that variable frequency of laser source does not affect the amplitude of the output waveform from photodiode as the peak power of the laser pulse is always 1mW. The output of photodiode decreases (Fig.3.16(b)) as the attenuation of output power from laser source decreases. At -12dB attenuation of laser power the output of photodiode becomes 56mV after amplification and it becomes difficult to measure the output pulse from photodiode by further increasing the attenuation due to low SNR. It is seen that the minimum measurable voltage using photodiode is 56mV at average laser

power of -67dBm. The minimum number of photons detected by photodetector at 1550nm wavelength can be estimated as follows:

Average number of photons per pulse from laser source

= (3.16E-13x1550E-9)/(6.626E-34x3E+8)

= 2464031 photons per pulse

Average number of photons per pulse after attenuation (-54dBm)

= (3.98E-15x1550E-9)/(6.626E-34x3E+8)

= 31034 photons per pulse

Responsivity of Photodiode

= I_{PD}/P (0.95 A/W)

Pulse Energy

= Average Power x Tpulse

= 3.98nW x 1μs = 3.98E-15 J

Peak Power

= Pulse Energy/ Pulse Width

= 3.98E-15/ 300E-12 =0.01326 mW

Fibre Input InGaAs Biased Detector Output

= 0.0126 mA x 50Ω = 0.63 mV

Amplified o/p

= 63.0 mV (Actual o/p 56mV)

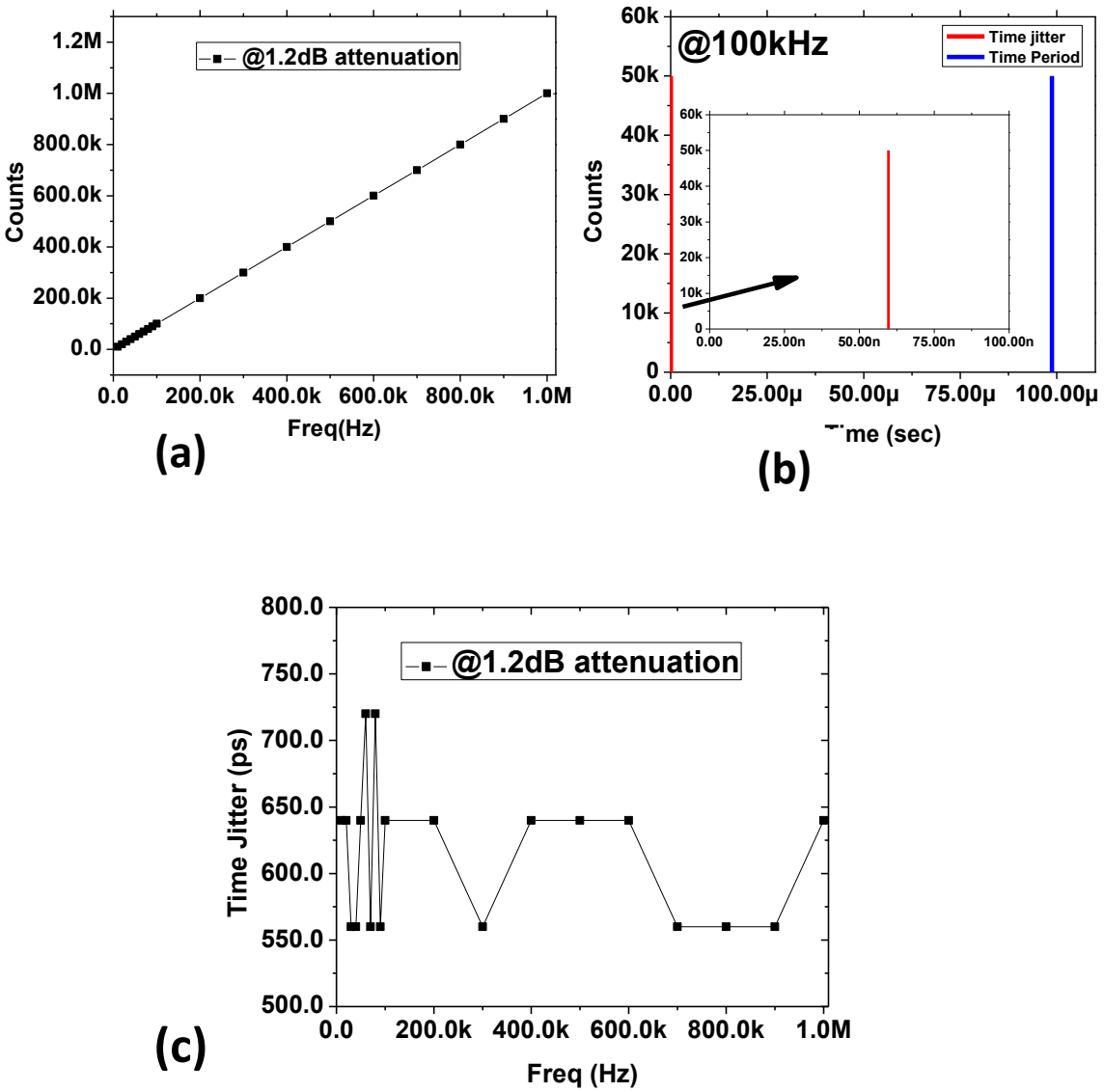

Fig.3.15: Study of (a) number of counts of pulses at different frequencies (b) response time and time jitter of the infrared photodetector and (c) time jitter at various frequencies.

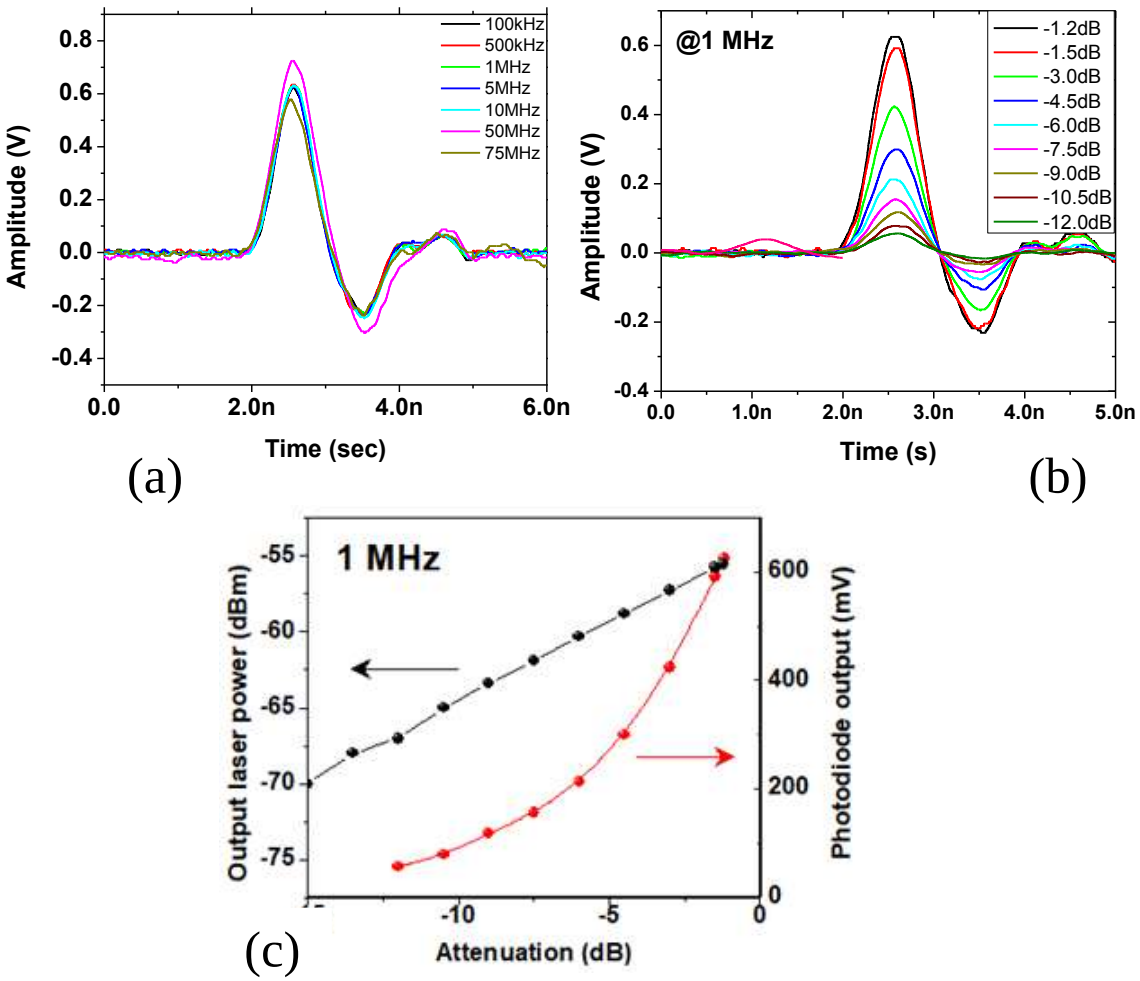

Fig.3.16 (a) Response pulse from photodetector at different frequencies (b) the response pulse at 1MHz at different attenuation levels and (c) variation of output laser power (black) and variation of amplitude of photodetector wrt variation in attenuation levels at 1550nm wavelength input from laser source at 1MHz.

3.4 Summary

This chapter reports on the design and development of a cryogenic setup down to ~1.8K for carrying out measurements on superconducting nanowire single photon detectors (SNSPDs). It has been found that variation in temperature is less than 10mK at lowest operating temperature. Apart from the above, another important advantage of the system is its low enough liquid helium loss rate (~100ml/hr) with all inserts which allows uninterrupted measurements for several days without any refilling of liquid helium. Further integration of optical setup has been discussed.

3.5 References

[1] J. Yin et al., "Quantum teleportation and entanglement distribution over 100-kilometre free-space channels", Nature **488**, 185 (2012).

[2] Ma Xiao-Song et al., "Quantum teleportation over 143 kilometres using active feed-forward", Nature **489**, 269 (2012).

[3] H. Takesue, S. D. Dyer, M. J. Stevens, V. Verma, R. P. Mirin, and S. W. Nam, "Quantum teleportation over 100 km of fibre using highly efficient superconducting nanowire single-photon detectors", Optica. **2**, 832 (2015).

[4] R. H. Hadfield, "Single-photon detectors for optical quantum information applications", Nat. Photon. **3**, 696 (2009). and references therein.

[5] S. Wang, W. Chen, J. -F. Guo, Z. -Q. Yin, H. -W. Li, Z. Zhou, G. –C. Guo, and Z. -F. Han, "2 GHz clock quantum key distribution over 260 km of standard telecom fibre", Opt. Lett. **37**, 1008 (2012).

[6] X. -C. Yao, T. -X. Wang, H. -Z. Chen, W. -B. Gao, A. G. Fowler, R. Raussendorf, Z. -B. Chen, N. -L. Liu, C. -Y. Lu, Y. -J. Deng, Y. -A. Chen, and J. -W. Pan, "Experimental demonstration of topological error correction", Nature **482**, 489 (2012).

[7] K. Shimizu, T. Honjo, M. Fujiwara, T. Ito, K. Tamaki, S. Miki, T. Yamashita, H. Terai, Z. Wang, and M. Sasaki, "Performance of long-distance quantum key distribution over 90-km optical links installed in a field environment of Tokyo metropolitan area", J. Lightwave Technol. **32**, 141 (2014).

[8] T. E. Northup and R. Blatt, "Quantum information transfer using photons", Nat. Photon. **8**, 356 (2014).

[9] B. Korzh, C.C.W. Lim, R. Houlmann, N. Gisin, M. J. Li, D. Nolan, B. Sanguinetti, R. Thew, and H. Zbinden, "Provably secure and practical quantum key distribution over 307 km of optical fibre", Nat. Photon. **9**, 163 (2014).

[10] Z. L. Yuana, J. F. Dynes, and A. J. Shields, "Resilience of gated avalanche photodiodes against bright illumination attacks in quantum cryptography", Appl. Phys. Lett. **98**, 231104 (2011).

[11] M. A. Itzler, X. Jiang, M. Entwistle, K. Slomkowski, A. Tosi, F. Acerbi, F. Zappa, and S. Cova, "Advances in InGaAsP-based avalanche diode single photon detectors", J. Modern Optics. **58,** 174 (2011).

[12] G. N. Gol'tsman, , O. Okunev, G. Chulkova, A. Lipatov, A. Semenov, K. Smirnov, B. Voronov, A. Dzardanov, C. Williams, and R. Sobolewski, "Picosecond superconducting single-photon optical detector", Appl. Phys. Lett. **79**, 705 (2001).

[13] M. D. Eisaman, J. Fan, A. Migdal, and S. V. Polyakov, "Invited review article: Single-photon sources and detectors", Rev. Sci. Instrum. **82**, 071101 (2011) and references therein.

[14] C. M. Natarajan, M. G. Tanner, and R. H. Hadfield, "Superconducting nanowire single-photon detectors: physics and applications", Supercond. Sci. Technol. **25**, 063001 (2012) and references therein

[15] A. E. Lita, A. J. Miller, and S. W. Nam, "Counting near-infrared single-photons with 95% efficiency", Opt. Express **16**, 3032 (2008).

[16] S. Miki, M. Fujiwara, M. Sasaki, B. Baek, A. J. Miller, R. H. Hadfield, S. W. Nam, and Z. Wang, "Large sensitive-area NbN nanowire superconducting single-photon detectors fabricated on single-crystal MgO substrates", Appl. Phys. Lett. **92**, 061116 (2008).

[17] A. Korneev, Y. Korneeva, N. Manova, P. Larionov, A. Divochiy, A. Semenov, G. Chulkova, Y. Vachtomin, K. Smirnov, and G. Gol'tsman, "Recent nanowire superconducting single-photon detector optimization for practical applications", IEEE Trans. Appl. Supercond. **23**, 2201204 (2013).

[18] A. J. Salim, A. Eftekharian, and A. H. Majedi, "High quantum efficiency and low dark count rate in multi-layer superconducting nanowire single-photon detectors", J. of Appl. Phys. **115**, 054514 (2014).

[19] M. K. Akhlaghi, H. Atikian, A. Eftekharian, M. Loncar, and A. H. Majedi, "Reduced Dark Counts in Optimized Geometries for Superconducting Nanowire Single Photon Detectors", Optics Express **20**, 23610 (2012).

[20] J. -L. F. –X. Orgiazzi, A. H. Majedi, "Robust packaging technique and characterization of fibre-pigtailed superconducting NbN nanowire single photon detectors", IEEE Tran. Appl. Supercond. **19**, 341 (2009).

CHAPTER 4

THIN FILM FABRICATION AND CHARACTERIZATION

4.1 Introduction

In this chapter the details about the NbN then film growth and characterization are discussed. The optimization of the film was performed for improved superconducting properties. Comparatively thicker films (≈50nm) were deposited for initial optimization. Thinner films of about 10nm were optimized in the next step towards their applications for single photon detection. Reactive DC magnetron sputtering technique has been employed for depositing high quality superconducting thin films of NbN. Magnetization measurements were carried out using a Quantum Design USA make 7T magnetic property measurement system (MPMS). The conventional four point probe method was also used to evaluate superconducting properties of the films down to 1.8K.

4.2 Superconductivity in NbN

NbN is a BCS superconductor with an energy gap of ~ 5 meV. The magnetic penetration depth of NbN is close to 200nm and the coherence length is < 5 nm. In thin film of NbN the superconducting properties are very much dependent on their microstructure. The nitrogen partial pressure during deposition is one of the most important factors which control the grain-boundary resistance and the effective coupling between neighboring grains. Films grown at lower temperatures show a granular microstructure with randomly oriented grains. It has been observed that the normal state transport as well as superconducting properties of NbN are greatly influenced by the degree of crystallinity. The normal state resistivity of polycrystalline films can vary from 100 - 2000μΩ-cm although the Tc remains the same as that of epitaxial films. The higher normal-state resistivity is primarily due to inter-grain conduction across the insulating grain boundaries.

4.3 NbN as a test system

We have selected NbN as a test system to study the effect of nanopatterning on the superconducting state of strong type-II superconductor. NbN is particularly suitable for such studies because of its high transition temperature and high critical current density. An essential research direction in the field of SNSPDs is to increase device performances by defining distributed Bragg reflector (DBR) prior to deposition of superconducting layer. It has been found that thin films of NbN with fairly high critical temperature can be fabricated at relatively low growth temperatures. This feature makes it possible to integrate NbN into hybrid structures without much inter diffusion at its interface. Moreover, since the demonstration of the first SNSPD, NbN has primarily been used as the superconducting materials. NbN devices have demonstrated device detection efficiencies as high as ~ 80% , hundreds of MHz count rates, less than 50 picoseconds jitter as well as very low dark count rate. In addition, the dead time is the order of a few nanoseconds. Therefore, it is essential to develop detectors based on NbN at the initial stage as a reference system for setting up and optimization of single photon detection facility.

4.3.1 NbN thin film growth and optimization

Growth of NbN thin films for its application in superconducting nanowire single photon detector (SNSPD) require thickness to the order of few nanometers (5nm-10nm). An optimized deposition process in the presence of high vacuum is required for fabrication of films with thickness of few nanometers.

4.3.2 Sputter deposition system

The schematic of the sputter deposition system is shown in Fig.4.1. It is a multichamber sputtering system for deposition of a variety of materials. It consists of three deposition chamber and a loadlock connected in series. The sample transfer arm with a substrate mounting heater at the end facilitates access to reach to any chamber for deposition. There are gate valves installed along the transfer line to isolate the chamber from each other as and when requires. Some of the important components of the deposition system are described below.

Load lock: It is a small cylindrical chamber which is used for mounting (demounting) of substrate (sample). The chamber is connected to pumping system. Prior to transfer of substrate to any of the deposition chambers loadlock is evacuated to at least 3- 4E-7 mbar pressure.

Deposition chamber: Each spherical chamber (12 inch dia.) has provision to mount three sputtering modules at a time which facilitates sequential deposition of different materials to create multilayer structure. Each sputtering module is dedicated for a particular material to avoid any contamination. Water cooled sputtering modules are designed for 2 inch dia. target. It consists of two parts - inner part is meant for housing magnet and target while the second part works as outer shield. Fig.4.2 shows picture of a magnetron sputtering module with all relevant details. The target is connected to the negative terminal of high voltage DC power supply whereas the outer part to the ground.

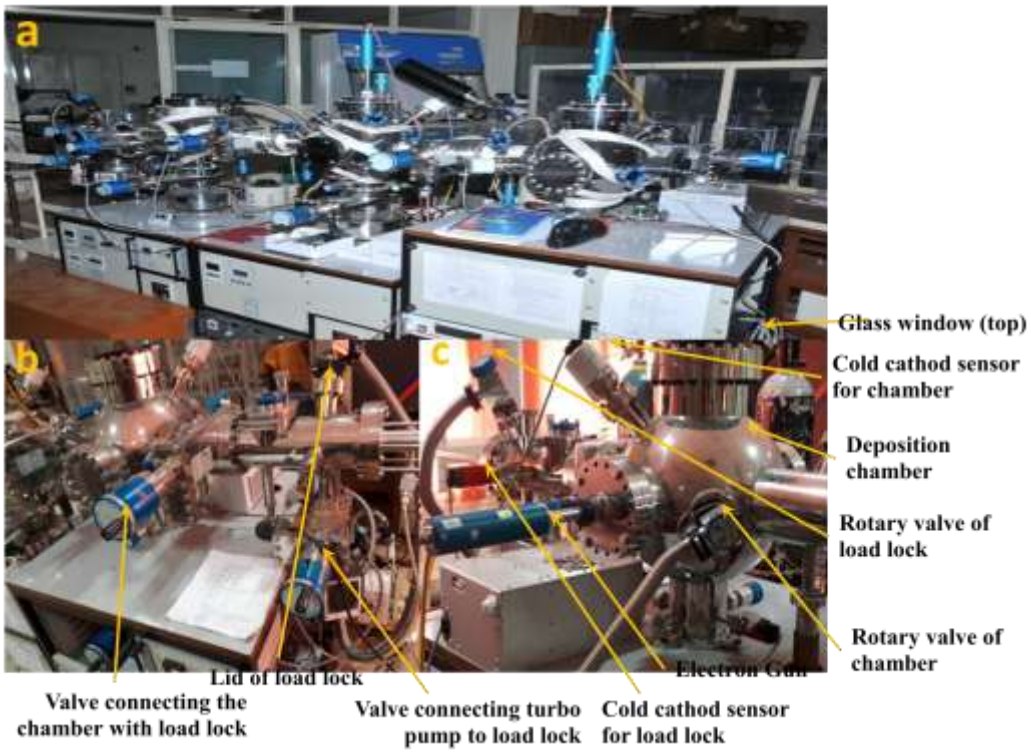

Fig.4.1: (a) Multi chamber sputtering system (b) Front view of the deposition chamber (c) Back view of the deposition chamber.

Magnetron sputtering module: Thin film microstructure depends on the deposition technique adopted for fabrication [1]. In DC magnetron sputtering technique the flux reaches the substrate from limited direction, hence the film grows in columnar manner [2]. In sputtering, the transportation of coating materials is controlled by the distance between target and substrate and the gas pressure whereas the diffusion is controlled by the substrate temperature and the energy of the particles emitted from the target [2]. Structure zone model defines the relation between the deposition parameters and the microstructure of the film [3-6].

The pressure inside the chamber in DC magnetron sputtering has both the upper and lower limits. It is kept within the range for desirable microstructure/ stoichiometry of the film. The more gas pressure gives rise to scattering of sputtered particles which results in the loss of kinetic energy as well as randomization of their incidence angle on the substrate. The lower limit is maintained to ensure that the emitting electrons from cathode collide with the gas particles and ionization take place to maintain plasma before they reach the substrate for final deposition.

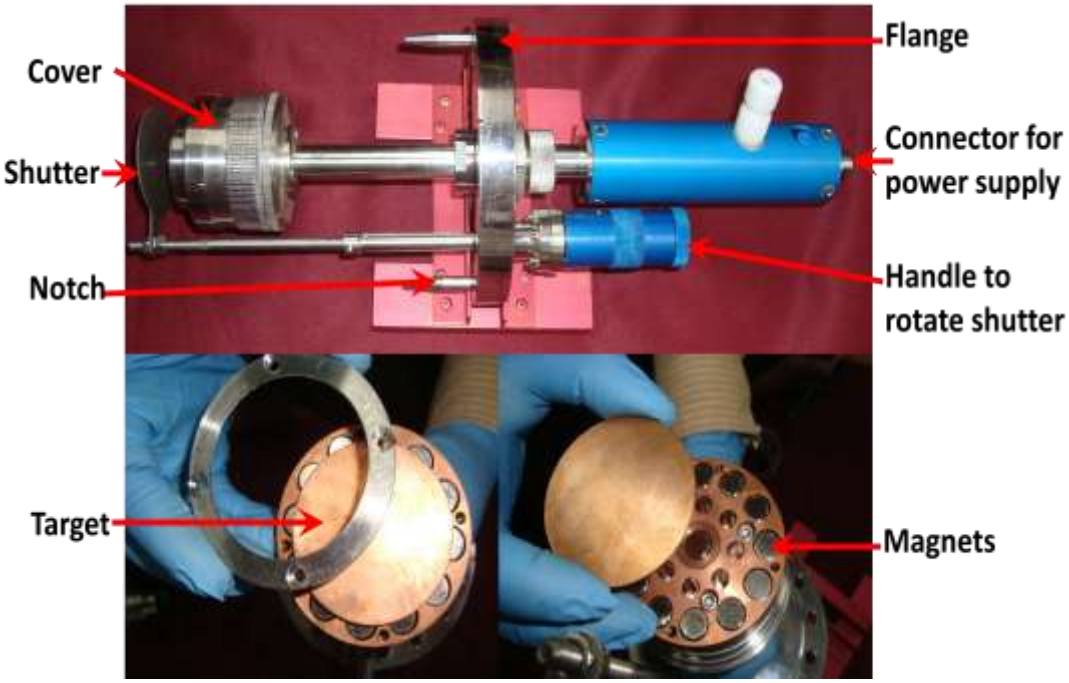

Fig.4.2: Side view of the (a) magnetron sputtering gun, front view of the magnetron sputtering gun showing (b) target after removal of cover and (c) magnets beneath the target.

The magnetic field at cathode helps the particles emitted from target to retain high kinetic energy for longer duration before finally settling down at the substrate. It also helps localization of plasma over the target resulting in lower plasma density over substrate and finally helps in fabrication of thin film of the order of few nanometers. Ion bombardment can be controlled using magnetron sputtering which is useful in modifying film microstructure.

Vacuum pump: All the chambers including load lock are connected with independent and separate two stage pumping system. At the first stage oil based rotary pump is used to create the vacuum inside the chamber. Once the vacuum reaches to the level of ~1E-2 mbar, the chamber is connected with the second stage turbo molecular pumping system. The base pressure of the chamber varies from 1E-7 mbar to 7E-8 mbar depending on the surrounding environments.

Pressure gauge: Two types of pressure gauge are mounted in each the chamber. One is pirani gauge sensor and another one is cold cathode sensor. Cold cathode sensor is capable of monitoring pressure in the range of E-3 to E-10 mbar. This is used to read the base pressure of the chamber and turns off before the deposition process. The pirani gauge monitors pressure in the range of E+3 to E-3 mbar and hence is suitable for precise monitoring of chamber pressure during film growth.

Mass flow controller (MFC): Ar and N_2 fluxes are controlled independently using separate MFCs. The MFCs are calibrated for designated gas for accurate control and reproducibility of gas flow inside the chamber.

4.3.3 Thin film deposition procedures

The following procedure is followed while depositing the thin film.

4.3.3.1 Sample cleaning

This procedure is performed to cleave bigger wafer/substrate into 5 x 5mm^2 pieces. The cleaving is performed by using diamond tip scriber manually. Standard cleaning method in ultrasonic bath is performed afterwards prior to fixing of the wafer on the mounting heater block for deposition.

4.3.3.2 Wafer/substrate mounting

The transfer arm is pulled out and placed inside the load lock. The load lock chamber is then required to be vented with dry N_2. Already cleaned wafers are then pasted on heater block with vacuum compatible silver epoxy. The heater block is then heated to about 60-70^{o}C for about 20 to 30 minutes for drying of silver epoxy and to remove organic solvents which otherwise would cause contamination of deposition chamber. The load lock is evacuated afterwards till the vacuum reaches to the order of E-7 mbar. Gate valves along the transfer line are required to be opened to bring the heater block in the deposition chamber. Here it is important to mention that there is a differential pumping zone which needs to be activated during the transfer to avoid any external gas to enter inside the vacuum system.

Wafer mounting with shadow mask: In this case the wafer is mounted along with a shadow mask clipped on top of sample. For instance, mask as shown in Fig.4.3 made out of hard electroformed nickel is used for generating in-situ patterns of 25µm wide lines with contact pads for four probe transport measurements.

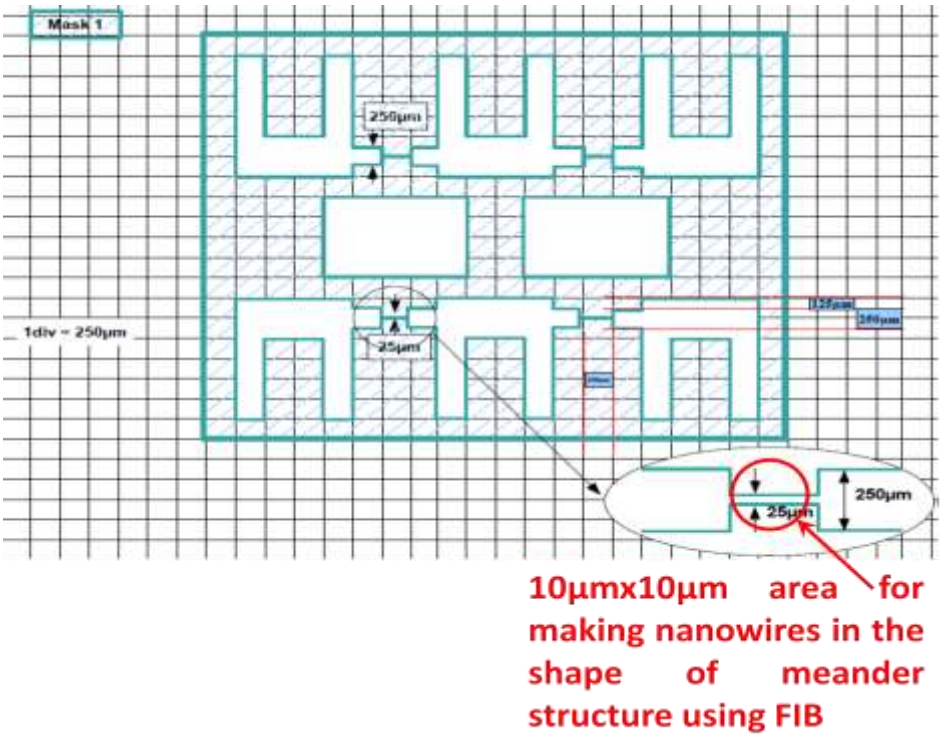

Fig.4.3: Shadow mask with 25µmx250µm feature size for making nanowires in meander structure in an area of 10µm x 10µm.

4.3.3.3 Purging/ flushing the chamber

Prior to deposition, the chamber is flushed with N_2 gas with a flow rate of 20sccm (standard cubic centimeter per minute) to reduce the presence of any unwanted gas species inside the chamber more specifically oxygen and moisture. The chamber pressure is maintained at 5E-2 mbar N_2 pressure by partially closed the gate valve between the deposition chamber and turbo molecular pump during this process. It is important to mention here that the pumping system sets to run in standby to avoid overheating during the exercise and also during film growth. The flushing continues for about an hour with 5 minutes pause after every 15 minutes of flushing.

4.3.3.4 Wafer heating

Once the chamber base pressure reached back to 1E-7 mbar after the flushing the heater block is turned on and set the temperature to a desired value. The temperature of the heater block is PID controlled and connected with 8-segment controller to assign different heating rate and hold time at different temperature regime. For precise monitoring of temperature a type-K (chromel/alumel) thermocouple is placed inside the heating block and very close to the wafer mounting surface. The distance between the sputtering target and the heater block can be adjusted between any values from 6 - 12cm without breaking the vacuum. However, it is not desirable once the chamber is conditioned for deposition.

4.3.3.5 Gas flow controlling

Once the desired temperature is achieved MFCs are turn on to maintain flows of N_2 and Ar inside the chamber to a desired ratio. For instance, 28sccm flow of Ar and 4sccm flow of N_2 provides NbN films with the best superconducting properties. The deposition of NbN takes place at a total chamber pressure of 7E-3 mbar.

4.3.3.6 Thin film deposition with DC magnetron sputtering

Formation of Ar plasma is initiated by applying a DC bias between the target and the outer shield. The gap between the target surface and the outer shield is kept within a millimeter during the mounting of target. The electric filed that is being created due to the potential difference initiates Ar plasma formation once the threshold value is

reached which then grows with the increasing bias voltage. The accelerated Argon plasma removes materials from the target and in presence of N_2 forms NbN in case of Nb sputtering. In our case the deposition of NbN was optimized at about 190W (300V and 0.63A) of DC power. The target is required to be pre-conditioned for about a minute to remove the surface layer before the wafer is exposed to the plasma to initiate film growth. The deposition is continued for about 5 minutes. Immediately after the deposition the wafer is set to cool down to room temperate at a desired rate in vacuum. It is important to remember that the sputtering sources are water cooled. Hence the flow of chilled water is required to be maintained during the while course of deposition. The circulation of chilled water is in principle should continue for about 15 - 20 minutes after the growth to ensure that the sputtering source is brought back to normal temperature. This prevents damage of the magnet assembly inside the source.

4.3.3.7 Demounting the sample

The heater block is moved back from chamber to the load lock and the gate valve separating the load lock and chamber is placed in closed position. The load lock after disconnecting from the pumping line is vented with dry N_2 for removing of sample.

4.4 Thickness calibration

Thickness measurement and optimization is very important factor in deciding the deposition time particularly, in the case of ultra thin films.

4.4.1 Measurement setup

Thickness was measured using stylus based surface profilometer (Make - AEP Technology, Model - NanoMap-500LS). The thickness profiler comes with software for controlling the equipment. It can be programmed for short (range < 500µm) as well long scan (range: 500µm to 50,000µm). The measured data can be analyzed with all the parameters calculated using SPIP software. The system has been tested with 8nm step height standard. The horizontal resolution is controlled by the scan speed and data sampling rate.

4.4.2 Setup configuration

The measurements are performed in 2D mode to get a line profile scan across the sample. The contact force which can be varied from 0.1mg to 100mg are chosen carefully depending on sample material, tip radius and scanning speed, In case of NbN contact it keeps between 2 - 3mg. The NbN film of about 100nm is chosen for thickness calibration. Based on the thickness calibration deposition time is estimated for thinner films down to 10nm. The detail scan parameters for the measurement are list as follows.

Table.4.1: Thickness measurement parameters

S. No.	Parameters	Values
1.	Vertical range	5µm
2.	Scan distance	750 - 1000µm
3.	Scan speed	50µm/sec
4.	Sample frequency	100 pts/ sec
5.	Number of points / scan	1500
6.	Data resolution	0.5µm
7.	Contact force	2 - 3 mg

The thickness of the sample is about 100nm for 5 minutes deposition at 190W sputtering power. A typical thickness profile on SPIP software is shown in Fig.4.4. The average deposition rate is calculated to be 0.33nm/sec. Based on this the deposition time can is estimated to be 30 seconds for 10nm thick NbN films. Shadow mask used during film growth for thickness calibration, NbN film after deposition on a glass surface and thin film samples for nanostructure fabrication can be seen in the Fig.4.5.

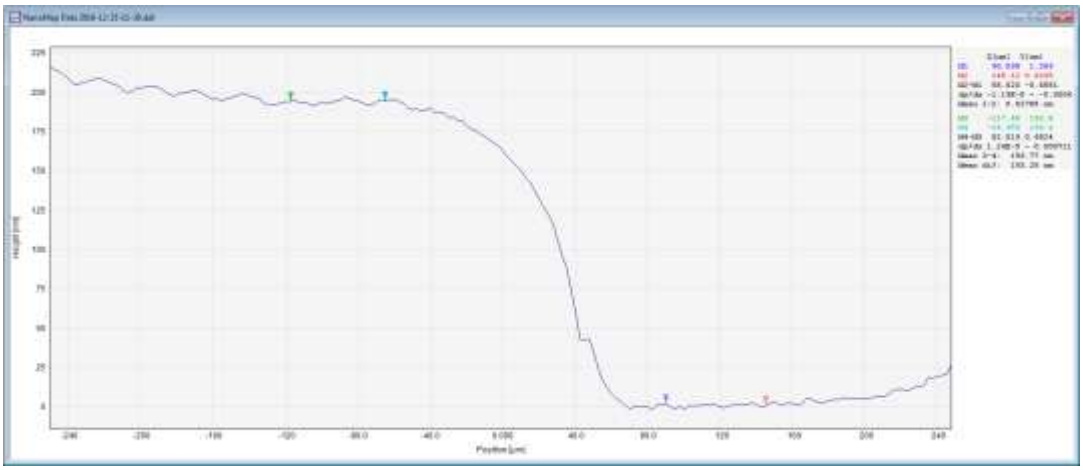

Fig.4.4 Thickness profile of sample with the help of surface profiler and SPIP software.

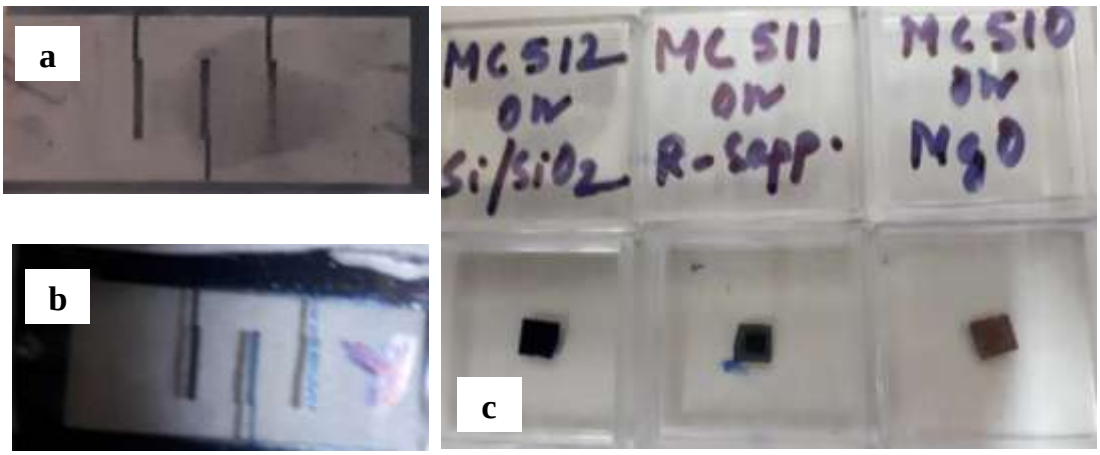

Fig.4.5: (a) shadow mask, (b) NbN lines on glass slide for thickness measurement, (c) thin NbN films on 5mm x 5mm Si/SiO_2, R-sapphire and Mgo substrate prepared for nanostructure fabrication.

4.5 NbN thin film optimization

The reaction between Nb and N_2 takes place at (1) target surface, (2) substrate surface and (3) in the path of target particles transportation to substrate. So, the stoichiometry of Nb-N film is very much dependent on the deposition parameters which control the ratio between sputtered material and reaction dynamics. The balance between sputtering and nitridization can be achieved in many ways as described below:

- By changing the ratio of N_2/Ar flow and keeping the total pressure (P_{total}) and applied voltage same.
- By changing the P_{N2} while keeping P_{Ar} and applied voltage same.
- By changing the P_{Ar} while keeping P_{N2} and applied voltage same.

Given below are the few important parameters and their role in control of the film microstructure as well as critical temperature.

4.5.1 Substrate temperature

The temperature of substrate during growth (Ts) plays an important role[7-9]. The melting point of NbN is $T_M \approx 2570^oC$. The motion of atoms at substrate surface depends strongly on the ratio of its temperature and melting point of NbN. For $T_S < 0.3T_M$ the motion of atoms at substrate surface is quite less and the diffusion of atoms

cannot take place whereas the transportation of atoms to substrate is quite fast which makes it difficult to get homogeneous thin films [2].

For $T_S > 0.5T_M$ the bulk diffusion takes place at the surface of the substrate. It was found that the intermediate range of temperature $0.3T_M < T_S < 0.5T_M$ is most suitable.

4.5.2 Plasma pressure

Energy flux towards the substrate and its angle of incidence depends mostly on the P_{total}. At lower P_{total} thin films trends to degrade due to excessive bombardment of neutral particles while at higher P_{total} excess of valence electrons prevents the system to reach a thermal equilibrium.

4.5.3 Target erosion

Target erosion is the formation of a ring shaped groove on the target surface after several uses. In this case sputtered particles have more collision in the groove and hence more energy loss occurs which results in the particles reaching the substrate with less energy. Also increase in area due to formation of groove results in decrease of effective power density which reduces the sputtering rate. Target erosion affects both the microstructure as well as stoichiometry of the sputtered film [10-12].

4.5.4 Substrate bias

Substrate bias controls the energy delivered to the substrate through ion collision. The logic behind keeping the substrate bias at ground is to avoid the negative charge formation at substrate due to arrival of electrons that escape from the magnetic trap of the target. This negative charge consequently attracts the positive Ar^+ ion resulting in enhancement of the energy with which it bombards at the substrate surface.

4.5.5 Target substrate distance

The microstructure of film gets affected by the change in distance between target and substrate. The energy with which sputtering atoms collide with the substrate or the neutral particles reach the substrate changes with the gap between target and substrate [11-13].

4.6 Optimization of parameters used for fabrication

The work presented here deals with the fabrication of ultrathin niobium nitride (NbN) films with desired superconducting properties, for the fabrication of superconducting nanostructures and its application as single photon detectors. Thin films of NbN are deposited using reactive magnetron sputtering. The dependence of Tc as a function of argon (Ar) and nitrogen (N_2) is studied systematically. Relatively thick (50nm) NbN and single crystal MgO (001) as substrate were preferred for the optimization of initial deposition parameters to facilitate epitaxial growth. In the next step, ultrathin films of NbN on 300nm SiO_2 coated silicon (Si) substrates at a lower temperature was optimized to avoid primarily the formation of stable Nb_2O_5 dielectric which crystallizes at around 500°C [14] and secondly the degradation of underlying layers or pre-coated polymer resist for lithographic patterning. Although thicker films grown at relatively low temperature and even at ambient substrate temperature were reported earlier, synthesizing ultrathin NbN films with desired superconducting properties is always a challenge due to proximity effect [15-17].

NbN films are deposited on MgO (100) single crystal as well as on 300nm SiO_2 coated p-type boron doped Silicon (100) substrates with resistivity ranging between 1 – 10Ω-cm by the reactive dc magnetron sputter process from a 2" diameter 99.95% pure metallic Nb target in an reactive gas mixture of 5N pure Ar and N_2. The flow rates of Ar and N_2 were controlled and monitored separately to understand their role on Tc. The base vacuum of sputter chamber was 1E-7 mbar and the deposition was carried out at a total chamber pressure of 7E-3 mbar. The MgO substrates were kept at 600°C during deposition while thinner films of NbN were deposited at 200°C on Si/SiO_2. MgO and Si/SiO_2 substrates were prebaked in base vacuum at 800°C and 200°C respectively for an hour prior to deposition. Thickness of the deposited films was measured using stylus profiler. The deposition rate is estimated to be 20nm/minute. Once optimized, the process parameters were kept unchanged and thinner films were grown on Si/SiO_2 assuming the same deposition rate.

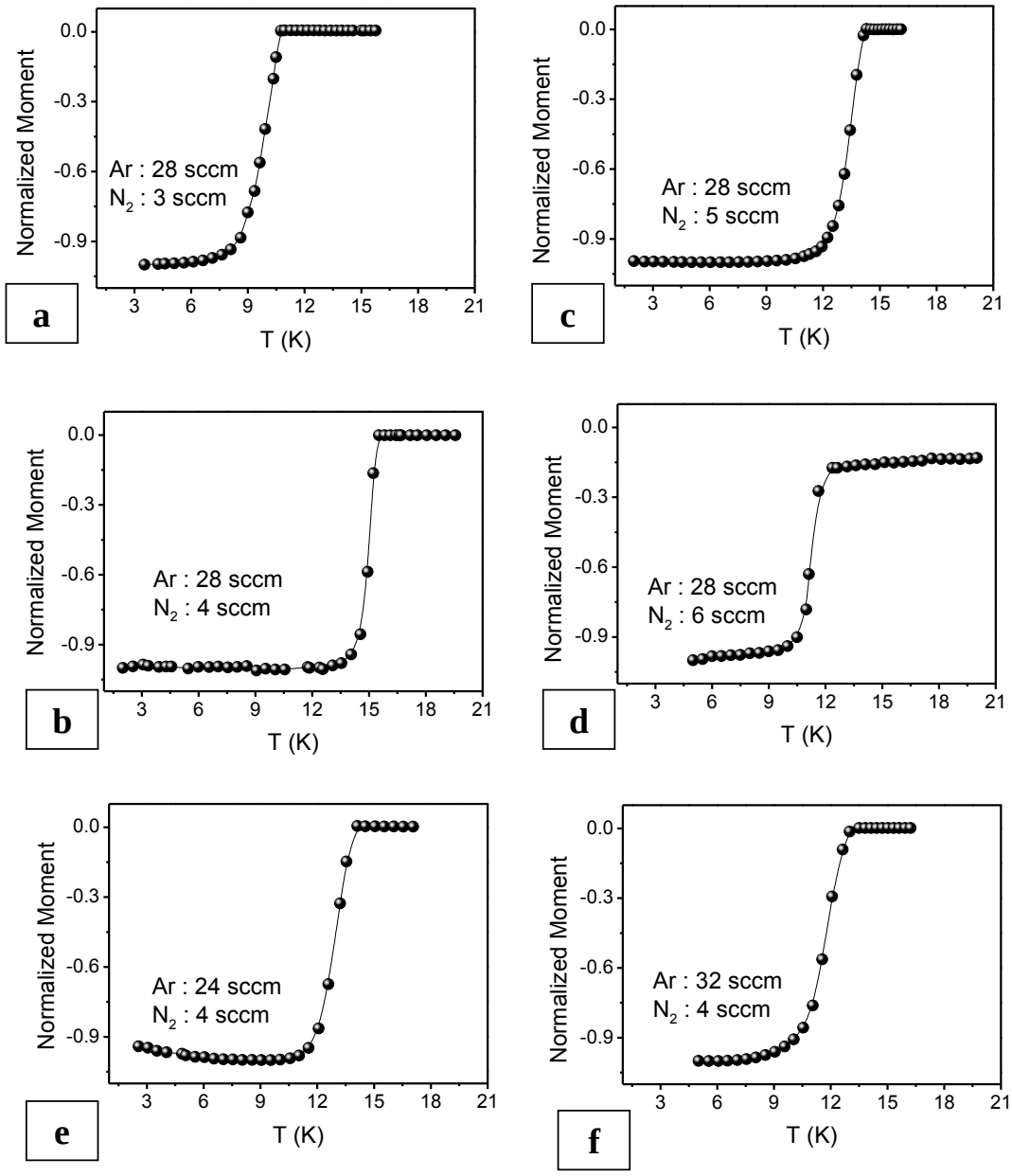

Fig.4.6: Normalized magnetic moment vs temperature plots of 50nm thick NbN films grown at 600°C and deposited at different ratio of argon-nitrogen gas mixture. Magnetization measurements were performed at 100G applied field. Prior to the measurements, samples were first cooled in zero-field down to the lowest temperatures.

Fig.4.6 shows the dependence of Tc on ratio of Ar and N_2 gas mixture. Tc is deduced from zero-field-cooled (ZFC) magnetization measurements as a function of temperature. Plots of variation in Tc with N_2 injection at a constant 28sccm Ar flow can be seen in Fig.4.6 (a), (b), (c) and (d). Tc initially increases with the increase of

N_2 content, reaches to a maximum at 4sccm of N_2 flow, and decreases for further increase of N_2 flow. Dependence of Tc follows the similar trend (Fig.4.6.(b), (e), (f)) when the Ar content in the chamber during the deposition varies from 24sccm to 32sccm for a fixed 4sccm N_2 flow. The Tc goes through a maximum at 28sccm Ar flow. The similar trends have been observed by previous workers and this has been attributed to gradual change in crystal structures [17]. The maximum Tc of NbN thin films is associated with the cubic B1 (fcc NaCl) phase. The monotonic decrease of Tc from its maximum value at both sides as the ratio of Ar and N_2 mixture changes from optimum value is associated with deviation of metal to nitrogen ratio from unity leading to gradual transition from cubic to tetragonal phase. Hall effect measurements on NbN thin films earlier revealed that the carrier concentration of NbN is sensitive to deposition growth condition and that the Tc of NbN is governed primarily by the carrier density. The deviation from equiatomic stoichiometric NbN leads reduction of carrier density due to increase of either Nb or N vacancies. It is possible that the structural transition is accompanied with the change in electronic band structure in NbN system [18].

Fig.4.7 (a) shows the dependence of transition temperature (Tc) on the change in flow of N_2 gas. It can be seen that maximum Tc is achieved by maintaining the N_2 flow at 4sccm. Fig.4.7 (b) shows the optimization of the Tc of NbN thin film by keeping the N_2 flow constant for which Tc was found maximum whereas varying the Ar flow from 24sccm to 32sccm. It can be seen that a maximum Tc of about 15.5K can be achieved at 4sccm of N_2 flow and 28sccm of Ar flow where rest of the parameters are kept at same optimized value.

Films of NbN were also deposited at a higher temperature. As shown in Fig.4.8 the NbN films of 50nm thick grown at 700°C has a lower Tc almost by 1.2K than the films grown at 600°C which is contrary to the expected trend, which predicts an increased fraction of B1 phase leading to improved superconducting properties with increasing deposition temperature. We believe this is likely due to the oxidation of NbN thin films during cooling in vacuum immediately after the deposition. Previous

studies on ultrathin NbN confirm from the TEM and EELS analyses the formation of an amorphous layer at the film-substrate interface due to inter-diffusion of niobium, silicon, nitrogen, oxygen at higher deposition temperatures [17].

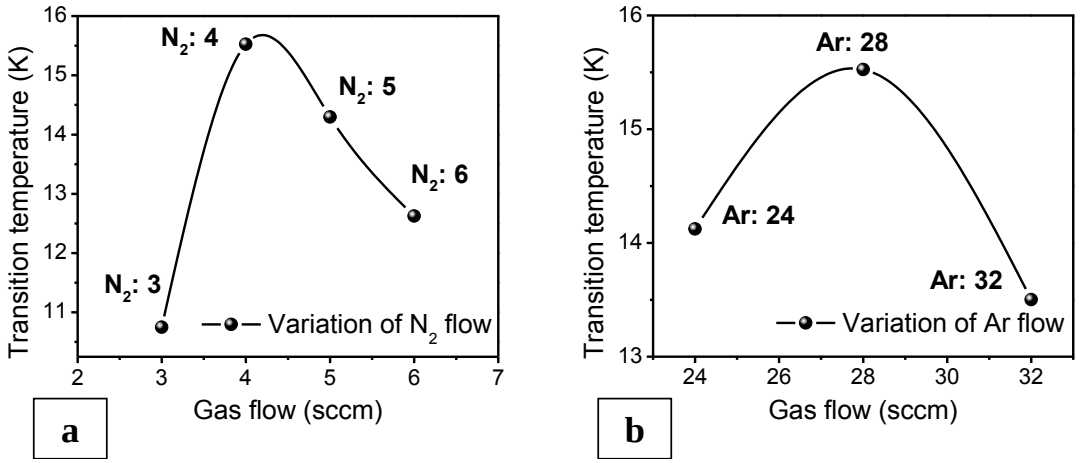

Fig.4.7: Dependence of superconducting transition temperature (T_c) of NbN thin films on ratio of argon-nitrogen gas mixture. Plot on the left side of the figure (a) is for the films synthesized by keeping the Ar flow fixed at 28 sccm while the N_2 flow was varied from 3 to 6 sccm. (b) shows the variation of T_c with argon flow for films synthesized at a fixed 4sccm N_2flow.

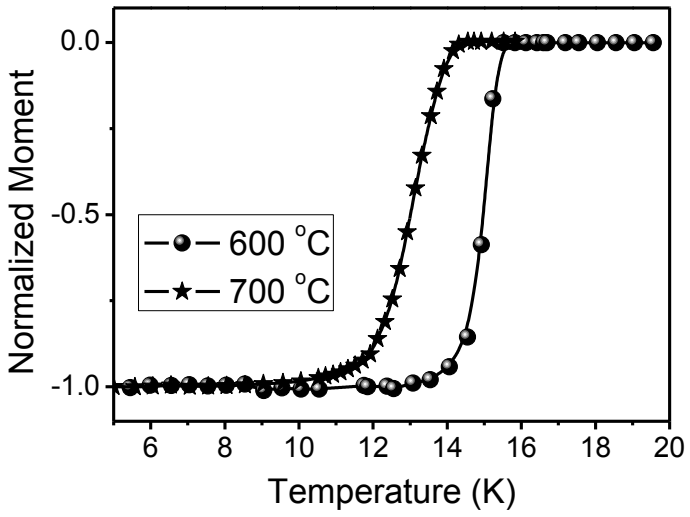

Fig.4.8: Normalized magnetic moment vs temperature plots of 50nm thick NbN films grown at 600°C and 700°C. Magnetization measurements were performed at 100G applied field. Prior to the measurements samples were first cooled in zero-field down to the lowest temperatures.

NbN thin film samples were also grown on Si/SiO_2 at 200°C substrate temperature with Ar to N_2 ratio of 7:1 for nanopatterning using FIB technique. The sputtering power of 190W was used to maintain the growth rate. Thickness of the NbN film was controlled by the deposition time. It can be seen from the resistance vs temperature plot of 10nm thick NbN grown (Fig.4.9) that there is no degradation of superconductivity in terms of Tc and transition width (ΔT). The best sample in the form of 25μm wide strip shows Tc of about 15.5K with $\Delta T \approx 1K$. Drastic reduction of Tc in ultra thin superconducting films with thickness comparable to the coherence length is only natural and can be explained in the framework of intrinsic proximity effect [19]. Based on the numerical calculation as proposed by Fominov et al. [19] Llin et al. [17] has estimated a 0.6nm thick non-superconducting boundary layers at each side of the superconductor which essentially reduces the thickness of superconducting channel from the measured value.

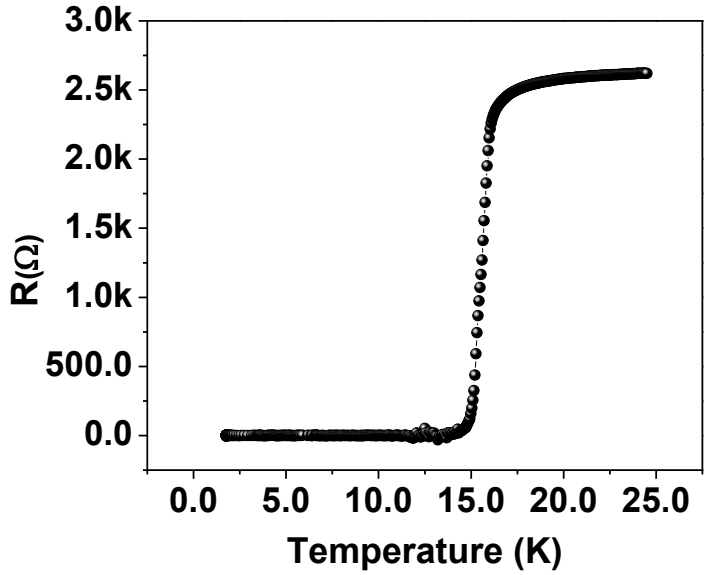

Fig.4.9: RT measurement of NbN 10nm thin film deposited at 200°C.

Table.4.2 shows the summary of optimized deposition parameters of NbN films down to 10nm thick in terms of superconducting properties.

Table.4.2: Optimized recipe for NbN thin film fabrication:

S. No.	Parameter	Value
1.	Deposition method	DC magnetron sputtering technique
2.	Target	Nb
3.	Substrate	MgO and Si/SiO_2
4.	Substrate size	5mmx5mm
5.	Target and Substrate distance (gap)	10cm
6.	Base pressure	1E-7 mbar
7.	Ar flow	24sccn
8.	N_2 Flow	4sccm
m9.	Standby speed	700Hz
10.	Deposition pressure	7E-3mbar
11.	Deposition temperature	200 ^oC, 600^oC
12.	Deposition power	0.63A x 0.30V ≈ 190W

4.7 Summary

In summary, ultrathin films of NbN have been synthesized employing DC magnetron sputtering. The chapter includes a detailed discussion on deposition facility. The optimization of NbN thin film fabrication for high T_c has been performed. The effects of deposition conditions, particularly the ratio of Ar/N_2 have been studied in an effort to optimize superconducting properties in NbN.

4.8 References

[1] A. M. Kadin, in "Introduction to superconducting circuits", Wiley, New York, 1999, Chap 2.

[2] K. Tanabe, "Ellipsometric and optical reflectivity studies of reactively sputtered NbN thin films", J Appl Phys. **63**, 1733 (1988)

[3] J. A. Thornton, "High rate rhick film growth", Ann. Rev. Mater. Sci. 7, 239 (1977).

[4] J. A. Thornton, "Influence of substrate temperature and deposition rate on structure of thick sputtered Cu coatings", J. Vac. Sci. Technol. **11**, 666 (1973).

[5] J. A. Thornton, "The microstructure of sputter-deposited coatings", J. Vac. Sci. Technol. A **4**, 3059 (1986).

[6] D. L. Smith, in Thin-Film Deposition: Principles and Practice, New York: McGraw-Hill, Inc., 1995, Chap. 5.

[7] S. Kubo et al, "Magnetic penetration depths in superconducting NbN films prepared by reactive dc magnetron sputtering", Appl. Phys. Lett. **44**, 258 (1984).

[8] Y. M. Shy et al, "Superconducting properties, electrical resistivities, and structure of NbN thin films", J. Appl. Phys. **44**, 5539 (1973).

[9] K. S. Keskar et al, "Superconducting transition temperatures of RF sputtered NbN films", Jpn. J. Appl. Phys. **10**, 370 (1971).

[10] M. Gurvitch, "Target erosion and deposition rates in planar magnetron sputtering", J. Vac. Sci. Technol. A **2**, 1550 (1984).

[11] H. C. Jones, "Some properties of granular thin films of high-field superconductors", Appl. Phys. Lett. **27**, 471 (1975).

[12] C. S. Jones, "Morphological, structural and mechanical properties of NbN thin films deposited by reactive magnetron sputtering", Surface and Coatings Technology **200**, 22 (2006).

[13] S. Adam et al, "Discontinuous hotspot growth related to the thermal healing length in superconducting NbN microstrips", J. Phys: Conf. Series **234**, 2 (2010).

[14] M. Ziegler et al., "Superconducting niobium nitride thin films deposited by metal organic plasma-enhanced atomic layer deposition," Supercond. Sci. Technol. **26**, 025008 (2013).

[15] S. Thakoor, J. L. Lamb, A. P. Thakoor, and S. K. Khanna, "High T_c superconducting NbN films deposited at room temperature," J. Appl. Phys. **58**, 4643 (1985).

[16] Z. Wang, A. Kawakami, Y. Uzawa, and B. Komiyamaa, "Superconducting properties and crystal structures of single-crystal niobium nitride thin films deposited at ambient substrate temperature," J. Appl. Phys. **79**, 7837 (1996).

[17] K. Ilin et al., "Ultra-thin NbN films on Si: crystalline and superconducting properties," Journal of Physics: Conference Series **97**, 012045 (2008).

[18] S. P. Chockalingam, M. Chand, J. Jesudasan, V. Tripathi, and P. Raychaudhuri, "Superconducting properties and Hall effect of epitaxial NbN thin films," Phys. Rev. B **77**, 214503 (2008).

[19] Y. V. Fominov and M. V. Feigel'man, "Superconductive properties of thin dirty superconductor–normal-metal bilayers," Phys. Rev. B **63**, 094518 (2001).

CHAPTER 5

NANOSTRUCTURE FABRICATION AND CHARACTERIZATION

5.1 Introduction

Several nanofabrication techniques such as EBL [1-3], ion irradiation [4, 5], local oxidation using an atomic force microscope [6], and FIB [7, 8-11] are employed to create junctions or patterned structures. Every route has its own pros and cons. For instance, FIB despite being extraordinarily flexible and straight forward approach for nanopatterning, needs overcome the issue of gallium contamination [12-14]. However, EBL comes out to be the best possible way among all the methods for nanostructure fabrication.

We report in this chapter FIB and EBL based routes for nanopatterning of NbN thin films. Although, the superconducting property is largely suppressed by the gallium ion implantation comparison to samples patterned using the standard EBL technique, the moderate Tc of about 6K clearly shows potential of FIB technique for patterning of superconducting films.

The conventional four point probe method was used to evaluate superconducting properties of the nanostructures in a customized variable temperature liquid nitrogen shielded liquid helium cryostat down to 1.8K.

5.2 Overview of fabrication using electron beam lithography (EBL)

Process flow for nanofabrication using EBL route is shown in Fig.5.1. A set of experimental conditions for routinely fabricating high-resolution nanostructures is developed after several test runs on 10nm thick and 5mm x 5mm area NbN films on Si/SiO_2. The 10μm x 10μm pattern area of the NbN film consists of meander structure with 100nm-wide wires and 50% filling factor. EBL was performed in Raith e-line lithography system.

The nanostructure fabrication was performed using EBL facility of Tata Institute of Fundamental Research (TIFR), Mumbai once and then using the facility of Indian institute of technology (IIT), Mumbai. Reactive ion etching (RIE) was performed in TIFR in both the cases.

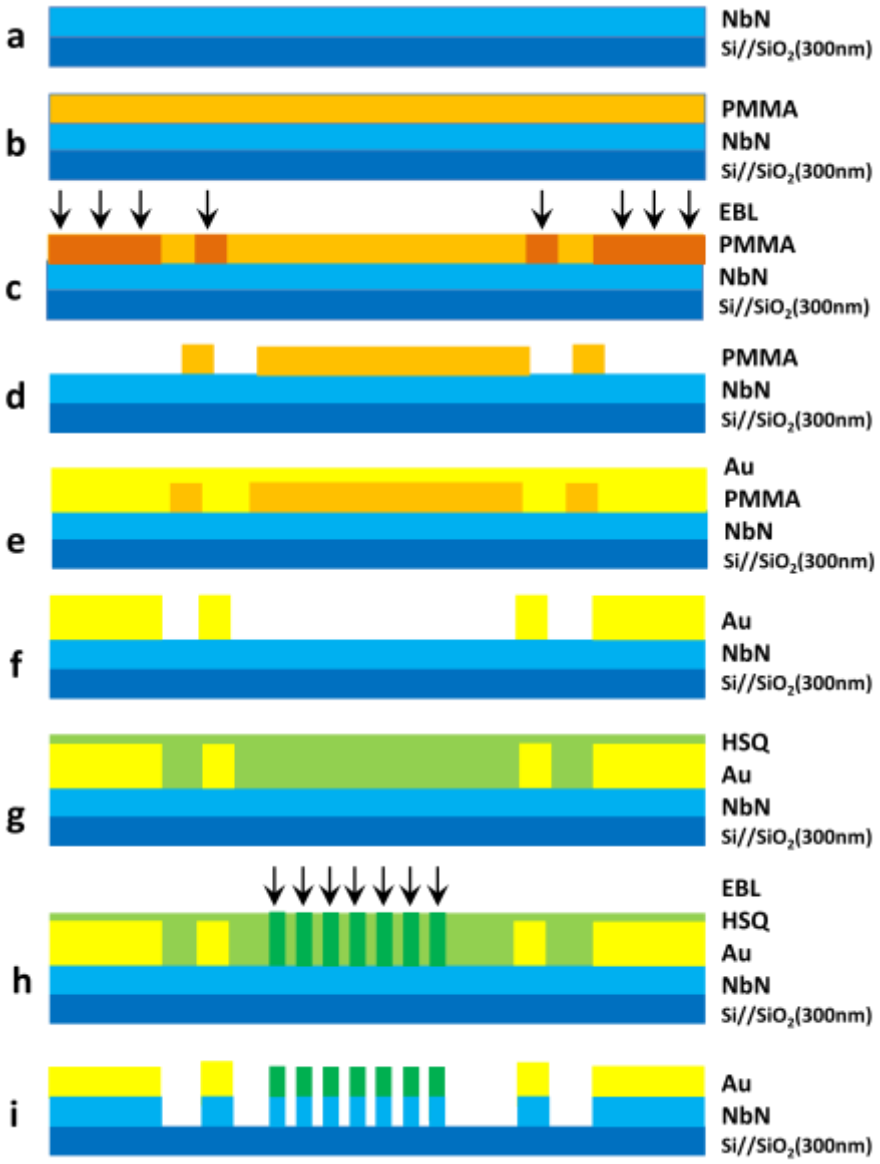

Fig.5.1: Overview of the fabrication process for nanostructure fabrication of NbN on Si//SiO_2 (300nm) substrate for its application as SNSPDs. (a) Deposition of NbN on Si//SiO_2 substrate (b) Spin coating of PMMA on thin film (c) EBL for fabrication of contact pads and markers (d) Development of PMMA (e-beam resist) (e) Thermal deposition of Cr/ Au (f) Lift off to remove Au from undesired places of thin film (g) Spin coating of HSQ (h) EBL for fabrication of nanostructure (i) Development of HSQ and RIE to remove NbN from undesired places.

The detailed process flow of nanowire fabrication is described below with the screening method used to choose the better device. The defects are not always obvious in SEM images and hence electrical measurements are to be performed for confirmation of usable devices. Poly methyl methacrylate (PMMA) is spin coated on the NbN film. EBL technique is used for making contact pads as well as the alignment markers for the second level of lithography for nanopatterning. Thermal deposition of Cr/Au and subsequent development of for contact pads is followed by spin coating of hydrogen silsesquioxane (HSQ). EBL is carried out as the next step for writing of nanopattern. Reactive ion etching (RIE) is performed to remove NbN from rest of the places except the nanowires covered with HSQ. Here it is required to mention that for fabrication of 100nm wide nanowires with 200nm pitch in 100μm^2 area in the form of meander structure the nearby area may also get exposed to electron beam due to proximity effect. The proximity effect depends mainly on the scattering of electrons emitted during EBL which generate many more secondary electrons in the e-beam resist and substrate of the film making the exposed area wider than the beam width. The higher accelerating voltage reduces the side scattering of electrons in the film and hence reduces the proximity effect. At the same time the higher limit is controlled by energy of electrons.

If the energy of electrons is too high (>30kV) it may damage the thin film. 15-20kV accelerating voltage is chosen for fabrication of nanostructure to avoid proximity effect and at the same time to avoid damage of the film.

To have uniform critical current the variation in width (< ±5%) of nanowires in an area of 10μmx10μm is a critical requirement for its application as single photon detector. Careful selection of EBL parameters and verification through high resolution microscopy and low temperature transport measurements is therefore must. Uniformity of edges is determined by the stability of beam current and proper placing of the stage/ alignment of the electron beam. High precision electron focusing and high precision stage control contribute a lot to uniformity of edges. The electron beam dose during writing these nanowires in meander structure is also very important factor which also ensures uniform edges without any constriction.

5.3 Procedure and process parameter optimization

About 50 NbN thin films on 5x5 mm^2 wafer are used for the optimization of process parameters for nano fabrication both at IITB and TIFR, Mumbai. A schematic of a typical structure is seen in Fig.5.2.

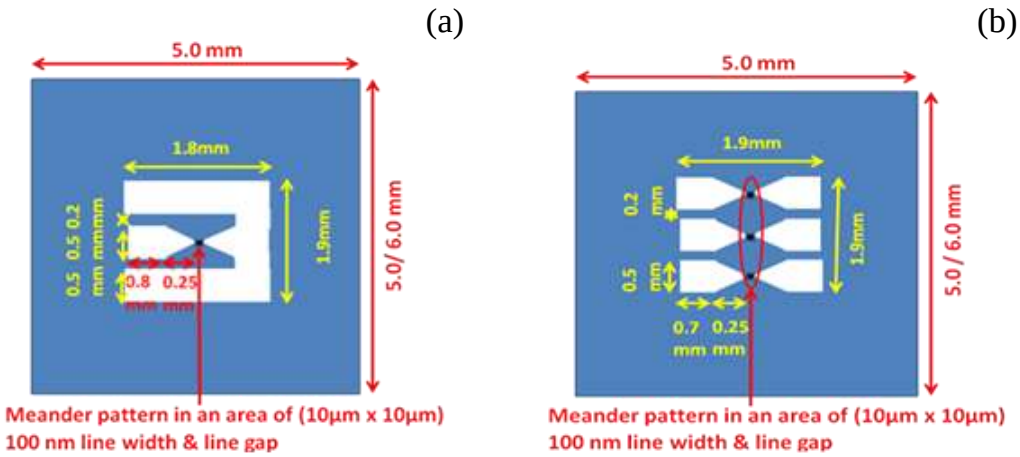

Fig.5.2: Schematic of typical NbN patterns (a) with and (b) without coplanar waveguide structure.

The design of the device in Autocad is an important step as the dimensional parameters chosen plays important role during fabrication. The geometry of the device with dimensions can be seen in the Fig.5.3.

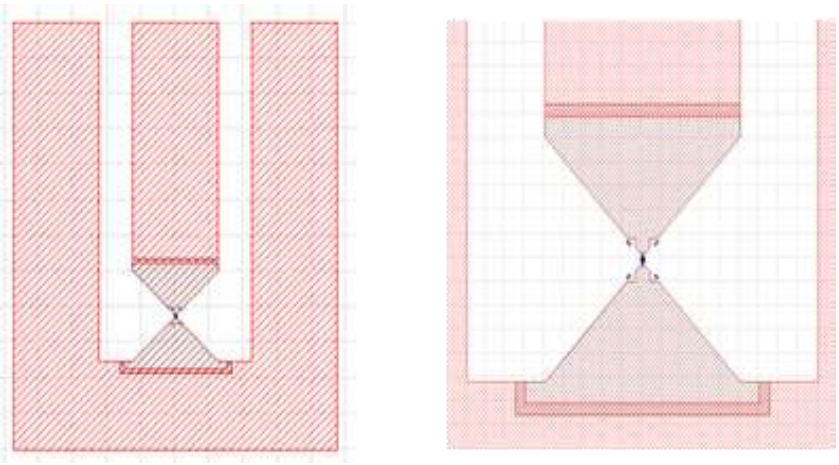

Fig.5.3: Autocad drawing of nanostructure along with contact pads in the form of coplanar waveguide.

Although as shown in the Fig.5.4, the bend present in the autocad drawing of meander structure between two nanowires is 180 degree, however after EBL the tight bends seem to become less sharp. The effect of tight bends on detection efficiency and dark count rate is required to be considered while designing selecting dimensions of the nanostructure in the device.

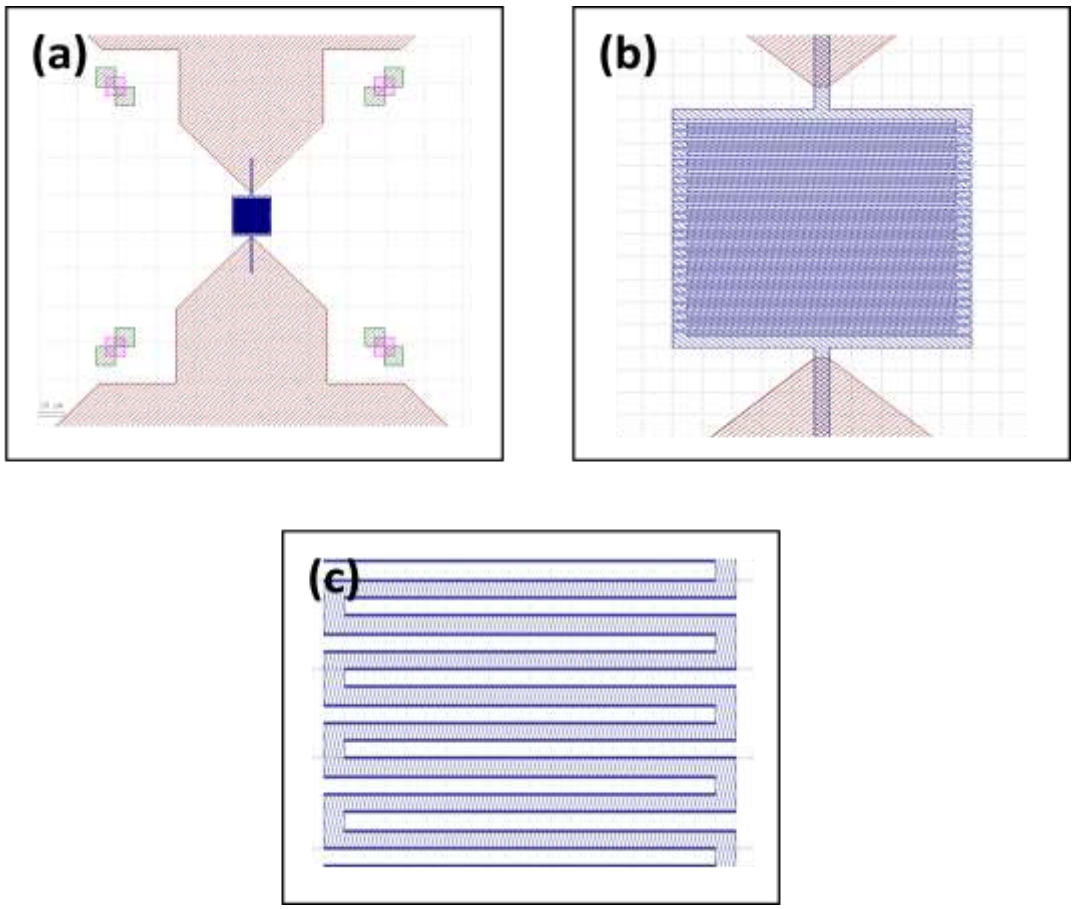

Fig.5.4: Autocad drawing of (a) tip of conical pad, markers and nanostructure (b) image after zooming the nanostructure (c) zoomed nanowires.

5.3.1 Optimization of the nanostructure at IITB

5.3.1.1 Contact pads and markers

The optimized recipe for fabrication of contact pads and markers for second level lithography followed at IITB is given below.

(1) Spin coating

(a) Co-polymer EL9 at 3200rpm for 60 seconds with an acceleration of 1600rpm followed by baking at 180^{o}C for 7 minutes.

(b) Microchem PMMA950A2 (4%) at 2000rpm for 45 seconds with an acceleration of 1000rpm followed by baking at 180^{o}C for 2 minutes.

(2) Electron beam lithography

The contact pads were defined in two parts in order to optimize the machine time. While large aperture was selected for broad rectangular part of the pad to increase the beam current, for cone shaped section of the pad close to the meander a moderate beam current was maintained for defining sharper edge. The marker due to their micron size was made with a relative small beam current. The details of the relevant EBL parameters are summarizes in Table.5.1

Table.5.1: EBL parameters for contact pads and marker optimized at IITB:

S. No.	Structure type	EHT (kV)	Write Field (µm)	Current (pA)	Aperture (µm)	Dose (µC/cm^2)	Time (minute)
1.	Marker	20	2000	149	20	200	2
2.	Fine pads	20	2000	1290	60	180	38
3.	Broad pads	20	2000	5240	120	170	31

(3) Pattern developing

Immediately after electron beam writing patterns were developed in MIBK: IPA (1:3) for 60-65 seconds. Isopropyl alcohol (IPA) was used thereafter as a stopper for 25-30 seconds.

(4) Fabrication of contact pads and marker

5nm of Cr was deposited using standard thermal evaporation technique which was followed by deposition of 80nm of Au. Lastly, the lift-off was done in acetone for 30 minutes. The optical images of the contact pads and markers are shown in Fig.5.5.

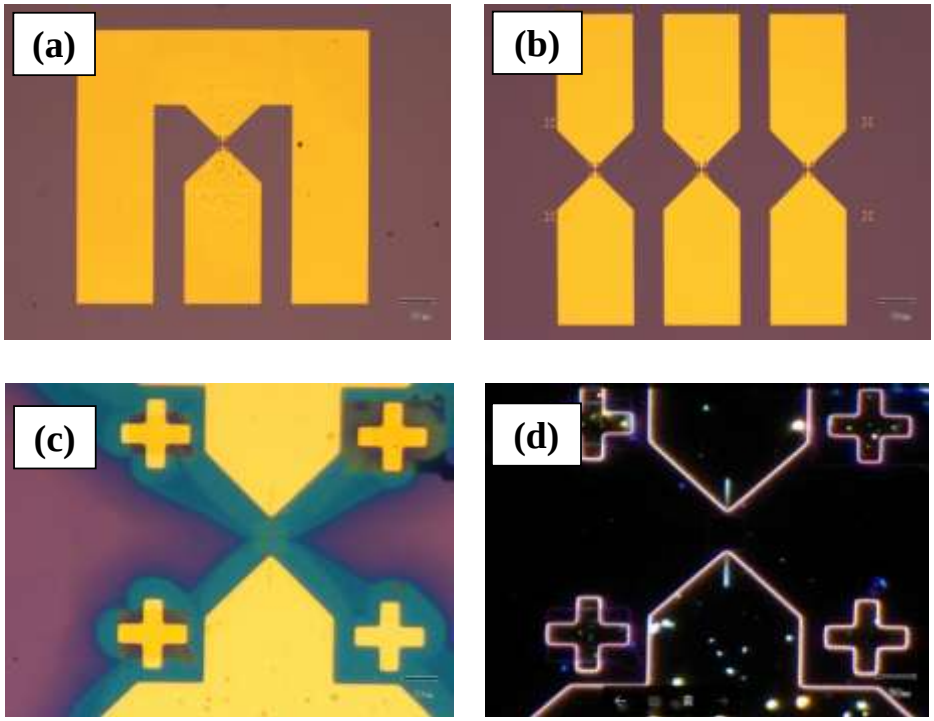

Fig.5.5: Optical images of contact pads and markers fabricated using EBL. (a-c) normal view (d) dark field image.

5.3.1.2 Meander pattern

Beam current which very much dependent of aperture turns out to be crucial in defining well separated meander lines. Judicious choice of write field seems to play an important role as well. A set of optimization was carried out on three different beam current as listed in Table.5.2. The dose was varied from 140 to 200μC/cm^2. The 'nanostructure-a' while failed to make any meander patterns 'nanostructure-b' and 'nanostructure-c' with much lower aperture and beam current shown reasonably good patterns within a particular dose range.

Table.5.2: List of trials for optimization of nanostructures at IITB

S. No.	Structure type	EHT (kV)	Write Field (μm)	Current (pA)	Aperture (μm)	Dose (μC/cm^2)
1.	Nanostructure - a	20	50	1272	60	140 - 200
2.	Nanostructure - b	20	25	35.95	10	140 - 200
3.	Nanostructure - c	20	25	19.45	7.5	140 - 200

A further optimization of process parameters was done by varying the development time. The development was performed in 25% TMAH. Four sets of sample were prepared and listed in Table.5.3. EBL for all the samples were done at 20kV EHT and with 25µm write field. Although there is no systematic dependence, however the dose range for best patterns shifts with development time for any particular beam current.

Table.5.3: Further trials for optimization of nanostructure at IITB

S. No.	Structure type	Current (pA)	Aperture (µm)	Develop Time (sec)	Dose (µC/cm^2)	Optimized Dose (µC/cm^2)
1.	Nanostructure -1	19.45	7.5	3	140-200	170-190
2.	Nanostructure -2	35.95	10	3	140-200	170-190
3.	Nanostructure -3	19.45	7.5	6	140-200	150-160
4.	Nanostructure -4	35.95	10	6	140-200	180-190

The SEM images shown in Fig.5.6 are the result of 'Nanostructure -2' with different doses.

(1) Nanostructure -2: Dose 170µC/cm^2

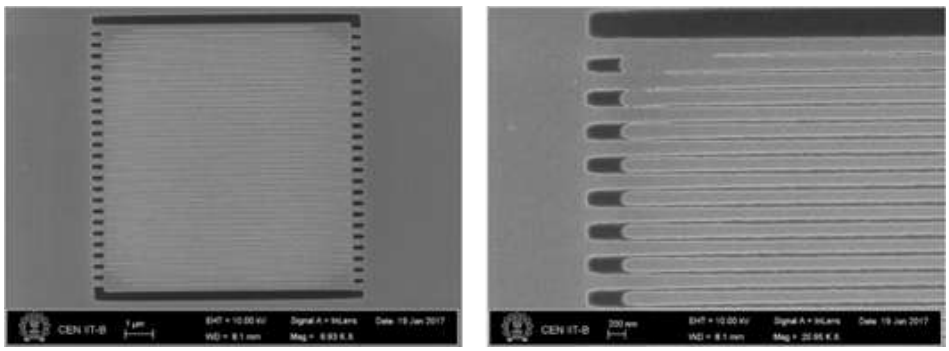

(2) Nanostructure -2: Dose 180µC/cm^2

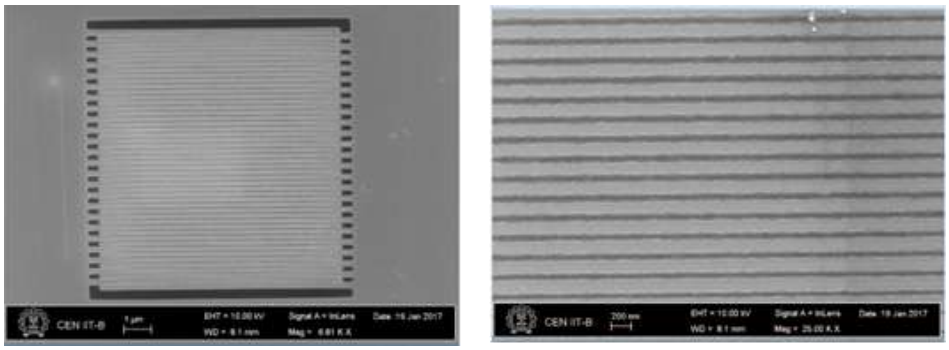

(3) Nanostructure -2: Dose 190µC/cm^2

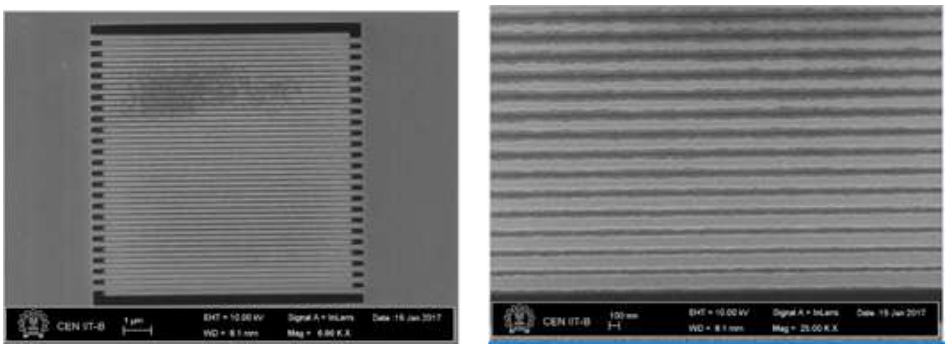

Fig.5.6: SEM images of nanostructure fabrication using EBL while optimizing the process parameters by varying dose and keeping development time (3second) and rest of the parameters same (a) Dose 170µC/cm^2 (b) Dose 180µC/cm^2 (c) Dose 190µC/cm^2.

5.3.1.3 Uniformity of edges

Variation in the width of edges mainly depends on the stability of the beam current, sample stage, high precision electron focussing and optimization of process parameters. Optimized parameters with dose 180µC/cm^2, development time 3seconds and aperture size 7.5µm were found to have better edge uniformity as is seen in the Fig.5.7.

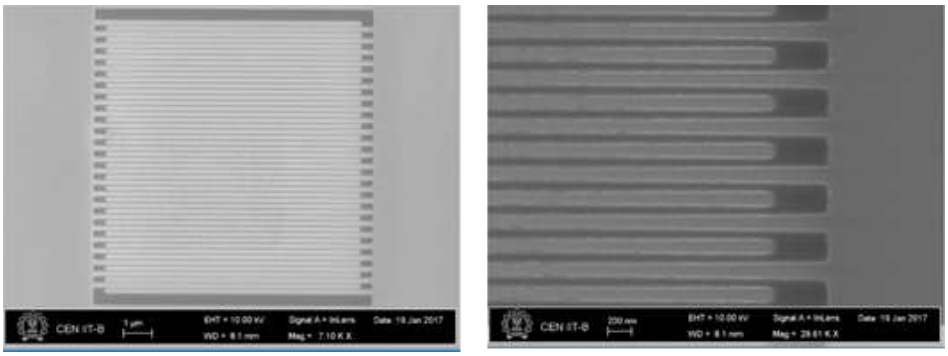

Fig.5.7: SEM image of nanostructure fabricated using EBL technique with Dose 180µC/cm^2, development time 3second and aperture size 7.5µm.

5.3.2 Optimization of the nanostructure at TIFR

Several set of recipes were tried for the fabrication of meander lines at a higher dose and lower EHT. SEM images of two important set of samples with marked improvement are presented in Fig.5.8 and Fig.5.9 with varying doses from 1200 to

1700μC/cm^2. In Fig.5.8 SEM images are for set of samples for which the spin coating of HSQ was done at 3000rpm. For the second set other than the spin speed of 5000rpm rest of the parameters were kept unchanged.

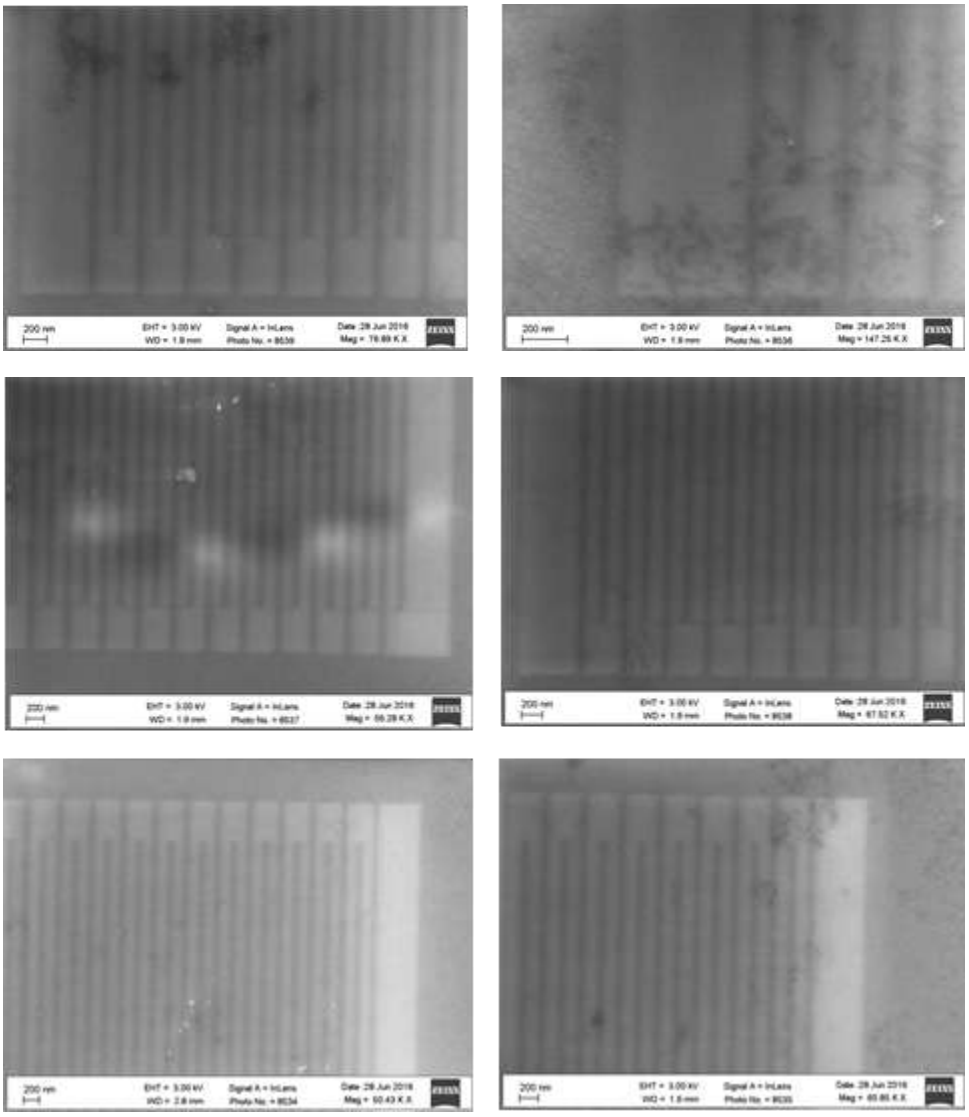

Fig.5.8: SEM images of meander lines at 3000rpm spin speed of HSQ coating. Variation in doses from 1200 μC/cm^2 to 1700 μC/cm^2.

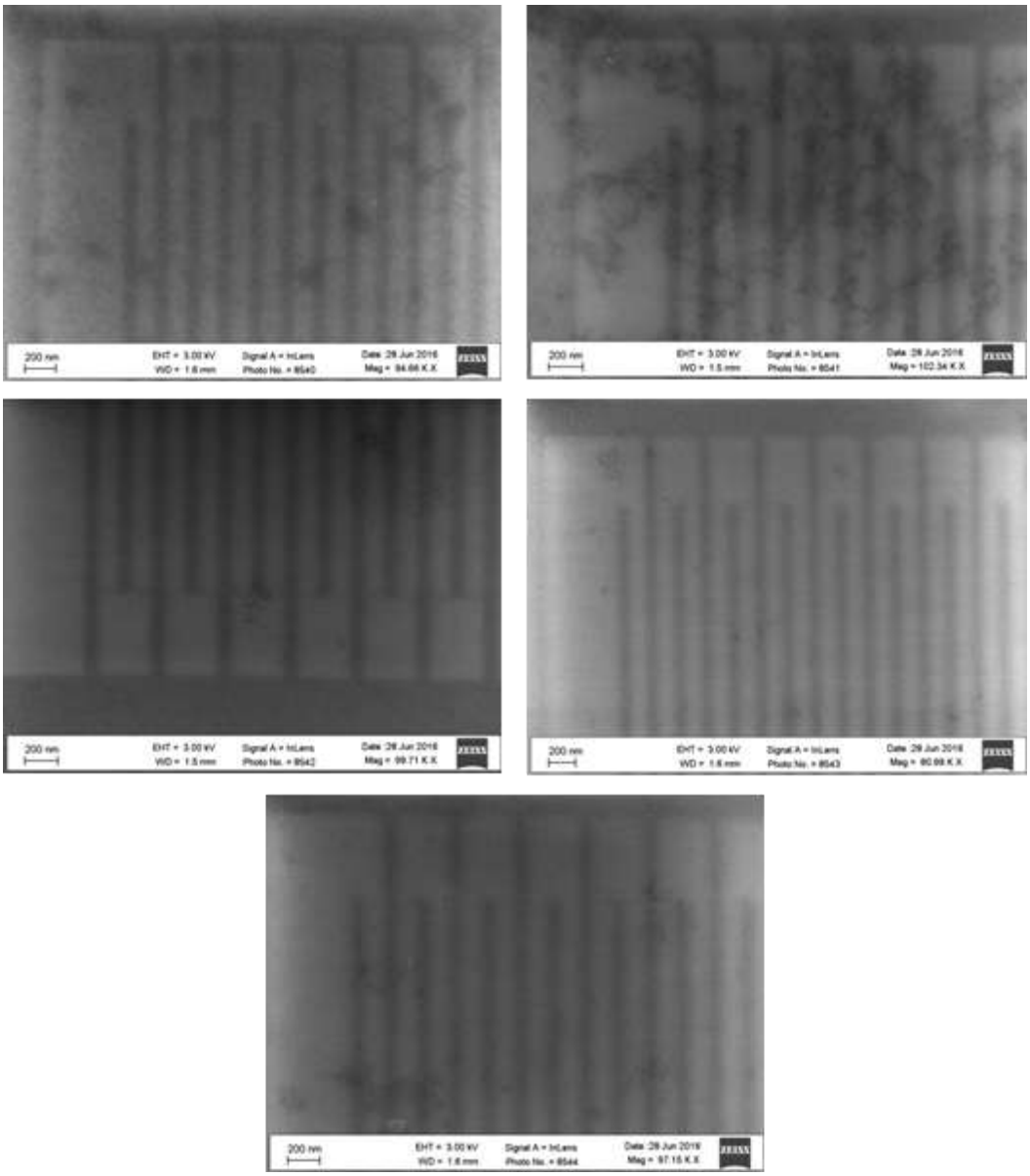

Fig.5.9: SEM images of meander lines at 5000rpm spin speed of HSQ coating. Variation in doses from 1200 µC/cm^2 to 1700 µC/cm^2.

A typical SEM image of NbN nanowires in the shape of meander structure within an area of 100µm^2 is shown in the Fig.5.10. The final recipe for the whole device structure is mentioned in the table.5.4.

Table.5.4: Optimized recipe of NbN nanolines in meander structure using EBL at TIFR

S. No	Structure type	E-beam resist	Voltage (kV)	Dose ($\mu C/cm^2$)	Write field (μm)	Aperture (μm)	Current (pA)
1.	Au pads	EL9 and PMMA 950 A2 (+ve resist)	15kV	180	2500	120μm	4229
2.	Au pads fine/ markers	EL9 and PMMA 950 A2 (+ve resist)	15kV	180μC/cm^2	100	30μm	244
3.	Nanowire in meander shape	HSQ(6%)(-ve resist)	15kV	1500μC/cm^2	100	30μm	132

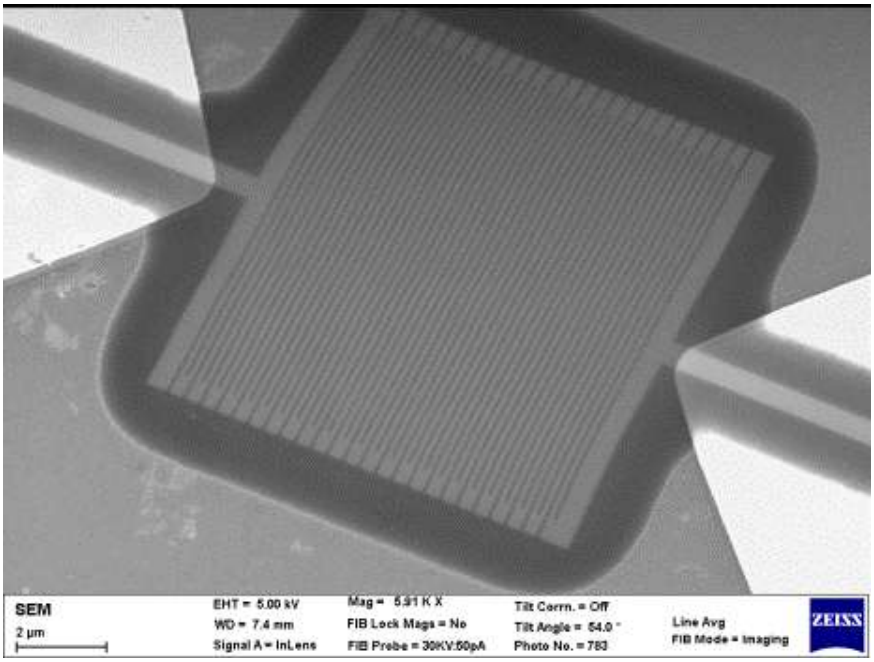

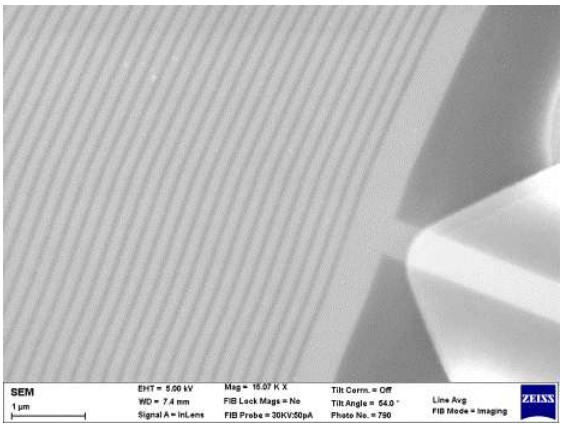

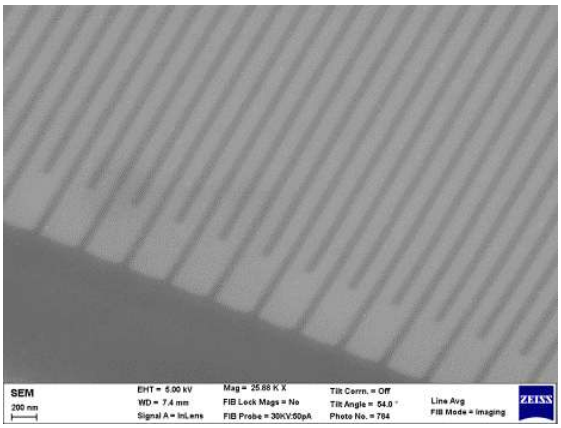

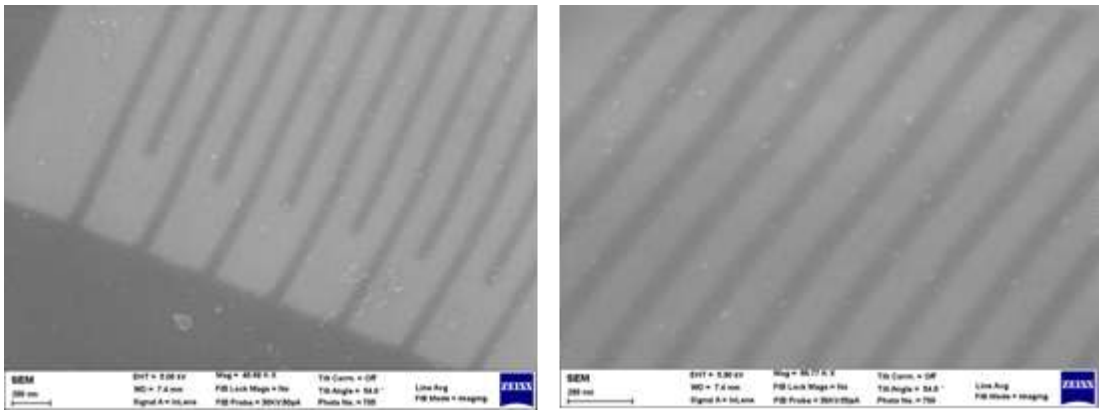

Fig.5.10: SEM images of a NbN nanostructure on Si//SiO_2 with line width of 100nm.

5.4 Focused ion beam lithography (FIB)

Achieving a small cross-section along with no degradation of the superconducting properties is vital particularly in the case of employing focused ion beam milling (FIB) technique for nanopatterning. Nevertheless, the Zhang et al. [10] were successful in fabricating high quality superconducting nanowires from ultrathin MgB_2 films by FIB. Bachar et al. [11] demonstrated FIB based design of a superconducting nanowire single photon detector on a core of a single mode optical fibre. Protective layer such as aluminium or gold are used in some cases to prevent degradation due to gallium irradiation during FIB milling [15-16].

Effort has been made to optimize the nano fabrication parameters via successive iterations of "design-observation-refabrication".

5.4.1 Elemental analysis

Elemental analysis was carried out using energy dispersive spectroscopy (EDS) measurements and shown in the Fig.5.11 and Fig.5.12, EDS plot as shown in the Fig.5.11 while confirms that the NbN has been removed completely from the exposed area however there is a significant amount of gallium implantation during milling. The quantitative analysis as shown in the figures shows only the presence of gallium, silicon and oxygen. Silicon and oxygen weight percentage are due to the presence of substrate. 25% (atomic) gallium contamination can be estimated from the analysis

which is significant. EDS measurements from the remaining portion of NbN which was not exposed to the gallium ion imaging or milling does not show any sign of gallium deposition (Fig.5.12).

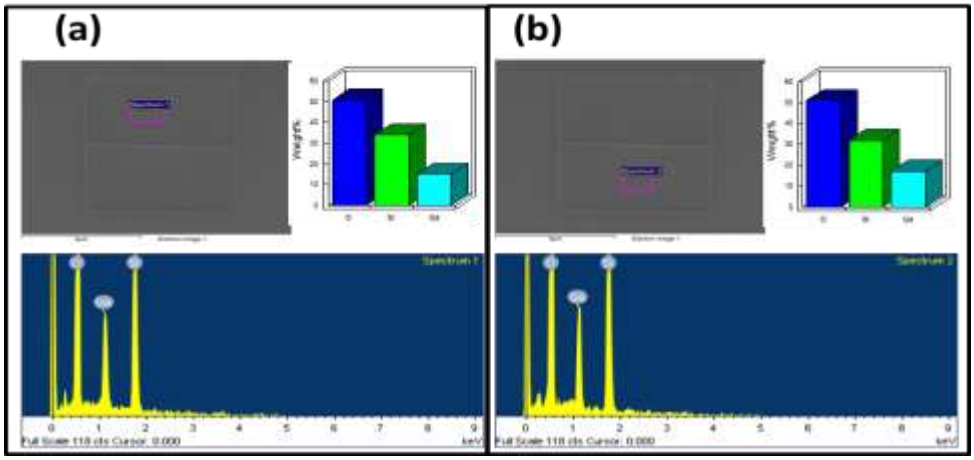

Fig.5.11: Panel (a) and (b) show EDS analysis for the heavily milled areas.

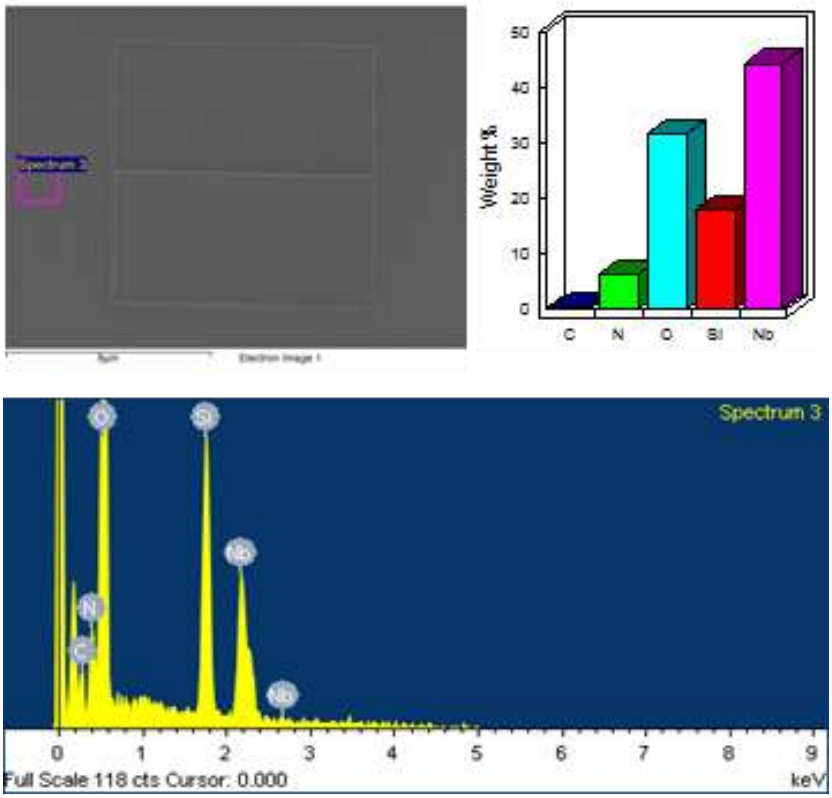

Fig.5.12: EDS analysis of unexposed area around the FIB milling.

5.4.2 Fabrication of single nanowire

FIB milling was performed in a Auriga, Zeiss dual beam system with an accelerating voltage of 30 kV. 25µm-wide thin (~10nm) NbN microstrips in four-probe measurement configuration were deposited using shadow mask. In order to avoid edge non-uniformity especially design bi-level mask made out of 75µm thick hard electroformed nickel plate with second level stepped back from the ~25µm thick with ultra sharp edge profiles was used. The bridges were thinned down to different widths along the length. Shown in Fig.5.13 are SEM images of 100nm, 200nm, 500nm, 1000nm wide lines for a length of 100µm. A very low ion beam current ~50pA was used. The idea behind making of bridges of different widths was initially to optimize the FIB process parameters. The effect of Ga ion contamination on superconducting properties as the wire width reduces is a definite research direction for future.

5.4.3 Fabrication of meander structure

The narrow junctions of NbN films were at first localized by using FESEM. The electron and gallium ion beams were aligned at the same point and utmost care was taken not to expose these junctions for the gallium ion imaging. The 25µm-wide bridge thinned down to 10µm for a length of 10µm. It makes even narrower panel of 10µm x10µm in 25µm x 250µm bridge.

Meander structure of 100nm wide nanowire and 200nm pitch were fabricated in this panel as shown in Fig.5.14. The milling pattern of meander lines was optimized and same milling parameters and conditions were used to obtain the required pattern at very low ion beam current ~ 50pA.

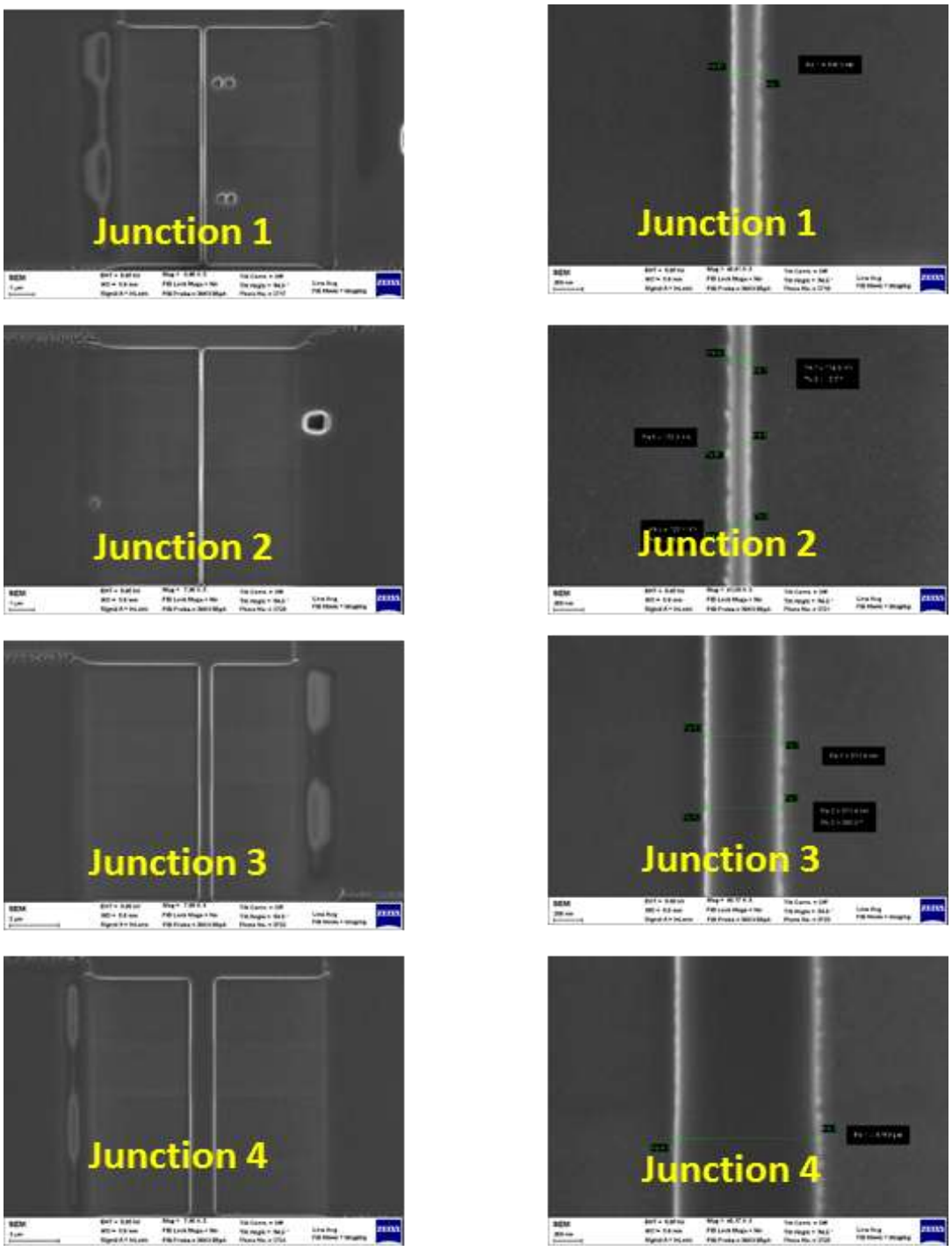

Fig.5.13: Nanowires of widths (a) 100nm, (b) 200nm, (c) 500nm and (d) 1000nm and length 100µm.

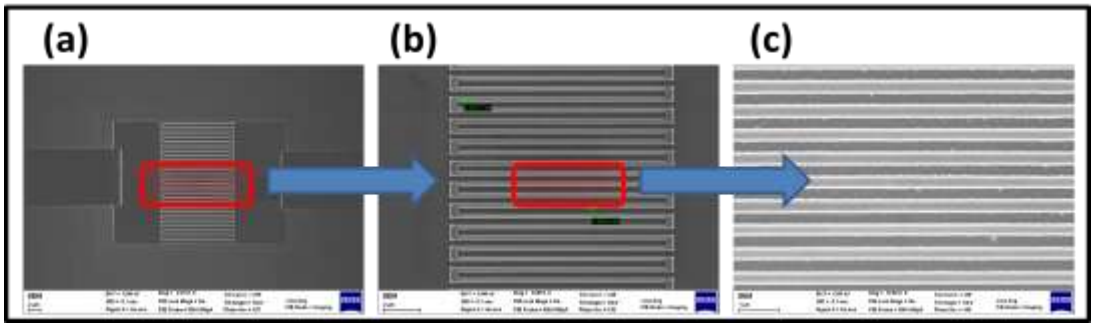

Fig.5.14: Meander pattern fabricated in a panel of 10µmx10µm area out cut in between 25µmx250µm bridge.

The sample then undergoes a second lithography step, in which the narrow junction strip of NbN was further milled at higher ion beam current ~ 240pA (panel a) to remove extra NbN from the edges of the pattern area and thereby ensure presence of only meander line connection between the contact pads for transport measurements.

5.5 Electrical characterization of superconducting meander lines

Superconducting nanostructures are studied for its transport properties towards the feasibility of its application in single photon detection. Superconducting transition temperature (Tc) and transition width (ΔTc) in thin film samples are the important factors for its further processing in making of nanostructures. Nanostructures are thoroughly examined using SEM as a first step prior to transport measurements at low temperature. Cr/Au layers were deposited afterwards using thermal evaporation. 25µm dia. aluminum wire was employed for connecting the pads with chip carrier using wire bonder as shown in Fig.5.15.

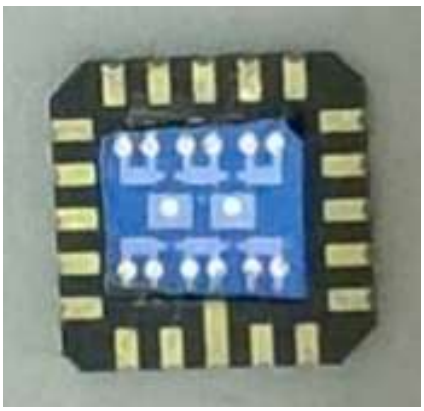

Fig.5.15: Sample mounted on a chip carrier for transport measurements.

5.5.1 Resistance versus temperature (RT) measurements

5.5.1.1 RT measurement of EBL fabricated samples

A typical RT curve of the sample after nanostructure fabrication (in TIFR) is shown in Fig.5.16. Tc is considered as the temperature where resistance of the sample is half of that in normal state and ΔTc is taken as the temperature window where resistance drops from 90% to10% of its normal state value. Tc foe the sample is ~8K and ΔT is ~1K. This is acceptable for the next level of investigation towards its feasibility for photon detection.

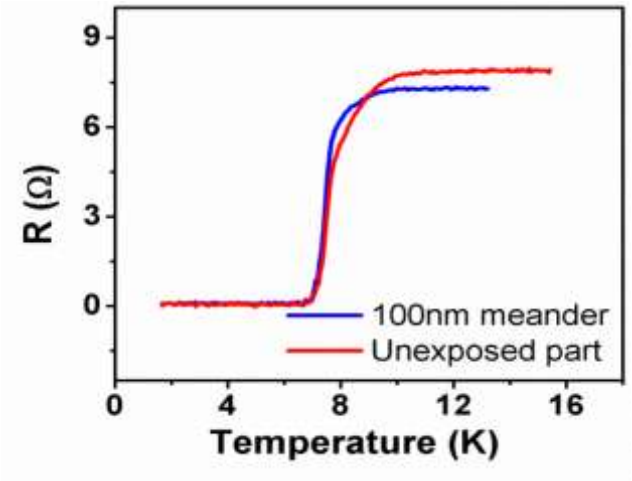

Fig.5.16: Comparison of resistance vs temperature plot of nanowires fabricated using EBL and RIE with 10nm thick pristine NbN thin films. Measurements were carried out both during heating and cooling cycles with a temperature sweeping rate of 0.5K/min.

The drawback in this case is that the resistance of the sample is quite low even after the nanostructure fabrication. An RT measurement of unexposed part is compared in the figure. In principle, the resistance of the patterned area should increase by two to three orders of magnitude after patterning. However, it is found that the resistance in both the cases has almost same value. Incomplete removal of NbN from the uncovered portion of the pattern area during reactive ion etching process is likely be the cause of such discrepancy. However, it is important to note that the temperature corresponding to zero resistance and the superconducting transition width is same in both cases, which confirms that processes involved in EBL do not alter the superconducting properties.

5.5.1.2 RT measurement of FIB fabricated samples

It can be seen from the Fig.5.17 that the Tc of the unpatterned film is ~15.5K with ΔT ~ 1K, and normal state resistance at 20K is 2.5kΩ. The resistive transition of FIB patterned nanostructures is compared with the unpatterned 25µm NbN strip in the figure. The measurements were carried out on meander patterns with 100 and 200nm line width and 50% filling factor over 10µm x 20µm area. Microstrip as well as nanopatterns were made on the same chip in order to avoid run to run variation of superconducting properties. Tc decreases upon nanopatterning due to gallium ion exposure and decreases further as the width of nanolines reduced to 100nm. It is important to note here the presence of residual resistance in R(T) curves even at T= 2K. Influence of gallium implantation during FIB on superconductivity of Nb microstrip was studied in details by Datesman et al. [12]. Although they observed a trend of decreasing Tc and increasing onset resistance with increasing gallium dose; all the samples however showed complete superconducting transition. The residual resistance after ion milling was observed by Litombe et al. on high Tc-cuprates [15]. Refinement of lithographic processes resulted in complete superconducting transitions in nanowires down to 80nm wide and 20nm thick optimally doped LSCO films.

We believe that the residual resistance in our case is caused due to nucleation of gallium ion mediated non-superconducting regime along the cross section of the nanowires randomly at certain places. Lateral gallium contamination due to highly focused ion beam in silicon in vicinity of the processed area was observed earlier [13]. The cause of lateral implantation is believed to be due to redepostion of sputtered gallium ions. Mayer et al. [17] have also reported the formation of amorphous layer in a sidewall of silicon due to gallium ions. With FIB milling using gallium ion at an 88 deg. incident angle, and 30keVenergy they have observed that the damage in side wall can extend up to 22nm in silicon. Mayer et al. argued that the result of gallium implantation may range from complete amorphization, as in the case of semiconductor materials, to the formation of defect agglomerates and even intermetallic phases, in the case of certain metals.

The meander pattern used in this study has 50% filling factor and the patterned area is same in both the cases, reducing the width by a factor of half essentially doubles the

length of the nanowire while decreases the cross section by a factor of half. Assuming simple ohmic behavior this in turns estimates the residual sheet resistance of pattern with 100nm wide line is higher by a factor of five of that for patterns with 200nm wide line. However, our measurement shows that the residual resistance is increased almost by one order of magnitude (from ~ 1kΩ to 10kΩ) while decreasing the width of the line [18]. This discrepancy can be understood qualitatively if we assume that the residual resistance observed in our samples is due to gallium ion implantation and that it is directly proportional to the dose of implanted gallium ion. Since the ion beam exposure time for the pattern with 100nm wide line is two times larger than that for the pattern with 200nm wide line, it is obvious that the residual resistance of former pattern will be higher than the estimated value.

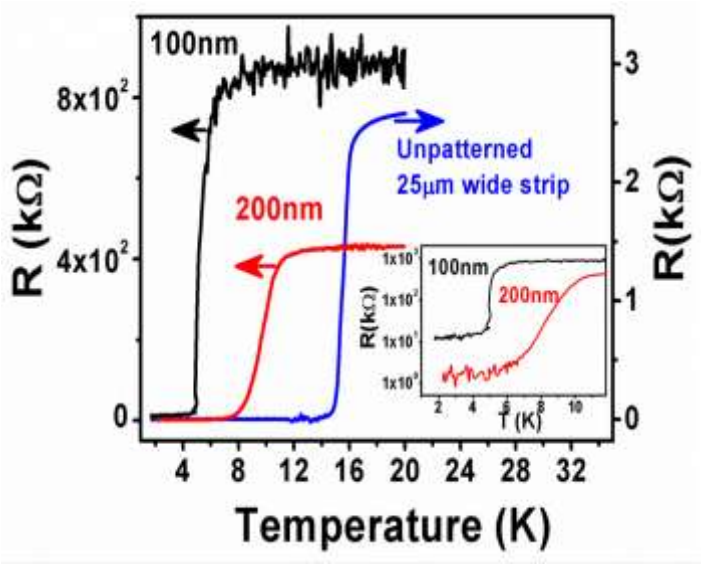

Fig.5.17: Resistance vs temperature plots of as-deposited NbN microstrip and NbN nanowires fabricated using FIB technique. FIB milled samples show non-zero resistive transition and reduction in superconducting transition temperature. Inset zooms in the low temperature behavior of nanowires.

5.5.2 Current versus voltage (IV) measurements

The voltage across the device remains zero in its superconducting state and current flows without any dissipation. This can be maintained only if the operating temperature of the device is less than the critical temperature and also the current flowing through the device at this temperature is less than the critical current (Ic). The

critical current depends on the material properties and geometry of the device. In ideal condition the intermediate state between the zero resistance state and the normal state is not stable. The IV characterization of the device is explained below for EBL fabricated nanostructure, FIB fabricated nanostructure and micron size structure fabricated by the use of shadow mask during DC magnetron sputtering of the thin film sample.

5.5.2.1 IV measurement FIB fabricated samples

IV characteristics of microstrip and nanopatterns are shown in Fig.5.18. IV curve of microstrip measured at 2K shown in panel A is hysteretic and shows a sharp jump from superconducting to normal state [19-21]. The current at which this jump took place is found out to be 1.5mA. The strip returns to superconducting state while reversing the applied voltage when the equilibrium between the Joule heating and energy dissipation in to the substrate by the phonons in the film is achieved at a particular current. Panel B shows that as the operating temperature increases the transition from superconducting state to normal state becomes less sharp and also critical current reduces. The difference in values of critical current and return current is quite visible at 2K whereas both values start merging at higher temperature. IV for both the patterns as can be seen in panel C is non-linear. Although it is not possible to deduce Ic from the measurements owing to incomplete superconducting transition, qualitatively it can be argued from the shape of the curve that the Ic must be low as compared to the devices with similar dimensions. Panel C also compares the IV curve of 200nm wide line pattern measured at two different temperatures (2K and 5K). The shape of the non-linear IV plot measured at 5K is similar to 2K data of 100nm wide line pattern, and does not have any hysteretic nature. IV curve for patterns with 200nm wide line measured at 2K, in particular is however interesting. It shows some hysteretic behaviour at higher current. The step like behaviour although not prominent, is typically associated with phase slip process. Incomplete superconducting transitions and the steps in IV were reported previously [22, 23]. Dissipation and/or fluctuations due generation of phase slip centres in the case of one

dimensional superconducting structures or vortex antivortex pair generation in two dimensional systems leads to destruction of long range order parameter. Although the nanowires in our case are much wider than the coherence length (typically 4-5nm in NbN) presence of local constrictions and/or inhomogeneities associated with FIB milling as mentioned previously cannot be ruled out.

The transport data are useful for derivation of many physical parameters of superconducting samples. Some of the parameters of NbN nanostructures which are useful for device applications are estimated and shown in Table.5.2.

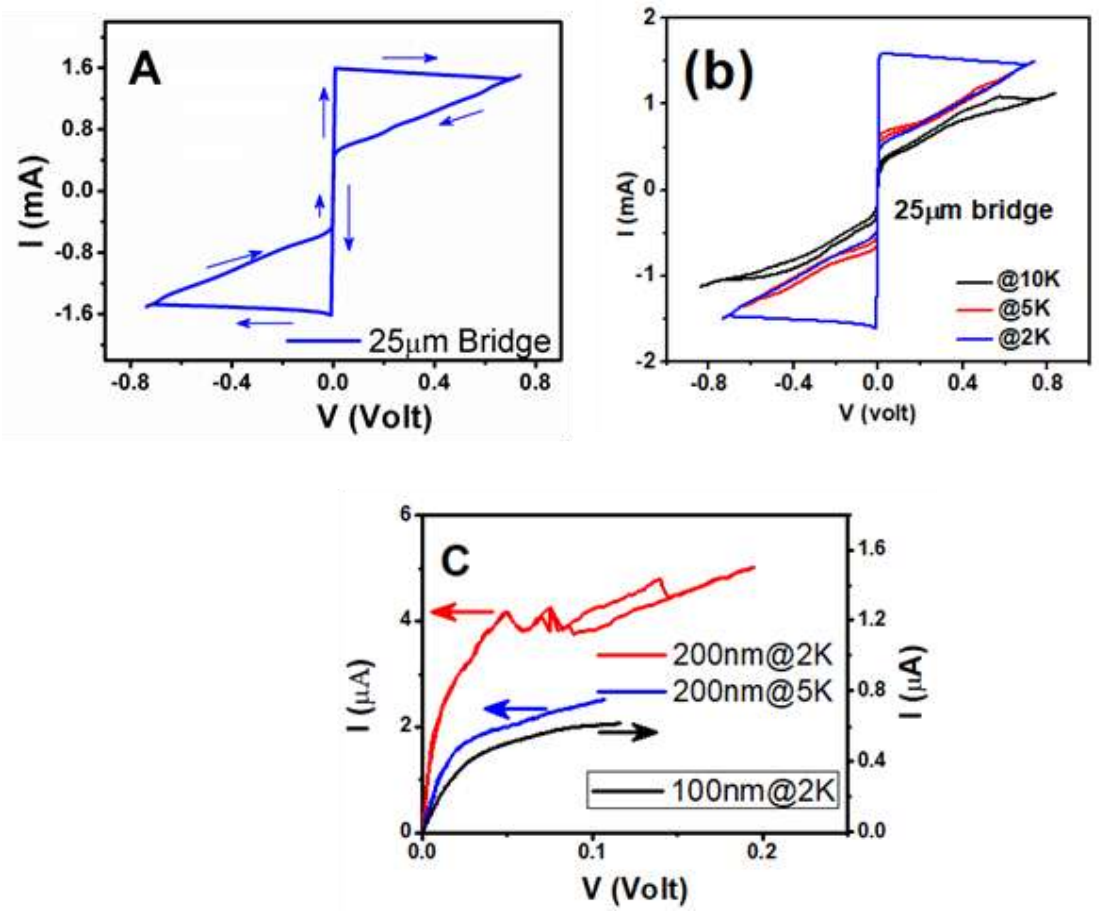

Fig.5.18: Current-voltage characteristics of NbN. Panel A plots I-V data of as-deposited NbN microstrips. Panel B plots IV data of as-deposited NbN microstrips measured at 2K, 5K and 10K. Panel C compares IV measurements of 100 and 200nm wide meander lines fabricated using FIB milling. The non-linear and non-hysteretic behavior evolves into a step like behavior particularly at higher bias voltage when measurement temperature decreases from 5K to 2K for 200nm wide line meanders.

Table.5.5: Experimentally observed and calculated parameters of superconducting nanostructure

S. No	Parameters	100nm wide meander	200nm wide meander
1.	Film thickness	10nm	10nm
2.	Nanowire width	100nm	200nm
3.	Pitch / fill factor	200nm / 50%	400nm / 50%
4.	Area / length	10µmx10µm / 500µm	10µmx10µm /250µm
5.	Critical temperature [Tc]	5K	8.5K
6.	Transition width [ΔTc]	1.5K	2.5K
7.	Energy gap [Δ (T=0)]	1.2meV	1.9meV
8.	Magnetic penetration depth [λ (T=0)]	512.5nm	543.0nm

5.6 Summary

The objective of nanostructure fabrication using NbN thin film samples was due to research interest towards fundamental physics of photon absorption and energy relaxation in NbN. The study is performed in order to develop patterning procedures which allow fabrication of high quality devices. The technical hurdles associated with fabrication to create these nanostructures are explored. This while may have technological ramification for novel device architectures, provide some interesting manifestation of intrinsic low dimensional superconducting properties.

5.7 References

[1] S Dorenbos, "Fabrication and characterization of superconducting detectors for single photon counting', Delft University of Technology, Master thesis (2007).

[2] S. Miki et al., "Large sensitive-area NbN nanowire superconducting single-photon detectors fabricated on single-crystal MgO substrates", Appl. Phys. Lett. **92**, 061116 (2008).

[3] A. Korneev, "Recent nanowire superconducting single-photon detector optimization for practical applications", IEEE Trans. Appl. Supercond. **23**, 2201204 (2013)

[4] N. Bergeal et al, "High Tc superconducting quantum interference devices made by ion irradiation", Appl. Phys.Lett. **89**, 112515 (2006).

[5] N. Bergeal, X. Grison, J. Lesueur, G. Faini, M. Aprili, and J. -P.Contour, "High Tc superconducting quantum interference devices made by ion irradiation", Appl. Phys. Lett. **89**, 112515 (2006).

[6] C. Delacour et al., "Superconducting single photon detectors made by local oxidation with an atomic force microscope", Appl. Phys. Lett. **90**, 191116 (2007).

[7] C. Zhang et al, "Fabrication of superconducting nanowires from ultrathin MgB2 films via focused ion beam milling", AIP Advances. **5**, 027139 (2015).

[8] S. -G. Lee, S. Oh, C. S. Kang, and S. -J. Kim, "Superconducting nanobridge made from YBa2Cu3O7 film by using focused ion beam", Physica C **460**, 1468 (2007).

[9] N. Curtz et al., "Patterning of ultrathin YBCO nanowires using a new focused-ion-beam process", Supercond. Sci. Technol. **23**, 045015 (2010).

[10] C. Zhang et al., "Fabrication of superconducting nanowires from ultrathin MgB_2 films via focused ion beam milling", AIP Advances. **5**, 027139 (2015).

[11] G. Bachar, I. Baskin, O. Shtempluck, and E. Buks, "Superconducting nanowire single photon detectors on-fibre", Appl. Phys. Lett. **101**, 262601 (2012).

[12] A. M. Datesman, J. C. Schultz, T. W. Cecil, C. M. Lyons, and A. W. Lichtenberger, "Gallium ion implantation into niobium thin films using a focused-ion beam", IEEE Trans. Appl. Supercond. **15**, 3524 (2005).

[13] Charaev et al, "Enhancement of superconductivity in NbN nanowires by negative electron-beam lithography with positive resist", J. Appl. Phys. **122**, 083901 (2017).

[14] Z Wang et al, "Superconducting properties and crystal structures of single-crystal niobium nitride thin films deposited at ambient substrate temperature", J. Appl. Phys. **79**, 10 (1996).

[15] N. E. Litombe, A. T. Bollinger, J. E. Hoffman, I. Božović, "$La_{2-x}Sr_xCuO_4$ superconductor nanowire devices", Physica C **506**,169 (2014).

[16] C. Lehrer, L. Frey, S. Petersen, M. Mizutani, M. Takai, and H. Ryssel, "Defects and gallium-contamination during focused ion beam micro machining", in Proc. IEEE Ion Implantation Technol. 2000, 695 (2000).

[17] J. Mayer, L. A. Giannuzzi, T. Kamino, and J. Michael, "TEM sample preparation and FIB-induced damage", MRS Bull. **32**, 400 (2007).

[18] R. Lusche et al, "Effect of the wire width on the intrinsic detection efficiency of superconducting nanowire single-photon detectors", J. Appl. Phys. **116**, 043906 (2014).

[19] W. J. Skocpol et al, "Self-heating hotspots in superconducting thin-film microbridges", J. Appl Phys **45**, 4054 (1974).

[20] G. N. Gol'tsman et al, "Picosecond superconducting single-photon optical detector", Appl. Phys. Lett. **79**, 6 (2001).

[21] D.Yu. Vodolazov et al, "Single-Photon Detection by a Dirty Current-Carrying Superconducting Strip Based on the Kinetic-Equation Approach", Phys. Rev. Appl. **7**, 034014 (2017).

[22] A. K. Elmurodov et al., "Phase-slip phenomena in NbN superconducting nanowires with leads," Phys. Rev B **78**, 214519 (2008).

[23] C. Delacour, B. Pannetier, J. - C. Villegier, and V. Bouchiat, "Quantum and thermal phase slips in superconducting niobium nitride (NbN) ultrathin crystalline nanowire: application to single photon detection", Nano Lett. **12**, 3501 (2012).

CHAPTER 6

CONCLUSIONS AND SCOPE FOR FURTHER RESEARCH

6.1 Introduction

The feasibility study towards research and development on SNSPD has the focus of the thesis. A summary of the important results of this thesis is presented in this concluding chapter. Following a brief summary of the results, we conclude this chapter by identifying a few potential frontiers of further research on SNSPD and its applications.

6.2 Summary of the thesis

This thesis is a preliminary study of nanostructure samples for their application in single photon detection. The basic understanding of the superconductor based single photon detector and its superior figure of merits in comparison to other existing technology in the field of secure quantum communication was the motivation behind selecting this topic.

Various components required to be used in readout circuit at room temperature as well as cryogenic temperature have been discussed.The electrical model of the device was simulated using microwave simulation software. The transient response and S-parameters were studied. The experimental readout setup can be taken up as future work with incorporation of identified electronics from simulated setup.

A low temperature measurement facility has been set up with temperature stability of 10mK with provisions for electrical as well as optical characterization. The target temperature of 1.8K is achieved even with maximum heat load.

An extensive study on superconducting thin film growth and optimization for next generation superconducting single photon detector has been performed. The

optimization of process parameters has been performed to achieve high Tc of the film by controlling the N_2 as well as Ar gas flow inside the chamber during deposition. The $Si//SiO_2$ was used as substrate as it can act as optical cavity for photon trapping while doing optical characterization in future. A more detailed analysis of film structure in terms of crystal phase, lattice parameter and microstructure might be taken as future work in the direction of optimization of film deposition.

Detailed study for nanowire fabrication in the form of meander structure using EBL and FIB was carried out. The transport properties of these samples were studied at different operating temperatures. It was found that the resistance of the meander structure created using FIB does not reach zero even below the critical temperature and it shows some residual resistance. The cause may be the formation of resistive barriers in series due to Ga ion contamination. The impurity of Ga ion contamination can be avoided by use of capping (protective) layers of Au which can be taken as future work in order to study the feasibility study of fabrication of the nanostructure sample towards its application of single photon detector with the help of FIB.

6.3 Scope for further research

6.3.1 Immediate goals / ongoing research

In this thesis we have been able to explore only a few aspects of the SNSPD using NbN superconductors. Here we enumerate some obvious research directions that are part of the ongoing research.

(1) Realization of HEMT amplifier based detection setup

(2) Optical setup for complete device characterization

(3) Realization of practical SNSPD

6.3.2 Some possible extensions of the current work

Apart from that there are certain research directions as mentioned below which will be included at the later stage.

(1) Research towards enhancement of optical coupling in superconducting nanowires single photon detectors

The activity towards enhancement of optical coupling essentially includes following components:

- Modelling of optical cavity and DBR structures out of variety of semiconductor or dielectric materials
- Experimental realization of optical cavity structure on the top of the detector
- Experimental realization of distributed bragg reflector (DBR) prior to deposition of superconducting thin films.

(2) High-Tc superconductors for realizing SNSPDs

Although, due to large superconducting energy gap of highT_c cuprates compared to that of NbN, sensitivity to photon detection is expected to be lower, an effort to explore the possibility of high Tc cuprates may open a new research direction in the field of SNSPD.

(3) Further research on nanowire fabrication using FIB

Although EBL route is found out to be a better choice when it comes to superconducting nano structuring, considering the simplicity of FIB milling efforts are currently being directed towards understanding the effect of gallium contamination on superconducting properties. In order to prevent degradation of superconducting properties due to gallium implantation research initiatives on capping layer which apart from protecting the underneath superconducting layer, influences the device performance as well will have a lot of potential for applications in single photon technologies.

(4) Establishment of single photon detection based metrology infrastructure

CSIR- National Physical Laboratory (NPL) being a National Metrology Institute (NMI) of India is engaged in frontline research in the areas of standards, material

science, energy, radio and atmospheric sciences and superconductivity. In the light of recent developments and owing to the demand of the present situation, it is absolutely essential to actively participate in the research being conducted throughout the globe and to provide metrology infrastructures for assisting optimizations and standardizations in the field of quantum information and computation.